SSC-58

The Superconducting Super Collider

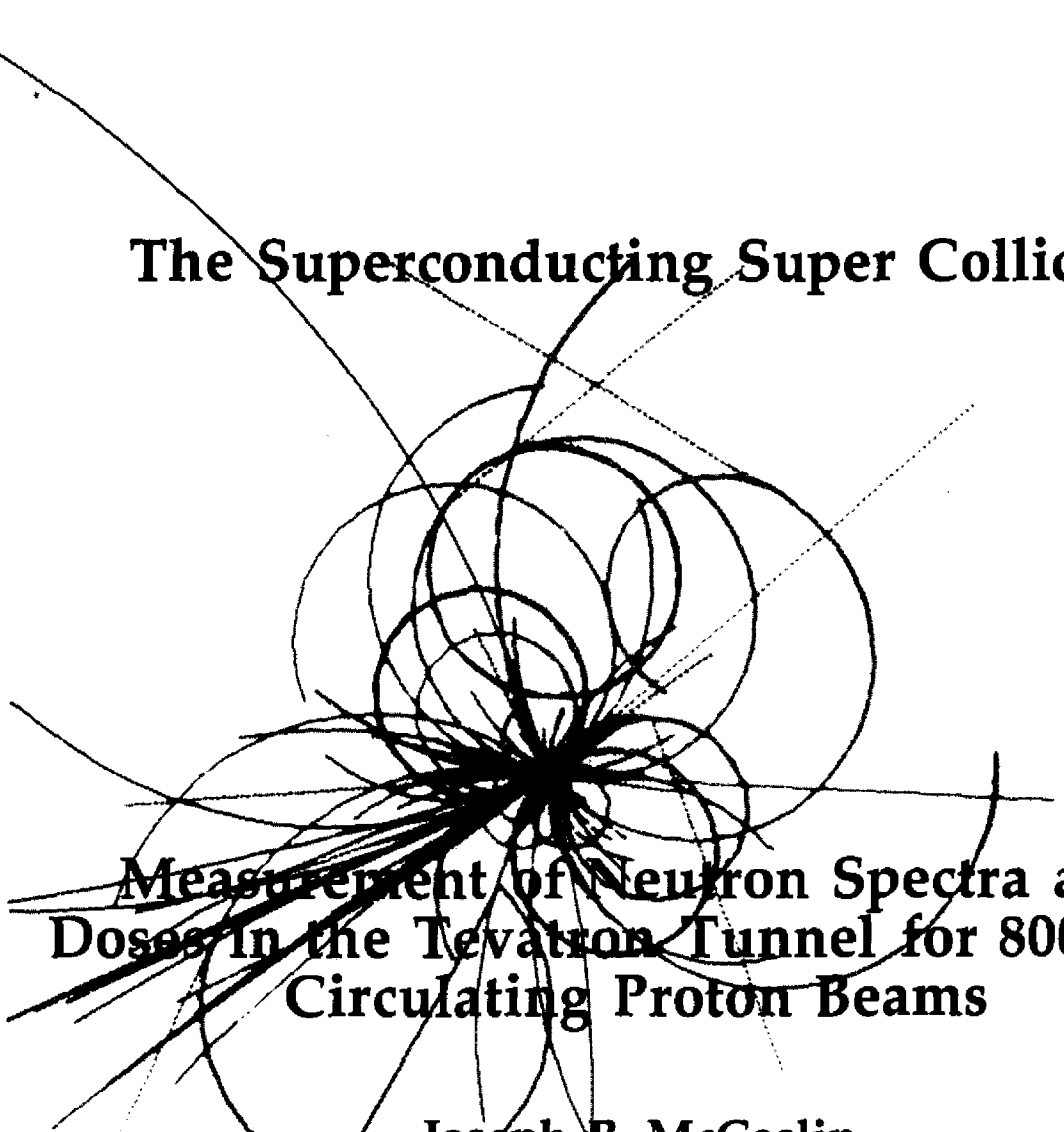

Measurement of Neutron Spectra and Doses in the Tevatron Tunnel for 800 GeV Circulating Proton Beams

Joseph B. McCaslin,
Rai-Ko S. Sun and William P. Swanson
Lawrence Berkeley Laboratory
University of California
Berkeley, CA 94720

Alexander J. Elwyn,
William S. Freeman and Peder M. Yurista
Fermi National Accelerator Laboratory
P.O. Box 500
Batavia, IL 60510

October 3, 1986

SSC-58

MEASUREMENT OF NEUTRON SPECTRA AND DOSES IN THE TEVATRON TUNNEL FOR 800 GeV CIRCULATING PROTON BEAMS

Joseph B. McCaslin, Rai-Ko S. Sun, and William P. Swanson
Lawrence Berkeley Laboratory
University of California
Berkeley, CA 94720

and

Alexander J. Elwyn, William S. Freeman, and Peder M. Yurista
Fermi National Accelerator Laboratory*
P.O. Box 500
Batavia, IL 60510

October 3, 1986

*Operated by Universities Research Association for the Department of Energy

MEASUREMENT OF NEUTRON SPECTRA AND DOSES IN THE TEVATRON TUNNEL FOR 800 GeV CIRCULATING PROTON BEAMS

Joseph B. McCaslin, Rai-Ko S. Sun and William P. Swanson

Lawrence Berkeley Laboratory
University of California
Berkeley, CA 94720

Alexander J. Elwyn, William S. Freeman and Peder M. Yurista

Fermi National Accelerator Laboratory
P. O. Box 500
Batavia, IL 60510

ABSTRACT

Measurements of the neutron fluence and energy spectrum were made in the Fermilab tunnel during Tevatron operation, using Bonner spheres and other instruments operated under various gated conditions. With a coasting beam of 10^{11} protons at 800 GeV, the average fluence rate at 2 m from the beam line was 3.6 cm^{-2} sec^{-1}. Comparison was made between spectra from the unfolding codes BUNKI, LOUHI and SWIFT, and reasonable agreement was found. There were no significant qualitative differences between spectra determined for Tevatron coasting beam conditions at 800 or 150 GeV or for Main Ring acceleration to 120-150 GeV at our location. When the unfolded spectra are plotted in lethargy units, in addition to the usual slowing-down component and thermal peak, a prominent peak is evident at about 0.23 MeV. About 30% of the fluence is contained between 100 keV and 1 MeV, and there is a surprising paucity of high-energy neutrons ($\approx$ 4% above 10 MeV). The median energy for the unfolded spectra is about 0.06 MeV and the average quality factor is close to 7.0. Values for the average neutron kerma factor in tissue and silicon are determined and upper limits are given for absorbed doses due to photons and minimum-ionizing particles.

MEASUREMENT OF NEUTRON SPECTRA AND DOSES IN THE TEVATRON TUNNEL FOR 800 GeV CIRCULATING PROTON BEAMS

Joseph B. McCaslin, Rai-Ko S. Sun and William P. Swanson

Lawrence Berkeley Laboratory
University of California
Berkeley, CA 94720

Alexander J. Elwyn, William S. Freeman and Peder M. Yurista

Fermi National Accelerator Laboratory
P. O. Box 500
Batavia, IL 60510

I. INTRODUCTION

An important consideration in the early design stages of conventional facilities for particle accelerators is the protection of accelerator components, control circuitry and detectors within the accelerator enclosure from radiation damage. In particular, neutron induced defects (displacements, transmutations, etc.) are important mechanisms for semiconductor degradation and eventual failure. The designer needs detailed knowledge of the components of the radiation field, their energy distributions and intensities. The primary object of this study is to determine the neutron fluence and spectrum within the Tevatron tunnel, and, insofar as possible, relate these to beam loss.

Existing literature provides little guidance regarding radiation within a high-energy accelerator enclosure. The massive CERN-LRL-RHEL shielding experiment of the mid-1960's, for example, used 26 GeV protons on a fixed target at the CERN PS (Gil68). However, extrapolation to SSC energies is difficult from what is now considered a 'low energy' experiment and is likely to lead to overly pessimistic estimates of both radiation intensity and spectral hardness because of the greater importance of the forward peaking of radiation at SSC energies. Apart from the CERN shielding experiment, no detailed measurement of radiation fields within the enclosure of a high-energy accelerator has been undertaken until now. Related useful studies have recently been performed in a labyrinth connecting onto a 400 GeV extracted beam line at the Tevatron (Cos85).

The results of this measurement program have additional application in the following areas:

- shielding design, especially for thin shields, as well as alcoves, labyrinths and other penetrations;
- understanding and reducing backgrounds in experimenters' detectors;
- understanding of the hadronic/electromagnetic cascades which generate the observed radiation fields.

II. EXPERIMENTAL SETUP

It was proposed that the measurements be made in a section of the tunnel that contained no devices that could contribute to high losses (e.g., septa, scrapers etc.). The A-4 Sector was selected as representative of a 'typical' section of tunnel for our measurement program during periods of Tevatron 800 GeV coasting beam operation. Measurements were also taken during periods of Main Ring (MR) operation. More information on the design and operation of the entire Tevatron system can be found in the review article by Edwards (Edw85).

Figure 1 shows a plan view of the counter array which spanned a length of 4.9 m. The upstream end (for proton operation) was 14 m from the downstream end of a warm 4-m accelerator straight section (A-48) near B-0. For low-beta coasting beam conditions, the working hypothesis was that this 4-m warm section constituted the local source of primary interactions for detected events. Figure 2, a cross sectional view of the tunnel, shows that the detectors were at the same elevation as the Tevatron ring at the opposite side of the enclosure and therefore to the interior of the ring. The distance from the beam line to the center of each detector was 2.0 m.

For the neutron energy spectral studies, a Bonner sphere spectrometer (Bra60, Aws85) was used as the primary measurement system. This inherently low-resolution system consisted of eight cylindrical LiI(Eu) scintillation crystals (12.7 mm diam $\times$ 12.7 mm high), enriched to 99% ^{6}Li, surrounded by spherical polyethylene neutron moderators ranging in diameter from 0 to 45.72 cm (0, 2, 3, 5, 8, 10, 12 and 18 in.). These detectors are coupled through photomultiplier tubes and an 8-input mixer-router to a 4096-channel multi-channel analyzer (MCA) (Fig. 3).

Thermal neutrons were detected through the ^{6}Li(n, α)^{3}H (Q=4.782 MeV) reaction,which produces a well-defined peak in the pulse height distribution from each crystal. Simultaneously, an additional ^{6}LiI(Eu) detector surrounded by a 12.7-cm (5-inch) diameter moderator sphere was used as a beam loss monitor by multi-channel scaling the counts in the neutron capture peak on a second 4096-channel MCA. This provided a check on the relative neutron fluence rate as a function of time during a data acquisition period to ensure that there were no periods of large, isolated beam losses. In addition, two moderated BF_3 gas proportional counters, a parallel plate thorium fission counter and a similar bismuth fision counter were used to obtain additional fluence and spectral information.

The Tevatron and Main Ring (MR) share a common tunnel. Because of certain high-loss activities associated with the operation of the MR (8-GeV injection, passage through MR transition), it was necessary to gate the detectors off during selected periods of operation. The gate-on condition was selected through FNAL-designed circuitry* that derived its signals from specified Tevatron clock events (Bee85). Four basic gating modes were available, along with their logical complements. They are shown in Table 1, in which 'TFT' signifies 'Tevatron flat-top', or the condition of circulating beam at constant energy, and $\overline{MR}$ (read: 'Not Main Ring') means that the Main Ring was not operating. For some data-taking runs the gating mode (or its complement) was logically combined with the signal from an additional manually set gate and delay generator. This allowed complete flexibility in the start of a counting interval and its duration, subject to the constraint of the selected gating mode. As an example, the electronics could be gated off ($\overline{MR}$) during the extremely high loss time of 8 GeV Main-Ring injection, while allowing measurements during the remainder of a main cycle.

* We are grateful to V. Dixon Bogert and David G. Beechy of Fermilab for design and fabrication of the special gating logic.

Table 1. Gating conditions used.

Mode 1	IF ($\overline{MR}$ and TFT)	Q = TRUE
Mode 2	IF ($\overline{MR}$)	Q = TRUE
Mode 3	IF (TFT)	Q = TRUE
Mode 4	IF (anything)	Q = TRUE

The data were gathered in a parasitic mode as background to machine development work -- during periods of tuneup and studies related to colliding beam operation (the first Tevatron $\overline{p}$-p collisions were achieved during the final week of the run). Data obtained under the Mode 1 gating condition ($\overline{MR}$ and TFT) were of primary interest. However data related to Main-Ring operations under various conditions were also obtained. Intensities in the Tevatron were typically 10^{11} protons circulating the ring at 47.75 kHz at flat-top energies of 150 and 800 GeV. Although the low beam currents used for accelerator studies enabled us to accumulate data at a convenient rate, without counting-loss or pileup problems, accurate determination of beam intensity was difficult. A number of possible beam monitors were considered and finally the DC toroid current monitor T:IBEM1 was chosen for normalization when available. While T:IBEM1 typically indicated 10^{11} protons stored, T:SMBEAM, another current toroid which was continually available but was only sensitive to the number of protons in the central and satellite buckets, gave readings of only about 40% of the T:IBEM1 readings. We believe that the T:IBEM1 readings are the more relevant to our measurements because they reflect the entire circulating current. Absolute beam intensities are probably known only to within a factor of two.

Pressure in the warm A-48 straight section was estimated as about 2×10^{-8} torr and the pressure in the cryogenic dipole string, said to be about 1×10^{-13} torr or less, was negligible by comparison (Jos86). The A-48 section was therefore the presumed source of beam interactions which initiated the neutron-producing cascades in our vicinity. Under the best stored-beam conditions achieved during our running time, the Tevatron beam life time ($1/e$) reached about 2.5-6h and 70-100h for 150 and 800 GeV operation, respectively (Edw86).

Data-taking run durations ranged from tens of minutes to more than an 8-hour shift, with 1 hr being typical. Since we had no control over accelerator conditions, our mode of operation was to begin a run when conditions seemed suitable and later determine actual beam intensities and lifetimes. Following each run, the pulse height distributions and background-subtracted peak integrals for the LiI counters were recorded, as well as counts in the BF_3, Th-fission and Bi-fission counters and the accumulated gate 'on' time.

The two identical BF_3 counters placed just upstream and downstream of the detector array (Fig. 2) give an indication of the direction to the neutron source 'centroid'. The ratio of counter rates, [BF_3-U/BF_3-D] = [Upstream / Downstream], varied from 0.68 to 1.56 for Tevatron runs at 800 GeV. Ratios greater than unity suggest a predominently upstream source. i.e., the 20-m dipole chain, whereas less than unity suggests a source in the downstream direction, towards the quadrupole chain leading to B0. A summary of these ratios is shown in Table 2, grouped by type of gating mode. The average is close to unity for all types of Tevatron runs but the standard deviations indicated for each gating mode indicate significant spread within each group. As the statistical uncertainty is insignificant, this means that the source 'centroid' does vary in our region, both upstream and downstream but the average location is not far from our counter array.

The analogous ratio for Main Ring runs suggests a neutron source 'centroid' more downstream of our counters but the information is not conclusive.

Table 2. Ratio of BF_3-detector counts by type of gating.

Type of Run	Energy	No. of Runs Averaged	Ratio BF_3-U/BF_3-D
$\overline{MR}$ · TFT CB[a]	800 GeV	4	1.24 ± 0.21
$\overline{MR}$ · TFT ALL	800 GeV	13	0.99 ± 0.23
$\overline{MR}$	800 GeV	2	0.88 ± —
$\overline{MR}$ · TFT	150 GeV	1	0.91 ± —
Average of 20 runs			1.01 ± 0.22
MR	8 - 150 GeV	5	0.73 ± 0.26

(a) CB: Coasting beam runs selected for small beam loss (runs listed in Table 3).

III. ANALYSIS OF NEUTRON SPECTRA

A. The General Problem

A typical pulse height distribution in ^{6}LiI(Eu) is shown in Fig. 4 for the 7.62 cm (3-in) diameter sphere. The peak near Channel 57 corresponds to events associated with the capture of thermal neutrons via the ^{6}Li(n, α)^{3}H reaction in the scintillator (Q=4.782 MeV). For all detectors except the 30.48 cm and 45.72 cm diameter spheres the background-to-total count under the peak was generally less than 15%; it was $\sim$ 30% for the largest sphere. Even so, neutron counting rates were easily obtained by subtraction of the background rates. For most cases of interest, the counting rates were small enough that counting-loss corrections (at most a few per cent) were not necessary. The relative counting rates in each detector were normalized to the same incident neutron fluence by linearly interpolating between observed background-corrected counting rates in the two identical BF_3 counters which were placed a known distance apart (4.9 m), on either end of the line of Bonner spheres. The ratio of the counting rates in the two BF_3 counters varied from (BF_3-U / BF_3-D) = [Upstream / Downstream] = 1.12 to 1.55 for the 800 GeV coasting beam runs. The average was 1.24. It is assumed that although the neutron fluence may have varied with distance along the line of Bonner spheres, the neutron spectrum did not change.

Measured neutron counting rates in the Bonner spheres are related to the neutron spectrum through the Fredholm equation

$$C_r = \int_0^\infty N(E) R_r(E) dE , \tag{1}$$

where C_r is the counting rate in a detector surrounded by a spherical moderator of radius r, N(E) is the neutron spectrum and $R_r(E)$ is the energy-dependent response function for a sphere of radius r. Given C_r and R_r, N(E) can be obtained by standard unfolding techniques.

In practice, Equation (1) is converted to a discrete form:

$$C_r = \sum_{i=i}^{n} N(E_i) R_r(E_i) \Delta E_i \,, \tag{2}$$

where $N(E_i)$ is the differential neutron fluence for the ith energy bin ΔE_i, and the response functions are obtained from a separate calculation. In the present work the functions of Sanna appropriate to 12.7 mm × 12.7 mm LiI(Eu) crystals and the specific polyethylene sphere density are used (San73). These functions are defined for either 31 or 40 discrete energy groups, depending on the unfolding program that is used. The unfolding problem is thus reduced to solving 8 equations (i.e., data from the 8 spheres) for either 31 or 40 unknowns. Equation (2) does not have a unique solution, and as is well known, there are inherent difficulties due to the underdetermined and sometimes ill-conditioned nature of such a problem.

B. Comparison of Unfolding Techniques

Because of the inherent problems in unfolding we have chosen to use three different computer programs to derive the neutron spectrum from the measured counting rates: BUNKI uses the SPUNIT iterative recursion procedure along with an algorithm that allows a choice of different starting solutions (Lo84, Br84); LOUHI is a constrained least-squares method that allows user-controlled constraint conditions (Rou80); and SWIFT is based on a Monte-Carlo method that allows a broad sampling of possible neutron spectra with no *a priori* assumptions about their character, apart from non-negativity (OBr81, Cha83, OBr83).

From the derived neutron spectrum that acceptably reproduces the measured counting rates for a given data set one can determine the neutron fluence, absorbed dose (kerma)* and dose equivalent, and thus the quality factor** associated with the neutron field. These quantities and other characteristics of the spectra unfolded using the three programs are discussed below for representative data sets.

In general, the fit to measured neutron counting rates is of comparable quality for the three unfolding codes. Figure 5 compares the fit from the LOUHI program, for example, with the measured sphere responses for the case of a Mode 1 (see Section II) 800 GeV low-beta coasting beam run. The other smooth curves on this figure represent calculated sphere responses if 100% of the neutron fluence is assumed to be in the energy bins indicated.

The neutron spectra derived from the three unfolding codes for this case are compared in Fig. 6. The results are quite similiar, except that SWIFT tends to predict higher, narrower peaks at the same location, than do the other programs. Although the shapes may vary, the areas under the respective curves do not differ significantly. Note that the energy scale is logarithmic and the ordinate is $\Delta\phi(E)/\Delta(\log E)$. In these units the area under the curve for each energy bin as it

* *Kerma* is defined as the 'quotient of dE_{tr} by dm where dE_{tr} is the sum of the initial kinetic energies of all the charged ionizing particles liberated by uncharged ionizing particles in a material of mass dm' (ICRU80). The unit for kerma is the Gray [1 Gy = 1 J kg^{-1}] or the rad [1 Gy = 100 rad].

** The quality factor, Q, is a factor by which the absorbed dose is multiplied to better approximate the effect of radiation on humans. In the absence of other modifying factors, the product of Q and the absorbed dose, D (in rad or Grays), is equal to the dose-equivalent, H (rem or Sieverts). The latter quantity is used to quantify the radiological exposure to persons. Values of Q for neutrons range between 2 and 11 with Q = 10 being considered a nominal 'conservative' value. Values of Q are based on recommendations of the International Commission on Radiological Protection (ICRP73).

appears on the graph is proportional to the neutron fluence within that bin.

C. Tevatron Spectra for 800 and 150 GeV

The dominant feature of spectra determined for 800 GeV operation (Fig. 7) is the prominent peak centered at an average of 0.23 MeV (with average energy values at half-height of 0.05 and 1.3 MeV). This peak is superimposed on a spectrum that is quite "soft"; only about 4% of the total fluence is from neutrons with energies greater than 10 MeV, about 30% of the fluence is between 100 keV and 1 MeV, and about 21% is below 1 eV (averages from several runs). These features can be seen in Fig. 8 in which the spectrum of Fig. 7 is expressed as cumulative percentages of fluence and absorbed dose (tissue) plotted as a function of neutron energy. The apparent paucity of very high energy neutrons is confirmed by the negligibly small counting rates from the thorium and bismuth fission counters (with neutron detection thresholds at $\approx$2 and $\approx$50 MeV, respectively; see below).

The spectral features discussed above are typical for data obtained under similiar gating constraints (Modes 1 and 2 in Section II, for example). This was true even under running conditions where large fluctuations in beam intensity and large beam losses were observed. Furthermore, the spectral features remained unchanged when the Tevatron was run at low-beta coasting beam at 150 rather than 800 GeV. This can be seen in Figs. 9 and 10 where again about 35% of the total fluence is from neutrons with energies between 100 keV and 1 MeV and only about 2% arises from energies greater than about 10 MeV (averages from several runs).

Neutron fluence, absorbed dose, and quality factors obtained from the spectrum unfolding calculations are shown in Table 3 along with other characteristics of the various data sets. These runs represent Tevatron 800 GeV low-beta coasting beam operation during which the beam intensity fluctuated very little and beam losses appeared small and relatively constant. Other data for Tevatron test runs when beam intensities and losses varied widely are not listed here because of large uncertainties in beam conditions. The single 150-GeV run, shown in Table 3 and in Figs. 9 and 10, unfortunately falls in the category of uncertain conditions. For the runs shown in Table 3 for 800 GeV, it is reasonable to assign uncertainties of at least 50% to the beam intensities listed in Column 4. Averaging the four runs we find a neutron fluence rate of 3.6 neutrons cm^{-2} sec^{-1} and an absorbed dose rate (in tissue) of 0.026 mrad/hr for a coasting beam of 10^{11} protons at 800 GeV. It should be emphasized that these numbers are for Tevatron operation only; as mentioned, data taking was normally gated off during injection into and ramping of the Main Ring.

The neutron fluence was also determined from measured BF_3 counting rates. By use of a previously determined calibration factor* of 0.66 neutrons cm^{-2} $count^{-1}$, fluence rates of 2.2×10^{-11} cm^{-2} sec^{-1} $prot^{-1}$ and 2.6×10^{-11} cm^{-2} sec^{-1} $prot^{-1}$ were found for the downstream and upstream BF_3 detectors, respectively, for the 800-GeV runs shown in Table 3. Since the moderated BF_3 counting has an approximate 0.02 MeV threshold for neutron detection, the average fluence rate in Table 3 has to be multiplied by the fraction of total fluence associated with neutrons of energy greater than this threshold to compare with the BF_3 values. For the 800 GeV runs in Table 3 this fraction averages 55%, so that the unfolded value of fluence rate for neutrons greater than 0.02 MeV is $0.55 \times 3.6 \times 10^{-11}$ neutron cm^{-2} sec^{-1} $= 2.0 \times 10^{-11}$ neutron cm^{-2} sec^{-1} $proton^{-1}$, in good agreement with the BF_3 values above. Thus the fluence obtained with the BF_3 counts is consistent with that of the Bonner-sphere spectrometry.

* Moderated BF_3 counter calibration is based on an NBS ^{238}PuBe neutron source whose emissivity is known to $\pm$ 2%.

Table 3. Characteristics of neutron spectra in low-beta Tevatron coasting beam runs.

Log Page	Date (Time)	Gate on Time (sec)	Beam Intensity (T:IBEM1) (protons)	Ratio BF-3 Counts Upstream/Downstream	Neutron Fluence (10^3 neuts cm^{-2}) BUNKI	LOUHI	SWIFT	Average Fluence Rate (cm^{-2}s^{-1})	Tissue Absorbed Dose (μrad) BUNKI	LOUHI	SWIFT	Average Tissue Dose Rate (μrad·h^{-1})	Quality Factor BUNKI	LOUHI	SWIFT	Ave. QF	Average Fluence Rate per Proton (10^{-11}·cm^{-2} s^{-1}·proton^{-1})	Average Tissue Dose Rate per Proton (10^{-13} mrad h^{-1}·proton^{-1})
	For 800 GeV:																	
48	9/23 (0725-0825)	1160	8×10^{10}	1.55	2.98	2.97	2.87	2.53	6.2	11.8	6.0	25	6.41	6.16	7.55	6.71	3.16	3.13
60	9/24 (0635-0730)	1055	2×10^{11}	1.17	6.84	6.80	6.85	6.47	10.7	9.9	13.7	39	7.08	7.45	7.58	7.37	3.24	1.95
62	9/25 (1016-1120)	1218	1.4×10^{11}	1.13	5.35	5.35	5.28	4.37	10.0	12.5	11.0	33	6.34	6.26	7.01	6.54	3.12	2.36
90	9/30 (0921-1000)	1027	2.5×10^{11}	1.12	12.3	12.2	12.1	11.9	18.0	17.0	25.0	70	6.64	7.00	7.04	6.89	4.76	2.80
	Average values			1.24												6.88	3.57	2.56
	For 150 GeV:*																	
64	9/26 (0525-0538)	265	1.0×10^{11}	0.91	1.27	1.25	1.27	4.77	2.4	1.5	2.5	29	6.94	7.83	7.94	7.57	4.77	2.90

*Noticeable beam loss for this run.

Table 4. Characteristics of spectra during Main Ring acceleration.

Log Page	Date (Time)	Delay of Start (sec)	Gate on Time (sec)	Integrated Main Ring Beam (Approx.) (10^{13} protons)	Ratio BF-3 Counts Upstream/Downstream	Neutron Fluence (10^5 neuts·cm^{-2}) BUNKI	LOUHI	SWIFT	Ave. Fluence (10^5 neuts·cm^{-2})	Tissue Absorbed Dose (mrad) BUNKI	LOUHI	SWIFT	Ave. Tissue Dose (mrad)	Quality Factor BUNKI	LOUHI	SWIFT	Ave. QF	Average Fluence per Proton (10^{-9} cm^{-2} · proton^{-1})	Average Tissue Dose per Proton (10^{-15} mrad · proton^{-1})
50	9/23 (1557-1615)	1.5	408	4.32	0.91	0.76	0.76	0.72	0.75	0.098	0.089	0.125	0.104	7.40	7.86	8.20	7.82	1.74	2.41
52	9/23 (1646-2049)	1.5	5588	62.8	0.83	6.63	6.59	6.35	6.52	0.87	0.83	1.04	0.913	6.45	6.56	7.38	6.80	1.04	1.45
54	9/23 (2153-2220)	1.0	794	8.78	0.99	1.60	1.58	1.55	1.58	0.23	0.20	0.29	0.24	7.10	7.56	7.78	7.48	1.80	2.73
—	10/4 (1003-1025)	0.85	442	6.05	0.58	0.281	—	0.265	0.273	0.038	—	0.041	0.040	6.76	—	7.69	7.23	0.45	0.66
—	10/4 (1144-1155)	0.85	101	0.21	0.35	0.050	—	0.048	0.049	0.0061	—	0.0071	0.0066	6.28	—	6.96	6.62	2.33	3.14
	Average values	—	—	—	0.73	—	—	—	—	—	—	—	—	—	—	—	7.19	1.47	2.08

D. Main Ring Spectra

Data were also obtained during periods of Main-Ring acceleration by gating on the electronics with the logical complement $\overline{Q}$ of Mode 1 and 2 signals. For these runs the actual start of the counting interval was delayed by 0.85 to 1.5 seconds from the initial $\overline{Q}$ signal to avoid the extremely high beam losses (and possible large detector dead times) associated with 8 GeV injection into the Main Ring. Again, of the three unfolding codes used, SWIFT predicts a larger thermal component than the other unfolding codes, but otherwise the three spectra have similiar properties. Figures 11 and 12 show an example of a typical spectrum unfolded with LOUHI. The similarity to the Tevatron 800 and 150 GeV runs is striking. The prominant peak (between 0.03 and 2.1 MeV, average energy at half-height) is centered at about 0.26 MeV. As with the Tevatron spectra discussed above, a characteristic is the 'softness' of the spectrum; less than about 2% of the fluence is from neutrons with energy greater than 10 MeV, about 28% from 0.1-1.0 MeV and about 22% from those less than 1 eV (averages for runs of Table 4). To within the internal (run-to-run) variations seen in the unfolded results, the Main Ring and Tevatron spectra can be considered to be the same.

Characteristics of Main-Ring runs are shown in Table 4. These runs represent many different machine operating conditions. Not only is Main Ring ramping associated with acceleration up to 150 GeV for Tevatron injection and 120 GeV for $\bar{p}$ production, both within a given accelerator super-cycle, but a large number of tests and procedures (cogging, coalescing, low-beta focussing, etc.) were performed during the period of these studies. Consequently, records of the actual intensity of the beam in the Main Ring were not always complete or even available. The runs shown in the table represent those in which an estimate of the total number of protons could be obtained for the periods during which the electronics was gated 'on'. The integrated intensity, based on an assumed 4-second cycle (0.25 Hz), is shown in Column 5; the precision is not better than a factor of two. It should be noted that the duration of the runs listed in Column 4 are the times during which the electronics was gated 'on'; it does not necessarily represent the time during which beam was actually accelerated in the Main Ring since some accelerator cycles have no beam associated with them.

Column 3 of Table 4 gives the time delay between the initial $\overline{Q}$ signal and the actual start of the counting interval. The value of 0.85 seconds is actually about 0.2 seconds longer than is necessary to completely eliminate the detection of neutrons from beam losses associated with injection from the Booster into the Main Ring. Neither the neutron fluence nor the absorbed dose seem to depend on this value; the last two columns show that, except in one case, both the fluence and the absorbed dose are constant to about a factor of two from run to run, when normalized to the estimated beam intensity. The average values are 1.47×10^{2} neutrons cm^{-2} and 2.1×10^{-4} mrad (tissue) for a total beam of 10^{11} protons.

E. Median and Effective Neutron Energy

The median energy of the fluence distribution and of the absorbed dose (tissue) distribution are both given in Table 5. These energies correspond to the average of 50% values of distributions like those shown in Figs. 8, 10 and 12. Values of the fluence-median vary between 0.059 and 0.11 MeV for four types of gating. Values for the absorbed-dose median are higher and also have a smaller spread: 0.49 - 0.69 MeV. Errors are estimated from the internal consistency of the data and are about $\pm$ 35% for each value listed. Therefore differences may not be significant.

In addition, the average kerma factor (absorbed dose to tissue divided by fluence) can be used to determine an effective neutron energy. Values so derived using tabulations of Caswell et al. (Cas80) are also shown in Table 5 for the set of runs listed in Tables 3 and 4. The remarkable thing about the energies shown in Table 5 is their small values. Plausible reasons for this are

Table 5. Median and effective neutron energy.

Type of Run	Energy	Number of Runs Averaged	Median Energy (MeV) Fluence	Median Energy (MeV) Abs.dose	Eff.Energy (tissue) (MeV)
$\overline{MR}$ · TFT CB[a]	800 GeV	4	0.059	0.61	0.82
$\overline{MR}$ · TFT ALL	800 GeV	12	0.057	0.69	0.38
$\overline{MR}$ · TFT	150 GeV	1	0.110	0.49	0.58
Average of above			0.061	0.66	0.59
MR	8-150 GeV	5	0.051	0.62	0.38

(a) CB: Coasting beam runs selected for small beam loss (runs listed in Table 3).

given in Section VI.

F. Paucity of High Energy Neutrons

The spectral unfolding described above indicates that relatively few neutrons are present above a few MeV. This result is directly confirmed by data from the BF_3, thorium-fission and bismuth-fission counters. In the analysis of Table 6, sensitivity of the counters was assumed constant with neutron energy above the thresholds indicated. Twenty separate runs using either gating Mode 1 or 2 were combined, giving a total clock time of 3696 min. The total gate-on time was 1088 min (65278 sec).

Table 6. Combined Tevatron runs with Mode 1 or 2 gating (20 runs; 65278 sec).

Type of Counter	Energy Range (MeV)	Total Counts	Calibration Factor (cm^{-2} $count^{-1}$)	Fluence Rate ($cm^{-2}sec^{-1}$)	Relative Fluence
Th-fission	>2	50	3500	2.7	0.095
Bi-fission	>50	6	3000	0.28	0.0097
BF_3-U	0.020 - 20	2,659,778	0.66	26.9	1.00
BF_3-D	0.020 - 20	2,940,705	0.66	29.7	

The two BF_3 counters, spaced 4.9 m apart, gave a ratio of [Upstream/Downstream] = 1.10 for this set of runs. In the right hand column, the two fission-counter fluences are divided by the *average* for the two BF_3 counters. These relative figures indicate that the fluence of neutrons with E > 2 MeV and E > 50 MeV from Tevatron operation average about (9.5 ± 1.4)% and (0.97 ± 0.4)%, respectively, of the total fluence as measured by BF_3 counters.

IV. DOSES TO LITHIUM IODIDE

A. Sources of Dose

The individual LiI crystals are cylinders of diameter and height 12.7 mm (1/2 in), density 4.06 g cm^{-3}, and mass 6.53 g. If the energy calibration of the detector-MCA system is known, the total dose to each crystal can be obtained by the straight-forward summation of the energy-weighted channels of the pulse height distributions and division by the mass, once assumptions have been made about the counts in channels between zero and the electronic threshold for each distribution. The total dose in each crystal is made up of the following contributions:.

(1) Thermal neutron reactions (n, α), i.e., the thermal peak;

(2) Fast-neutron reactions with ^{6}Li, such as (n, α), (n,n'd);

(3) incident charged particles from the hadronic cascade;

(4) incident photons from the electromagnetic cascade fed by the hadronic cascade;

(5) photons from neutron capture in the detector or moderator (CH_2 or LiI); and

(6) incident photons from neutron capture elsewhere; e.g., iron or concrete in the tunnel environment.

Of these the thermal neutron peak is easily separable and forms the basis for the analysis and discussion of Section III. Fast neutrons with energies between 0.1 and 1.0 MeV (30 - 35% of the total neutron fluence for Tevatron spectra) also fall within the pulse-height range encompassed by the thermal peak. Neutrons with energies greater than a few MeV could interact in the detector through both the ^{6}Li(n, α) and ^{6}Li(n, n'd) reactions. However, according to the analysis of Section III, relatively few neutrons fall into this range (2 - 4% above 10 MeV for Tevatron spectra); we neglect their contribution to the LiI dose.

B. Minimum Ionizing Particles

Charged particles from the high energy hadronic cascade (pions, muons) are expected to be largely minimum ionizing and their energy loss rate is about 1.2 MeV g^{-1} cm^2 (for relativistic pions and muons) (PDG84). The maximal expected energy loss, for a minimum ionizing particle traversing a diameter of a LiI crystal, is then 6.2 MeV. As the detectors were centered in the plane of the Tevatron ring, high-energy charged particles should be incident in approximately the same plane. For a broad monoenergetic beam perpendicular to the crystal axis, the expected energy loss distribution rises from zero probability for zero energy loss (tangential incidence) to a sharp peak at maximum energy loss for a diametral path (Fig. 13; also see Appendix G). An analysis of the *distribution* of energy losses by a broad field of minimum ionizing particles perpendicular to the crystal axis gives a mean and standard deviation of (4.87 $\pm$ 1.36) MeV. Thus any important component of such particles should manifest itself as an enhancement Channels 71 - 127.* As no such enhancement is seen in the pulse height distributions, and because photon and neutron contributions to the pulse height spectra are expected to be important in this same region the dose due to minimum ionizing particles cannot be determined except as an upper limit.

The 45.7-cm (18-inch) sphere contains the smallest number of counts in the minimum ionizing region and its thickness of polyethylene should not affect the fluence of high energy charged particles. Therefore it is taken as the detector for the purpose of establishing this upper limit. Ascribing *all* of the pulses in Channels 71 - 127 to minimum-ionizing particles results in:

* This is based on a calibration of the same crystals using gamma sources ^{137}Cs, ^{60}Co and ^{24}Na (Sun86).

$$D_{mip} \leq \frac{1}{6.53\text{g}} \times \frac{3\text{ MeV}}{61} \sum_{C=71}^{127} C \cdot N(C) \tag{3}$$

$$= 7.53\times10^{-3} \sum_{C=71}^{127} C \cdot N(C)\ \text{MeV}\cdot\text{g}^{-1} = 1.21\times10^{-10} \sum_{C=71}^{127} C \cdot N(C)\ \text{rad},$$

where M = 6.53 g is the mass of the crystal, the factor (3 MeV/61) expresses the channel number-energy calibration (Sun86), N(C) is the number of counts in Channel C and the summation is over the MCA channels indicated. As this approach is only approximate anyway, a simplified form for evaluating the summation over 57 channels is based on the observed smoothness of the MCA distributions:

$$D_{mip} \leq 1.21\times10^{-10}\ [57 \times 99\ N(99)]\ \text{rad} = 6.8\times10^{-7}\ N(99)\ \text{rad} \tag{4}$$

The resulting doses may be compared to the neutron and photon doses estimated for the same runs. For 18 (unselected) Tevatron runs made under varying conditions, the ratio of minimum-ionizing particle (mip) dose (to LiI) to neutron dose (to tissue) is found to be:

$$D_{mip}/D_n < 0.077 \pm 0.030 \tag{5}$$

An average for the four selected Tevatron runs at 800 GeV listed in Table 3 gives a consistent result: 0.08 ± 0.03. When this estimate of D_{mip} is divided by neutron fluence instead, we have the relation:

$$D_{mip}/\phi_n < (1.6 \pm 0.6)\times10^{-10}\ \text{rad cm}^2 \tag{6}$$

Because of the limitations outlined above, these must be considered as upper limits and they may overestimate the actual charged particle dose by a large factor.

C. Photon Doses

To estimate an upper limit for the dose to the LiI crystals due to external photons from the EM cascade, we assume a pulse height distribution proportional to E^{-2} which is suggested by the track length distribution from shower theory (Ros56; see Appendix F). The shape is indicated by the curve of Fig. 13, which is normalized to the distribution at Channel 70 ($E_\gamma \approx 3.44$ MeV). In doing this we also implicitly assume the energy transfer efficiency is uniform between chosen limits that are given below. The assumptions just described lead to an integral of the form

$$D_\gamma[MeV\cdot g^{-1}] \leq \left[\frac{N(70)}{M}\right] \times \left[\frac{4900}{(61/3)}\right] \int_{E_1}^{E_2} E^{-1} dE \tag{7}$$

where N(70) is the observed number of counts at Channel 70, M = 6.53 g is the mass of the LiI crystal, the factor $(70)^2 = 4900$ is for normalization and (61/3) converts the abscissa scale from channel number to MeV (Channel 61 corresponds to 3 MeV photon energy; Sun86).

At 0.3 MeV, the photon mass attenuation coefficient in iron is larger by a factor of 3 than at its minimum at about 8 MeV. Photons below this energy would be heavily attenuated. At much higher energies, the energy transfer efficiency declines because the maximum range of electrons from photon interactions reaches a limit of 6.2 MeV (see preceding section), a decreasing fraction as the photon energy increases beyond this. Integration limits of 0.3 and 30 MeV were chosen for this analysis to encompass this range which includes the Compton minimum for iron. Doses based on Equation (7) for the LiI counter in the 5.08-cm (2-in) diameter sphere were calculated. Comparison of the resulting doses is made by dividing the photon doses to LiF, determined as just explained, by neutron doses to tissue as determined from the fitted neutron spectra. An average over 17 runs made under varying conditions gives 1.12 ± 0.50. For the four selected runs listed in Table 2, the average is 1.24 ± 0.50. When this estimate of D_γ is divided by neutron fluence, we have the relation:

$$D_\gamma/\phi_n \; < (1.8\pm0.6)\times10^{-9} \text{ rad cm}^2 \tag{8}$$

Lacking a satisfactory method of subtracting other contributions to the LiI pulse height distributions, this result must be considered as an upper limit.

VI. DISCUSSION

A. Origin of the Tunnel Radiation Field

We imagine that the following general scenario is plausible: Fragments from beam-gas interactions, or protons lost from orbit strike the vacuum vessel at glancing angles and initiate hadronic cascades. As for the cause of proton loss from orbit, an obvious primary mechanism of interest to this experiment is loss due to scattering on residual gas, particularly in the warm section A-48 (Fig. 1). A second cause is beam phase-space excursions in relation to the machine acceptance. While this generic cause could not be monitored during the experiment and is subject to considerable variation, it is noted that B-0 is a low-beta section where loss of orbiting beam should be less than average for the entire machine. Therefore, as regards our experiment, we believe that this mechanism is of lesser importance.

After the hadronic cascade is initiated, the energy carried by the primary proton is eventually partitioned into two fractions: About 37% is retained by the hadrons and is deposited by nuclear interactions and ionization; the remaining 63% is lost to the electromagnetic (EM) cascade (Ran85). This portion is fed by the π^0 decay photons.

In calculations shown below the rule of thumb is invoked which predicts 10 neutrons produced per GeV of hadron-transported (not EM-transported) energy deposited in iron. This is an extrapolation from 10 GeV of data shown by Patterson and Thomas (Pat73, p.141).

The neutrons that finally escape from the iron yoke are of three basic origins -- prompt reaction products of the hadronic cascade, evaporation neutrons from excited residual nuclei and photoneutrons produced by the EM cascade. Of these the evaporation neutrons undoubtedly dominate. The photoneutrons are shown to be negligible (Appendix B). Charged particles from the hadronic cascade are largely absorbed in the iron yoke as are photons from the EM cascade (preceding section; also see Appendix E, F and G).

The beam-tube-magnet system represents a linear source of neutrons that is generally not uniform. However, where a uniform isotropic linear distribution can be assumed, the inverse

square law gives a direct fluence at distance, d, of

$$\phi_{dir} = \frac{q'}{4\,d}\,, \tag{9}$$

where q' is the source strength in neutrons per unit length. From the inverse square law, one also infers that about half of the direct fluence at a distance, d, comes from a beam line segment within $\pm d$ ($= \pm 2$ m) of a detector location. Scattered neutrons constitute the majority of the detected neutrons, and similar arguments would indicate that scattering-surface elements at more than one tunnel diameter (3 m) distance are of diminishing importance. It is also shown below that the dipole magnetic field causes energy to be deposited in the magnet yoke in the downstream direction of a primary beam-gas interaction with a distribution that is approximately of the form $\exp(-z/5.9\text{m})$, reflecting a rather short "decay length". These relations are brought together here to suggest that fluences detected at any position generally are a result of quite localized neutron sources.

Whatever the initial cause of beam loss from stable orbit, the resulting neutrons undergo a number of scatterings within the iron yoke before they filter out. In so doing, they largely lose memory of the initial beam direction, especially the evaporation neutrons which have an energy of a few MeV and are inherently isotropic. After passing the iron yoke filter, the neutrons, partially moderated but relatively unattenuated, undergo further scattering and moderation in the concrete tunnel. It is shown in Appendix C that about 85% of the neutrons detected are scattered neutrons. Of the neutrons *detected,* the fractions are approximately: [neutrons direct from beam line] : [fast neutrons scattered by concrete] : [thermal neutrons from the concrete] = 15% : 69% : 16%. In the further interpretation of the data, this should be taken into account.

B. Uniform-Loss Model

Our primary objective was to study the tunnel radiation field, especially the neutron fluence, under the cleanest possible conditions, i.e., with a steady stored beam of the longest possible lifetime. For such runs, an important mechanism of local beam loss is very probably proton collisions in the 4-m warm straight section, A-48, immediately upstream (Fig. 1). Runs having a steady measurable beam loss are also of interest, although the distribution of beam losses around the ring is unknown. A model of uniform beam loss around the entire circumference ($2\pi 1000$ m) would predict a direct neutron fluence at $d = 2$ m of $\phi_{dir} = 6\times10^{-6}$ neutrons cm^{-2} per proton lost (Fig. 14), if scattered neutrons are neglected. This is based on an estimated neutron production rate of 10 neutrons proton^{-1} GeV^{-1} (Pat73, p. 141), extrapolated from 10 GeV to the Tevatron energy. It is also assumed that 37% of the initial energy is available to the hadronic cascade; the remaining 63% is fed to the accompanying electromagnetic (EM) cascade via π^0 production.

Although undoubtedly too simple, this model serves as a useful reference for discussion. For a stored beam of 1×10^{11} protons and a nominal 100-hr beam lifetime ($1/\epsilon$), the uniform loss model translates to a direct fluence rate of $\dot{\phi}_{dir} = 1.67$ neutrons cm^{-2} sec^{-1} at $d = 2$ m. When corrected for the larger number of scattered neutrons the total fluence rate becomes $\dot{\phi}_{tot} = 1.67$ neutrons cm^{-2} sec^{-1} / 0.15 = 11 neutrons cm^{-2}sec^{-1} for a 100-hr beam lifetime. This is an average for the entire machine that is larger than the experimental result of 3.6 neutrons cm^{-2}sec^{-1} (Table 3) by a factor of 3.

The middle curve of Fig. 14 shows the expected direct neutron fluence rate at 2 m from the beam line for this model. The upper curve is based on the same model but is scaled by the ratio of total fluence (direct plus scattered) to direct fluence to account for the scattered component.

A prediction for the direct fluence rate from photoneutron production within the iron yoke is shown (lower curve of Fig. 14; see Appendix B). This assumes that 63% of the energy is in the electromagnetic cascade. It is probably acccurate to within a factor of two and is seen to fall below the direct fluence from the hadronic cascade by about a factor of 37. This is the basis of the statement that the photoneutron contribution is negligible compared to neutrons from hadronic interactions even at Tevatron energies.

For later comparison, the uniform loss model is calculated for the cold sections separately, assuming a pressure of 5×10^{-11} torr (1.15×10^{8} molecules cm^{-3}) of helium (100%) having a cross section of 135 mb (Edw85; also see Appendix A). For 1×10^{11} protons stored at 800 GeV, this implies 7.43×10^{-2} interactions cm^{-1} sec^{-1} or 220 neutrons cm^{-1} sec^{-1}. At the distance $d = 2$ m, Equation (9) gives:

$$\phi_{dir,cold}(2\text{ m}) = \frac{q'}{4\,d} = \frac{220\text{ neutrons cm}^{-1}\text{sec}^{-1}}{4\cdot 200\text{ cm}} = 0.275\text{ neutrons cm}^{-2}\text{ sec}^{-1} \qquad (10)$$

When correction is made for the fraction of scattered neutrons (15% are direct, 85% are scattered), we predict the total fluence at $d = 2$ m from a cold section to be:

$$\phi_{total,cold}(2\text{ m}) = 0.275\text{ neutrons cm}^{-2}\text{ sec}^{-1}\ /\ 0.15 = 1.83\text{ neutrons cm}^{-2}\text{ sec}^{-1}\ . \qquad (11)$$

C. Simulation with CASIM

The beam-gas interaction scenario in the A-48 straight section (warm) and dipole chain (cold; see Fig. 1) was modeled with the Monte Carlo code CASIM (VanG75a, b) using a simplified magnet geometry and field configuration (Fig. 15). Dipoles were modeled as hollow concentric iron cylinders of appropriate thickness and length. The field distribution, also shown in Fig. 15, was set at 3.5 T within the dipole vacuum pipe. An 8-mradian bend was provided by each dipole. A 5.18-m warm section was assumed to be uniformly filled with nitrogen gas (Z = 7, A = 14) to simulate the actual gas which is believed to be mainly CO (Jos86). The density was set at 7 mg cm^{-3} to provide a reasonable rate of primary beam-gas interactions but very few double interactions. The total cross section assumed was 357 mb per nucleus, of which 100 mb was elastic, to give an interaction rate of 5.57×10^{-2} per incident proton. Later the results were scaled to the actual gas density, 3.3×10^{-14}g cm^{-3} (assuming CO at 2×10^{-8} torr). Residual gas within the cold dipoles was neglected in this simulation. Protons at 800 GeV were incident on the warm section.

Figure 16 shows the radially-integrated star density, $dN(\text{stars})/dz$, and deposited energy density, dE_{dep}/dz, as functions of distance, z, from the warm section. In the units shown, stars/(m·proton) and GeV/(m·proton), the distributions are almost the same, with only a small difference (30%) for small z. This implies that each star corresponds to an average of about 1 GeV deposited energy. There is a strong decline in these functions with distance from the warm section -- about a factor of $1/e$ over 5.9 m. The radially-integrated energy density was parameterized as $dE_{dep}/dz = 3.5\exp(-0.17z)$ GeV/(m·proton) for positive z and zero for $z<0$.

Scaling was then performed by multiplying by the following factors:

- For the ratio of actual length of the warm section to the length assumed [4.00 m / 5.18 m] = 0.772.
- For the ratio of actual to assumed gas density: (3.3×10^{-14}g cm^{-3}/7×10^{-3}g cm^{-3}) = 4.70×10^{-12};

- For the actual gas mixtures, the cross sections (per molecule) of CO and H_2, weighted by the presumed proportions (see Appendix A): $[CO : H_2] = [(0.4\times775 \text{ mb} + 0.6\times84 \text{ mb}) / (775 \text{ mb})] = 0.465$.
- For 1.0×10^{11} protons stored: 4.775×10^{15} protons sec^{-1} incident on the warm section;
- A neutron source term given by 10 neutrons per GeV deposited (Pat73, p. 141);
- For the fraction of energy *not* lost to the EM cascade (Ran85): 0.37.

The combined scaling factor is 2.98×10^4, giving a neutron source rate distribution of:

$$\frac{d\dot{Q}}{dz} = 1.04\times10^5 \exp(-0.17z) \text{ neutrons m}^{-1}\text{sec}^{-1}, \tag{12}$$

for a primary beam interaction rate of 448 sec^{-1} in the warm section predicted for the real experiment. The *total* neutron source rate can be obtained from this model by integrating Equation (9) over all $z > 0$. It is $\dot{Q}_{tot} = 6.12\times10^5$ neutrons sec^{-1}.

By numerical integration along the dipole chain, the fluence of direct neutrons can be obtained for any location of a detector, (d, z_D), where d is the perpendicular distance from the beam line and z_D is the longitudinal coordinate. Figure 17(a) shows the differential direct neutron fluence rate, $d\dot{\phi}_{dir}/dz$, for detectors located at ($d = 2$ m; $z_D = 5$, 14 and 20 m). The points at $z_D = 14$ and 20 m correspond approximately to real locations of the detectors BF3-U and BF3-D, respectively [actual locations $z_D = 14$ and 19 m (Fig. 1)]. These distributions show that the effective source of *direct* neutrons at each location is very limited; the distributions of fluence contribution decrease by half within about 2.2 m on either side of the detector location.

Figure 17(b) shows the distribution of direct neutron fluence rate, $\dot{\phi}_{dir}(z_D)$ at $d = 2$ m as a function of z_D. This curve is precisely the integral over z of the functions $d\dot{\phi}_{dir}/dz$ of Fig. 17(a). The ratio of direct fluences at the two BF_3 detectors is predicted by this curve to be BF3-U/BF3-D = 2.0. This is larger than the observed ratio for coasting-beam conditions, 1.24 (Table 3). However the contribution of scattered neutrons would reduce this ratio.

The distribution of scattered neutrons is difficult to predict, but the gross contribution can be estimated at the median point of our counter array, $z_D = 16.5$ m. Using Fig. 17(b), we calculate $\dot{\phi}_{dir}(16.5 \text{ m}) / 0.15 = 0.28$ neutrons cm^{-2} sec^{-1} / 0.15 = 1.87 neutrons cm^{-2} sec^{-1}. This is lower than the experimental result of 3.6 neutrons $cm^{-2}sec^{-1}$ for 1×10^{11} protons under clean coasting beam conditions (Table 3) by about a factor of 1.9. Both the beam current and pressure in A-48 are each only known to within a factor of about 2, which could help to remove the discrepancy. The contribution from the chain of focussing elements downstream of the dipole chain (Fig. 1) is difficult to simulate and no attempt was made to do so. This could also be a source of neutrons. Except for the runs selected for "clean" coasting beam conditions of Table 3, ratios of BF_3 counts shown in Table 2 generally indicate a stronger source downstream from the counter array, rather than upstream.

D. Discussion of Models

The CASIM simulation just described presents the following problems:

- It underpredicts the observed fluence by a factor of about 1.9.
- It predicts a strong decline in ϕ_{dir} with z_D, which seems inconsistent with the observed ratio of BF_3 counts.
- If the conditions assumed within the warm section A-48 (composition, pressure) hold for every warm section (7% of the circumference and assuming zero gas pressure in the cold sections), a

beam lifetime of 564 hr would be predicted, much longer than the 70 - 100 hr observed at the time of the measurements.

Therefore the CASIM simulation, although probably representing a reasonable partial description, is incomplete and additional beam loss mechanisms are needed.

On the other hand, the uniform-loss model discussed in Section B above, for a 100-hr beam lifetime, would predict too many neutrons by a factor of about 3. However, this prediction is an average for the machine and might not apply locally.

A combination of the CASIM-simulation and a uniform-loss model for the cold section alone (Section B) would be consistent with the observed fluence rate:

$$\dot{\phi}_{CASIM} + \dot{\phi}_{tot,cold} = \tag{13}$$

$$1.87 \text{ neutrons cm}^{-2}\text{sec}^{-1} + 1.83 \text{ neutrons cm}^{-2}\text{sec}^{-1}$$

$$= 3.7 \text{ neutrons cm}^{-2}\text{sec}^{-1} ,$$

in good agreement with the observed fluence rate of 3.6 neutrons $cm^{-2}sec^{-1}$, and would give a ratio of BF_3 counts of BF3-U / BF3-D = 1.42. This is closer to the observed ratio of 1.24 for clean coasting beam conditions than is the CASIM model alone.

This excellent agreement is gratifying but, as there are uncertainties of a factor of 2 in both the beam current and in our analysis (particularly in our knowledge of the gas pressure), it may also be largely fortuitous.

If the identical beam-tube conditions assumed above (gas composition, pressure and cross sections) held for all the respective warm and cold sections around the ring circumference, the beam decay constant from beam-gas interactions would be 1.03×10^{-6} sec^{-1}, which corresponds to a lifetime ($1/e$) of 1.03×10^{6} sec = 287 hr. This is consistent with the observed lifetime of 70 - 100 hr but shows that mechanisms other than beam-gas scattering are contributing to beam loss.

In view of the approximations required in this analysis, and the non-rigorous treatment of scattered neutrons, it is clear that more elaborate modeling, as well as additional experimental study, with better monitoring and control of both beam current and gas pressure, are needed. Future experimental work should include a study of the fast neutron component along the tunnel (function of both d and z_D), in order to separate the direct from the scattered component.

E. Unclean Conditions

As noted above, our running conditions were chosen to be as clean as possible and as such they are more amenable to interpretation. Realistic accelerator conditions are not as clean, especially when injection and abort cycles are considered. These can be especially severe during machine commissioning. We were not able to study these non-pristine conditions in a controlled manner. However, we did note that, during injection into the Main Ring and transfer of beam from the Main Ring to the Tevatron at 150 GeV, neutron fields were so intense as to cause substantial pile-up and dead-time losses in our detectors. The attempt at measurements under these conditions was abandoned. On the other hand, single-turn resonant extraction to the abort dump located at C-0 (60 degrees or 1047 m downstream) was executed without noticable increase in the radiation field in our area.

F. Doses to Silicon

The photon doses discussed above are for LiI, whereas the neutron absorbed dose is for tissue. For an assessment of possible radiation damage to inorganic materials, we should convert both dose contributions to a common reference material, silicon.

For photon doses, we scale by the ratio of mass-energy absorption coefficients μ_{en}/ρ for the two materials silicon and LiI at the energy of ^{60}Co radiation (1.25 MeV): $[\mu_{en}/\rho\ (\mathrm{Si})]\ /\ [\mu_{en}/\rho\ (\mathrm{LiI})] = (2.65 \times 10^{-3}\ /\ 2.44 \times 10^{-3}) = 1.09$ (see, for example, Hub82). As the correction is not great, and μ_{en}/ρ does not vary much in the photon energy region in question, this correction is accurate enough.

The conversion of neutron absorbed dose from tissue to silicon is not so simple because the kerma factors for both tissue and silicon vary rapidly over the relevant spectral range. For that reason a special numerical integration over the spectrum was performed in a mesh of 118 points from thermal energies (0.0247 eV) to 30 MeV. This was done using values of the kerma factor tabulated by Caswell et al. (Cas80), folded together with spectra determined by LOUHI. The result of each integration, the total kerma, is assumed to represent the absorbed dose. The kermas for the two materials are divided and the average ratios shown in Table 7 for three kinds of running conditions. These ratios agree within the observed standard deviations. The average over the three types of runs is 22.0.

Table 7. Ratio of kerma in tissue to kerma in silicon for observed spectra.

Running Conditions	Ratio: $\bar{k}_{f\ (tiss)}/\bar{k}_{f\ (Si)}$	Runs Averaged
Tevatron 800 GeV	18.9	4
Tevatron 150 GeV	22.0	5
Main Ring (accel. 8 - 150 GeV)	25.2	1
Average of above	22.0	—

G. Summary of Tunnel Radiation Components

Table 8 is a summary of the principal components of the Tevatron radiation field as observed by us for coasting beam conditions. Each quantity is averaged over several runs. Because we were positioned to the interior of the Tevatron ring, muons, which contribute a significant component to the radiation field mostly in tangential directions, were not observed by us. Uncertainty in normalization to beam intensity is probably a factor of two. Table 9 contains a similar summary for Main Ring operation. The quantities of Tables 8 and 9 have been defined and discussed in previous sections.

We emphasize that the absorbed dose values ascribed to photons and minimum ionizing particles are upper limits; doses to our counters due to direct interactions of neutrons above thermal energy have not been subtracted and these could account for a substantial part of the absorbed dose to LiI. It is known that, for neutrons incident on hydrogenous materials (tissue), over a broad energy range (thermal to at least 5 MeV), a considerable absorbed dose is generated from the neutron capture gamma rays (NCRP71). This amounts to a photon dose (divided by neutron fluence) of $(4 - 5)\times 10^{-10}$ rad neutron^{-1} cm^2. The upper limits on photon doses, shown in Tables 8

and 9 are higher than this and therefore are consistent with these earlier determinations.

Table 8. Characteristics of the Tevatron neutron field at 2m from beam line for coasting-beam conditions.

Quantity	Units	Value	
		800 GeV	150 GeV
Quantities independent of beam monitor:			
Median energy (fluence)	MeV	0.059	0.11
Median energy (abs.dose)	MeV	0.610	0.49
Quality factor	rem/rad	6.9 ± 0.5	7.6 ± 0.5
Kerma factor (k_f , tissue)	rad cm^2	$(2.0 \pm 0.3)\times10^{-9}$	$(1.7\pm0.3)\times10^{-9}$
Kerma factor (k_f , silicon)	rad cm^2	$(1.1 \pm 0.2)\times10^{-10}$	$(7.7\pm1.3)\times10^{-11}$
Effective energy (k_f , tissue)	MeV	0.82	0.58
D_γ (LiI) / ϕ_n	rad cm^2	$< (1.8\pm0.6)\times10^{-9}$	$< 2.2\times10^{-9}$
D_{mip} (LiI) / ϕ_n	rad cm^2	$< (1.6\pm0.6)\times10^{-10}$	$< 2.5\times10^{-10}$
Quantities normalized to 10^{11} circulating protons (T:IBEM1 Monitor):			
Fluence rate ($\dot{\phi}_n$)	neutrons cm^{-2} sec^{-1}	3.6	4.7

H. Comparison with Other Calculations

It is interesting to compare our spectra with others in the literature. The Monte-Carlo calculations of Gabriel and Santoro (Gab71) produced particle spectra within a 1-m deep volume of soil at the end of a long narrow tunnel (600 m $\times$ 0.9 m diam) following a 1-interaction length Be target struck by 500 GeV protons (Fig. 18). On the other hand, our measurements were made at a location 2 m from an iron-filtered line source in a 3.05-m diameter tunnel. The spectral similarity consists in the enormous component of slowing-down neutrons ($\approx 1/E$) which clearly dominates the Monte Carlo calculation. The difference is in the absence of a strong 0.2 - 0.3 MeV peak in the calculated lethargy distribution, which is very prominent in the experimental distributions. The peak must therefore be ascribed to the effect of the iron.

I. Extrapolation to SSC Energies

A crude estimate of the neutron absorbed dose rate expected during SSC (SSC86) operation can be obtained from the above value of the dose rate. The circumference of the SSC accelerator

Table 9. Characteristics of the Main Ring neutron field at 2m from beam line.

Quantity	Units	Value
Quantities independent of beam monitor		
Median energy (fluence)	MeV	0.03
Median energy (abs.dose)	MeV	0.48
Quality factor	rem/rad	7.2 ± 0.5
Kerma factor (k_f , tissue)	rad cm^2	$(1.43\pm0.3)\times10^{-9}$
Kerma factor (k_f , silicon)	rad cm^2	$(5.7\pm1.0)\times10^{-11}$
Effective energy (k_f , tissue)	MeV	0.38
D_γ (LiI) / ϕ_n	rad cm^2	$< 1.5\times10^{-9}$
D_{mip} (LiI) / ϕ_n	rad cm^2	$< 0.9\times10^{-10}$
Quantities normalized to 10^{11} accelerated protons (approx.):		
Fluence ϕ_n	neutrons cm^{-2}	147

ring is assumed to be 83 km, 13.2 times that of the Tevatron, so that the time for one revolution of a proton bunch around the SSC ring is about 277μsec (vs. 21μsec for the Tevatron). If the neutron absorbed dose rate is assumed to scale linearly with energy from 800 GeV to 20 TeV, then, for two stored SSC beams of 1.27×10^{14} protons each, we find that conditions in the SSC tunnel would be about 4800 times as severe. If the estimated reduction in energy available to the hadronic cascade (escape to the EM cascade) is taken into account, the severity is somewhat diminished. Assuming simple energy scaling and equal beam-tube pressures, an estimate of the neutron dose rate (tissue), $\dot{D}_n$, gives:

$$\dot{D}_n\,(tissue\,,SSC) = 0.026 \text{ mrad hr}^{-1}\times\left(\frac{20 \text{ TeV}}{0.8 \text{ TeV}}\times\left[\frac{2.54\times10^{14} \text{ protons}}{1.00\times10^{11} \text{ protons}}\right]\times\frac{21\mu\text{sec}}{277\mu\text{sec}}\right) \quad (14)$$
$$= 0.026\times[4800] = 125 \text{ mrad hr}^{-1} .$$

To convert the projected tissue dose rate to the dose rate in silicon, we use the average kerma factors $\bar{k}_f\,(tiss\,)\,/\bar{k}_f\,(Si\,) = 22.0$ from Table 7. This gives

$$\dot{D}_n\,(Si\,,SSC) = \frac{\dot{D}_n\,(tiss\,,SSC)}{22.0} = \frac{125 \text{ mrad hr}^{-1}}{22.0} = 5.7 \text{ mrad hr}^{-1} . \quad (15)$$

For analysis of potential damage to electronics in the SSC tunnel, the average neutron fluence rate is also relevant. From Table 8:

$$\dot{\phi}_n\,(SSC) = 4800\times\dot{\phi}_n\,(\text{Tevatron}) = 4800\times3.6 \text{ cm}^{-2}\text{ sec}^{-1} \quad (16)$$
$$= 1.73\times10^4 \text{ neutrons cm}^{-2}\text{ sec}^{-1}.$$

VII. CONCLUSIONS

The object of this investigation was to study the radiation environment in the tunnel of an operating high energy proton accelerator. Primary attention was given to the neutron field, because it is potentially the most detrimental to electronic equipment. The following observations are derived from this study:

1. The neutron spectra obtained under different conditions, i.e., different energies (and even different accelerators within the Tevatron tunnel), are strikingly similar.

2. The spectra are surprisingly soft and they contain prominent peaks in the lethargy distributions centered at about 0.23 and 0.26 MeV for the Tevatron and Main Ring, respectively (the apparent difference is not significant), as well as at thermal energies.

3. High-energy neutrons are relatively unimportant compared to the lower energy neutrons, with only about 10 % and 1 % of the fluence found above 2 and 50 MeV, respectively.

4. The above observations suggest a common 'filter' for the neutrons, regardless of the nature of the original interactions which produce the parent cascade. Prominent parts of the filter must be the iron magnet yokes as well as the concrete tunnel lining.

5. From the observed fluence rate and the relative uniformity of fluence, it seems unlikely that neutrons observed by us can be explained by the model based on primary beam-gas interactions in the warm section A-48 alone. The addition of a second type of neutron source based on a uniform distribution of beam-gas interactions in the adjacent cold dipole chain, that contributes about half of the fluence at our detector location, would give predictions fully consistent with our observations.

6. Because of their capability of producing lattice defects and transmutations, neutrons are shown to be the most important potential cause of radiation damage to solid state electronic devices in accelerator tunnel environments similar to ours. However we cannot exclude the possibility that, in cases where substantial absorption of the hadronic cascade is not provided, other radiation components may be more important in this regard.

An interesting question is whether, to a first approximation, all types of absorbed dose are neutron-related in tunnel geometries similar to ours; components coming directly from the beam line other than those carried by neutrons may be unimportant in comparison. If so, it seems certain that the iron magnet yoke provides an essential filter in that it allows fast neutrons to escape with relatively little attenuation while it effectively absorbs the hadronic and EM cascades. This question deserves additional attention, both by more detailed simulations and by additional experimental work.

Our results regarding neutron spectra are of great utility for the design of thin shields, alcoves, labyrinths and other penetrations. They also serve as an experimental benchmark for theoretical studies of the hadronic cascade. As noted in several places, there is good evidence that the neutron spectrum at our location was subject to filtering both by magnets and by reflections in the concrete tunnel. It may be that, under the conditions of much thinner shielding, a considerably harder spectrum may be found. There is evidence for this in the CERN-LRL-RHEL experiment (Gil68), in which threshold detectors mounted in the accelerator tunnel with direct view of a beam stop found a neutron spectrum more representative of the first generations of a hadronic cascade.

VIII. FUTURE STUDIES

Based on the knowledge gained so far, we believe it desirable to extend this work by additional measurements which would incorporate the following features:

a) The primary source should be uniquely defined and controlled by the experimenters (flying wire or localized pressure rise).

b) Gated detectors designed specifically to determine photon and charged particle doses separately should be included along with the neutron detectors.

c) Flexibility in location of detectors should permit a number of locations to be used, including some nearer the beam to study radiation at small angles, and to separate the direct neutron fluence from the scattered.

IX. ACKNOWLEDGEMENTS

The authors would like to express their gratitude to persons whose efforts were instrumental in making these measurements possible. In particular, J. Richie Orr and others of the Fermilab Staff, including V. Dixon Bogert, Larry Coulson, Donald A. Edwards and Frank A. Nezrick were most hospitable and cooperative. We are especially grateful to David G. Beechy for designing special gating logic and to John E. Elias for helpful discussions. Of the SSC Central Design Group, under the direction of Maury Tigner, we would like to mention Donald E. Groom, Peter J. Limon, James R. Sanford and Timothy E. Toohig. Those of us from Lawrence Berkeley Laboratory thank Alan R. Smith for valuable advice and Ralph H. Thomas and Jensen Young for support and encouragement.

REFERENCES

Aws85 M. Awschalom and R. Sanna, Applications of Bonner sphere detectors in neutron fields, Radiation Prot. and Dosimetry 10, 89 (1985).

Bee85 D. G. Beechy, Internal memorandum addressed to D. Bogert, A. Elwyn and B. Freeman, dated 8 August 1985, Fermi National Accelerator Laboratory.

Bra60 R. L. Bramblett, R. L. Ewing and T. W. Bonner, A new type of neutron spectrometer, Nucl. Instr. Meth. 9, p. 1 (1960).

Cas80 R. S. Caswell, J. J. Coyne and M. L. Randolph, Kerma factors for neutron energies below 30 MeV, Radiation Research 83, 217 (1980).

Cha83 D. A. Chambless and J. A. Broadway, Comments on "Neutron spectral unfolding using the Monte Carlo method", Nucl. Instr. Meth. 214, 543 (1983).

Cos85 J. D. Cossairt, J. G. Couch, A. J. Elwyn and W. S. Freeman, Radiation measurements in a labyrinth penetration at a high energy proton accelerator, Health Physics 49, 907 (1985).

Edw85 H. T. Edwards, The Tevatron energy doubler, Ann. Rev. Nucl. Part. Sci. 35, 605 (Annual Reviews Inc., Palo Alto, CA, 1985).

Edw86 H. T. Edwards, private communication, Fermi National Accelerator Laboratory, Batavia, IL (1986).

Eis82 C. M. Eisenhauer, R. B. Schwartz and T. Johnson, Measurement of neutrons reflected from the surface of a calibration room, Health Physics 42, 489 (1982).

Gab71 T. A. Gabriel and R. T. Santoro, Calculation of the long-lived activity in soil produced by 500-GeV protons, Nuclear Instr. Methods 95, 275 (1971).

Gil68 W. S. Gilbert, D. Keefe, J. B. McCaslin, H. W. Patterson, A. R. Smith, L. D. Stephens, K. B. Shaw, G. R. Stevenson, R. H. Thomas, R. D. Fortune and K. Goebel, The 1966 CERN-LRL-RHEL Shielding Experiment at the CERN Proton Synchrotron, Lawrence Radiation Laboratory, Report No. UCRL-17941, Berkeley, CA (1968).

Hub82 J. H. Hubbell, Photon mass attenuation and energy absorption coefficients from 1 keV to 20 MeV, Int. J. Appl. Radiat. Isot. 33, 1269 (1982).

ICRP73 International Commission on Radiological Protection, Data for Protection Against Ionizing Radiation from External Sources: Suppplement to ICRP Publication 15, ICRP Publication No. 21, Pergamon Press, Oxford (1973).

ICRU80 International Commission on Radiation Units and Measurements, Radiation Quantities and Units, ICRU Report No. 33, Washington, D. C. (1980).

Jos86 H. Jostlein, private communication, Fermi National Accelerator Laboratory, Batavia, IL 60510 (1986).

McC79 R. C. McCall, T. M. Jenkins and R. A. Shore, Transport of accelerator produced neutrons in a concrete room, IEEE Trans. Nucl. Sci. NS-26, 1593 (1979).

NCRP71 National Council on Radiation Protection and Measurements, Protection Against Neutron Radiation, NCRP Report No. 38, Washington, D.C. (1971).

OBr81 K. O'Brien and R. Sanna, Neutron spectrum unfolding using the Monte Carlo method, Nucl. Instr. Meth. 185, 277 (1981).

OBr83 K. O'Brien and R. Sanna, Reply to Chambless and Broadway, Nucl. Instr. Meth. 214, 547 (1983).

Pat58 H. W. Patterson and R. Wallace, A Method of Calibrating Slow-Neutron Detectors, Report No. UCRL-8359, Lawrence Radiation Laboratory, Berkeley, CA 94720 (1958).

Pat73 H. W. Patterson and R. H. Thomas, Accelerator Health Physics, (Academic Press, New York, 1973).

PDG84 Particle Data Group, Particle Properties Data Booklet, from Review of Particle Properties, Rev. Mod. Phys. 56, No. 2, Part II (April 1984).

Ran85 J. Ranft, private communication, Karl Marx University, Leipzig (1985).

Ros56 B. Rossi, High Energy Particles (Prentice-Hall, Englewood Cliffs, NJ, 1956).

Rou80 J. T. Routti and J. V. Sandberg, General purpose unfolding program LOUHI 78 with linear and nonlinear regularisations, Compt. Phys. Commun. 21, 119 (1980).

San73 R. S. Sanna, Thirty-one Group Response Matrices for the Multisphere Neutron Spectrometer over the Energy Range Thermal to 400 MeV, U.S. Atomic Energy Commission, Health and Safty Laboratory, Report HASL-267 (1973).

Smi85 A. R. Smith, private communication, Lawrence Berkeley Laboratory, Berkeley, CA (1985).

SSC86 SSC Central Design Group, J. D. Jackson, ed., Conceptual Design of the Superconducting Super Collider, Lawrence Berkeley Laboratory, Report SSC-SR-2020 (March, 1986).

Sun86 R. K. Sun, Photon-Energy Calibration of LiI Crystals Using $_{11}Na^{24}$, Lawrence Berkeley Laboratory, Health Physics Note LBL-HPN-143 (August, 1986). To be submitted to Health Physics.

VanG75a A. Van Ginneken and M. Awschalom, High Energy Particle Interactions in Large Targets, Fermi National Accelerator Laboratory, Batavia, IL (unumbered, undated volume in small format; 1975).

VanG75b

A. Van Ginneken, Program to Simulate Transport of Hadronic Cascades in Bulk Matter, Fermi National Accelerator Laboratory, Report No. FN-272 (1975).

FIGURE CAPTIONS

Fig. 1. Plan view of experimental setup in the tunnel. Beam direction (for protons) was left to right. (a) overall view; (b) detail of detector geometry. Solid circles: LiI(Eu) detectors; squares: moderated BF_3 counters. Numbers indicate the polyethylene sphere diameter in inches. Th and Bi fission counters were positioned near the 10" and 12" spheres.

Fig. 2. Tunnel cross section showing relationship of detectors to Tevatron and MR.

Fig. 3. Functional block diagram of detectors and electronics.

Fig. 4. Typical pulse height distribution for the 7.62-cm (3-inch) Bonner sphere.

Fig. 5. Comparison of measured (points) and calculated detector response (solid curve) for actual neutron spectrum from 800-GeV coasting beam. Other curves show relative response of detectors as a function of sphere diameter for three representative energy intervals.

Fig. 6. Comparison of spectra derived from three unfolding codes, BUNKI, LOUHI and SWIFT, for Tevatron 800-GeV coasting beam.

Fig. 7. Unfolded spectrum from program LOUHI for a Tevatron run with coasting beam at 800 GeV.

Fig. 8. Spectrum of preceding figure expressed as cumulative percentage of fluence and tissue absorbed dose.

Fig. 9. Unfolded spectrum from LOUHI for a Tevatron run at 150 GeV.

Fig. 10. Spectrum of preceding figure expressed as cumulative percentage of fluence and tissue absorbed dose.

Fig. 11. Unfolded spectrum from LOUHI for a Main-Ring run (average over various energies during boost from 8 to 150 GeV).

Fig. 12. Spectrum of preceding figure expressed as cumulative percentage of fluence and tissue absorbed dose.

Fig. 13. Observed pulse height distribution (points, logarithmic ordinate) for the bare LiI crystal, showing idealized pulse height distribution for minimum ionizing particles in a cylindrical crystal (solid curve) and curve of the form E_γ^{-2} (dashed) hypothesized for photon spectrum.

Fig. 14. Estimate of fluence rate at 2 m for a uniform loss of 800 GeV protons around ring circumference (2π 1000 m). Assumed division of energy: [EM cascade : Hadronic cascade] = 63% : 37%. Lower line: Estimate of direct fluence rate of photoneutrons; Center line: Direct fluence rate from the hadronic cascade; Upper line: total fluence rate including scattered.

Fig. 15. Geometry used for CASIM simulation of experimental arrangement (not to scale and transverse dimensions exaggerated). (a) Magnetic field off, showing dipole cross section assumed; (b) Magnetic field on, showing idealized field distribution. Field is assumed uniform within each of 7 regions. Orbit is bent by 8 mradian in each dipole.

Fig. 16. CASIM Monte-Carlo calculations for radially-integrated star density, $dN(\text{stars})/dz$ and energy deposited, dE_{dep}/dz, in dipole magnets as functions of distance from the warm section. Straight line is a parameterization of the energy deposited, dE_{dep}/dz.

Fig. 17. (a) Calculations based on parameterization of previous figure showing direct-fluence source distribution along dipole chain, $d\dot{\phi}/dz$, at detector locations ($d = 2$m; and $z_D = 5$, 14 and 20m). Abscissa is the distance, z, from the warm section. Integral of curve for each detector location, z_D, gives:

(b) Neutron direct fluence rate, $\dot{\phi}$ at $d = 2$m as a function of z_D, based on integrals of panel (a).

Fig. 18. Hadron spectra within earth at end of a concrete-lined target tunnel. Incident proton energy: 500 GeV. [Adapted from Monte Carlo calculation of Gabriel and Santoro (Gab71)].

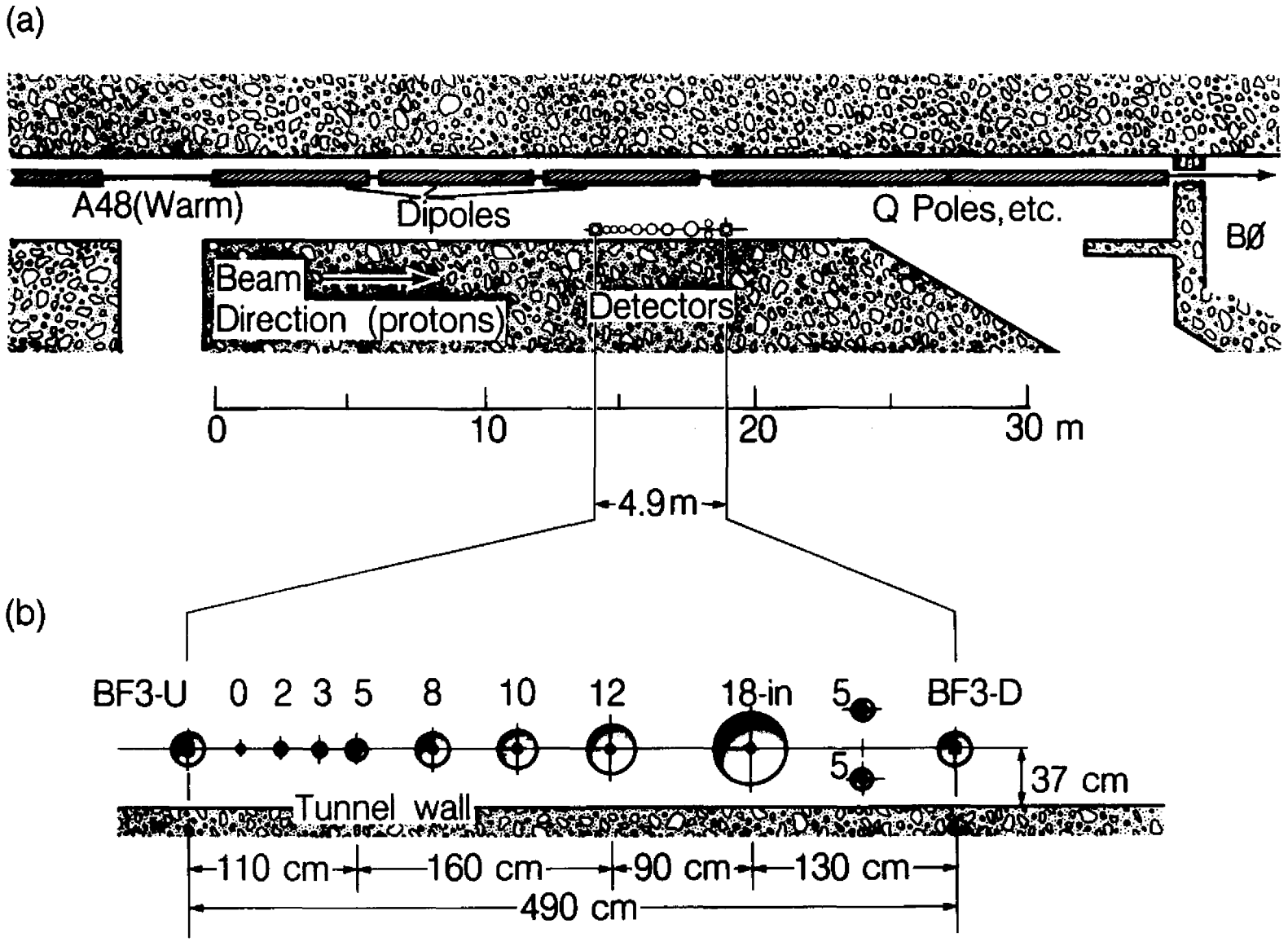

Fig. 1. Plan view of experimental setup in the tunnel. Beam direction (for protons) was left to right. (a) overall view; (b) detail of detector geometry. Solid circles: LiI(Eu) detectors; squares: moderated BF_3 counters. Numbers indicate the polyethylene sphere diameter in inches. Th and Bi fission counters were positioned near the 10" and 12" spheres.

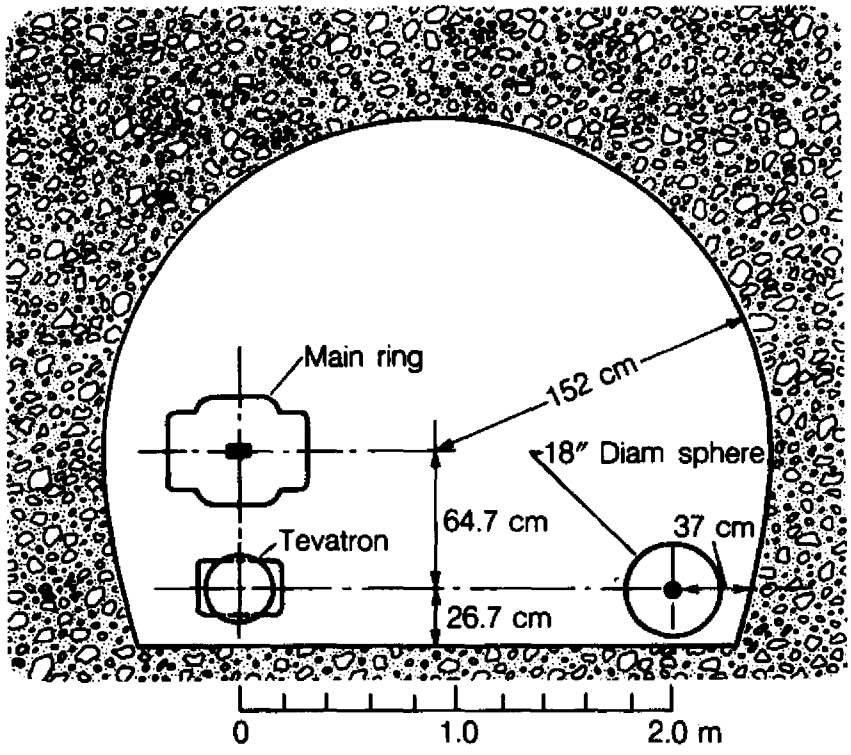

Fig. 2. Tunnel cross section showing relationship of detectors to Tevatron and MR.

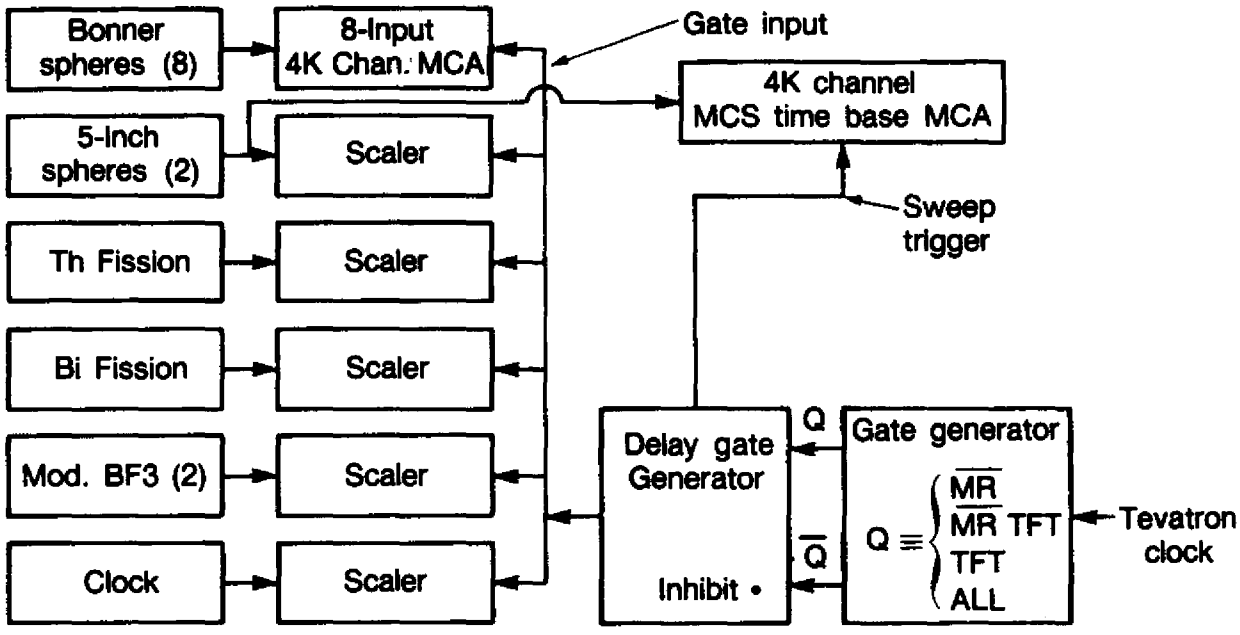

XBL 868-12007

Fig. 3. Functional block diagram of detectors and electronics.

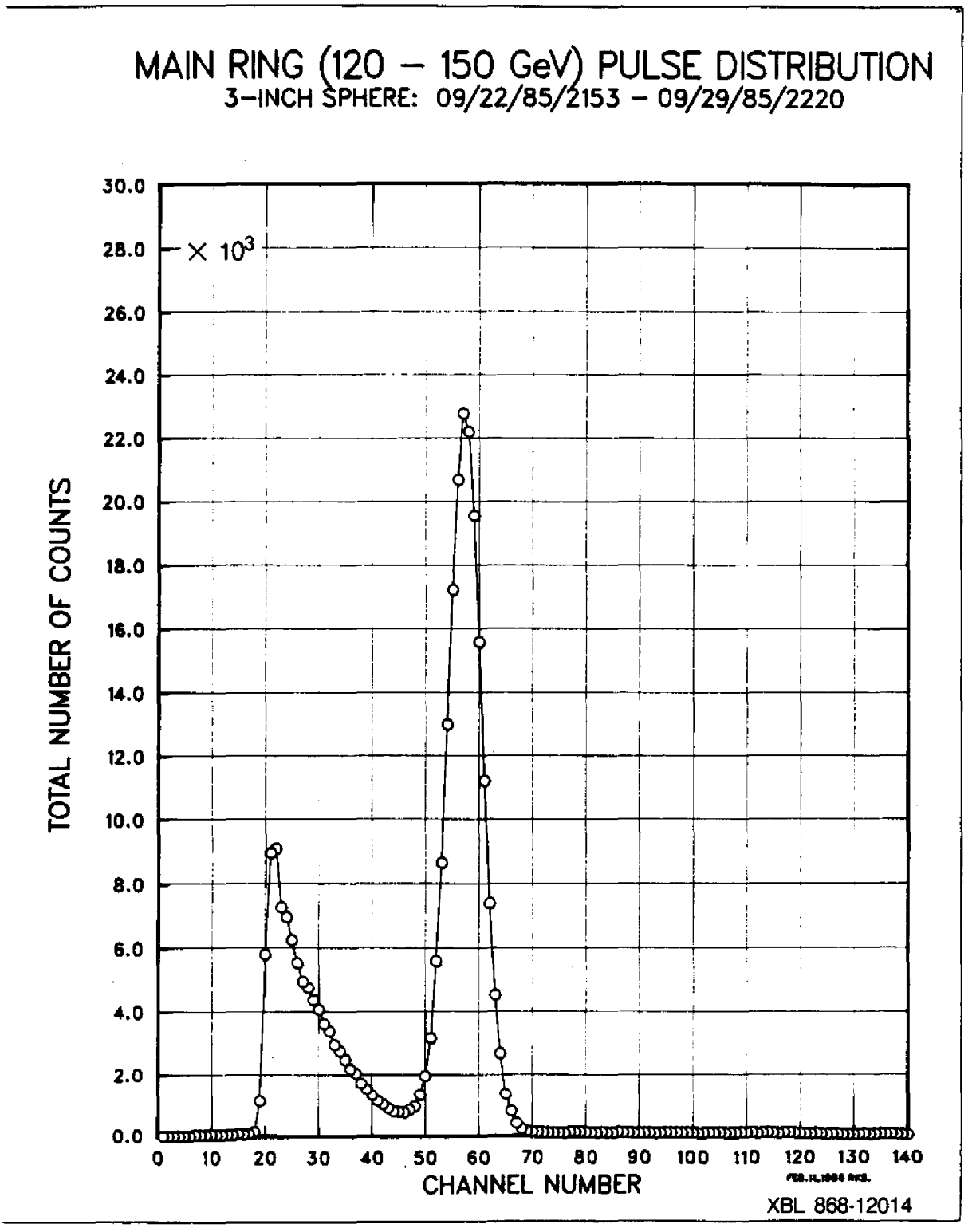

Fig. 4 Typical pulse height distribution for the 7.62-cm (3-inch) Bonner sphere.

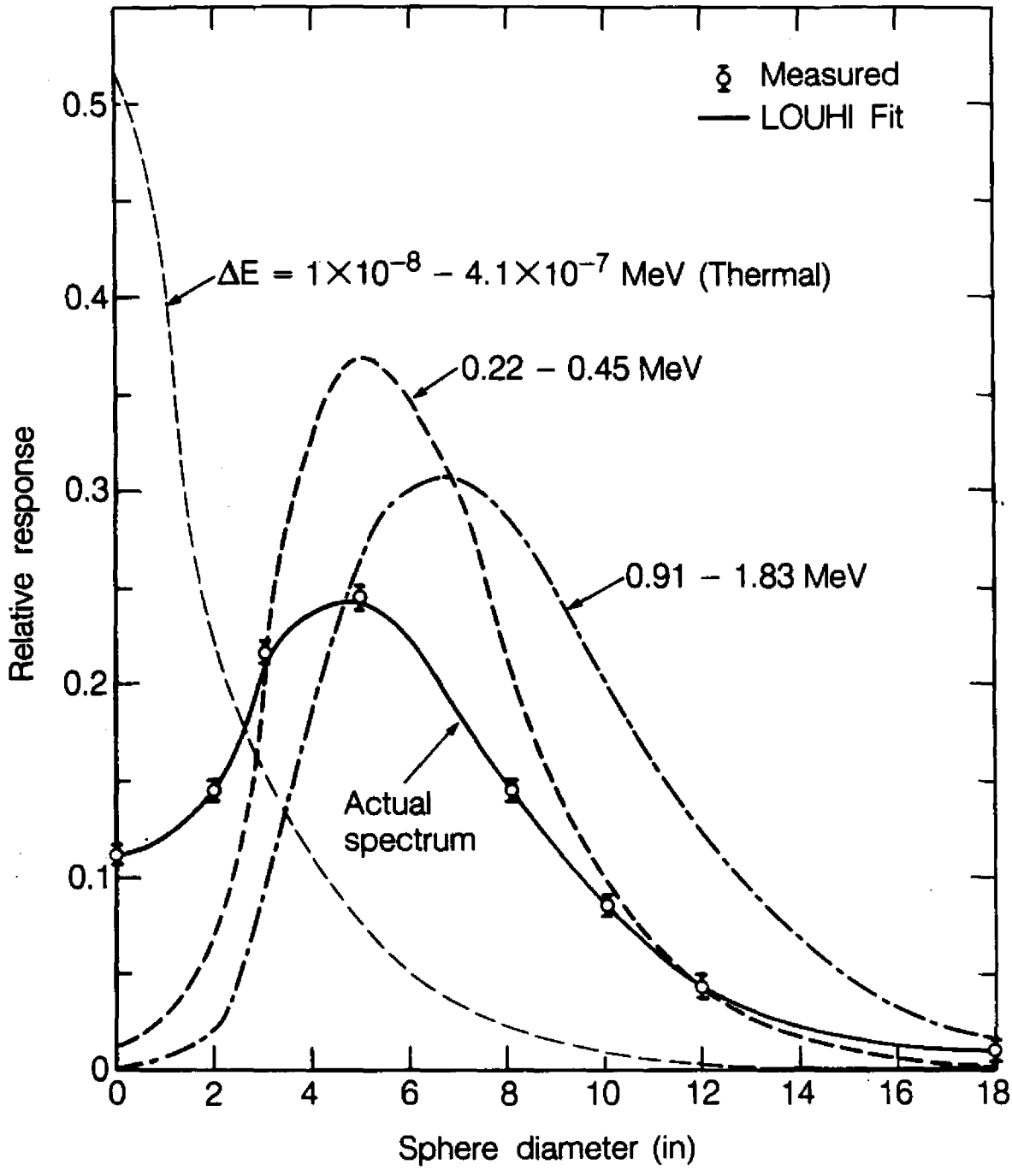

XBL 868-12018

Fig. 5 Comparison of measured (points) and calculated detector response (solid curve) for actual neutron spectrum from 800-GeV coasting beam. Other curves show relative response of detectors as a function of sphere diameter for three representative energy intervals.

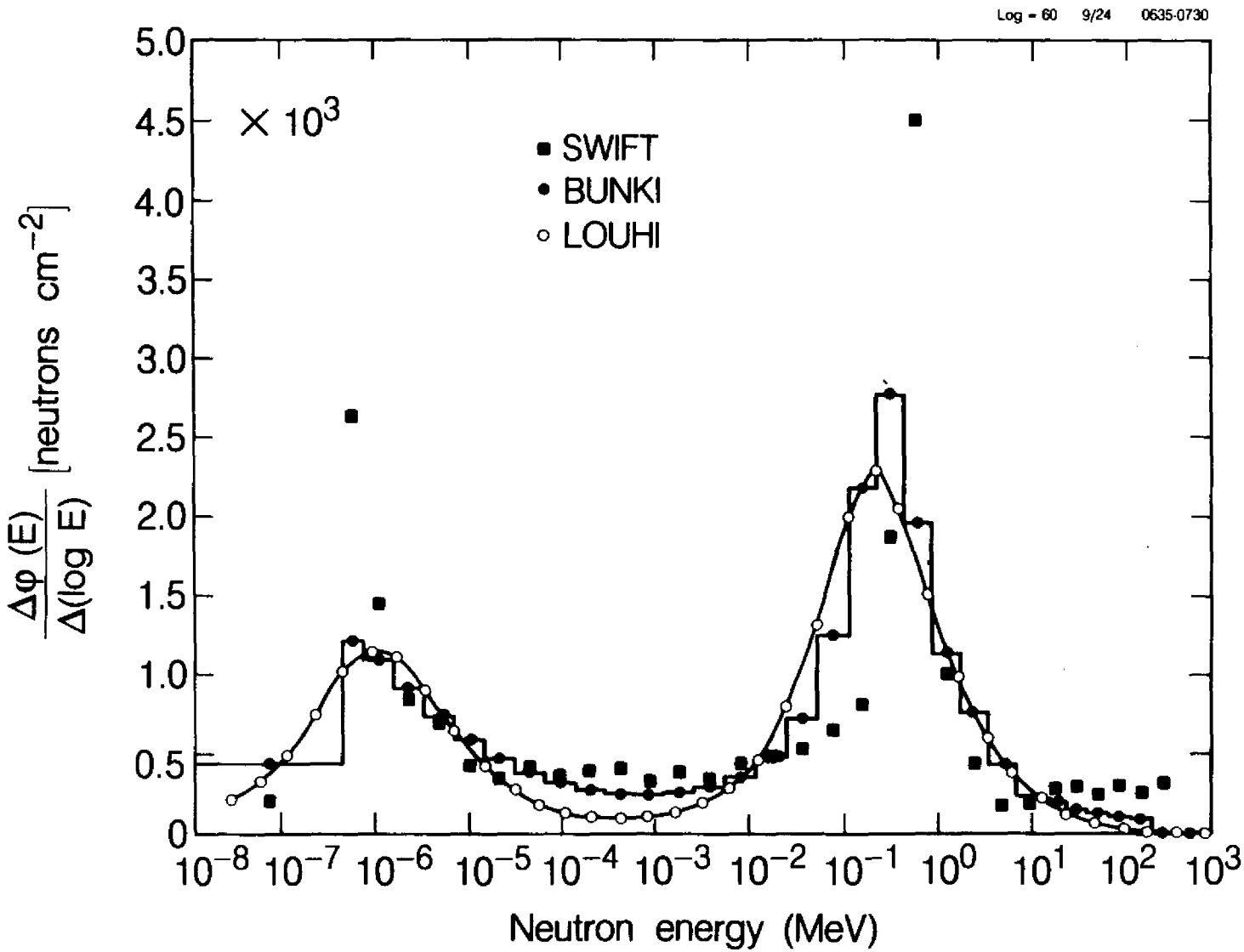

Fig. 6 Comparison of spectra derived from three unfolding codes, BUNKI, LOUHI and SWIFT, for Tevatron 800-GeV coasting beam.

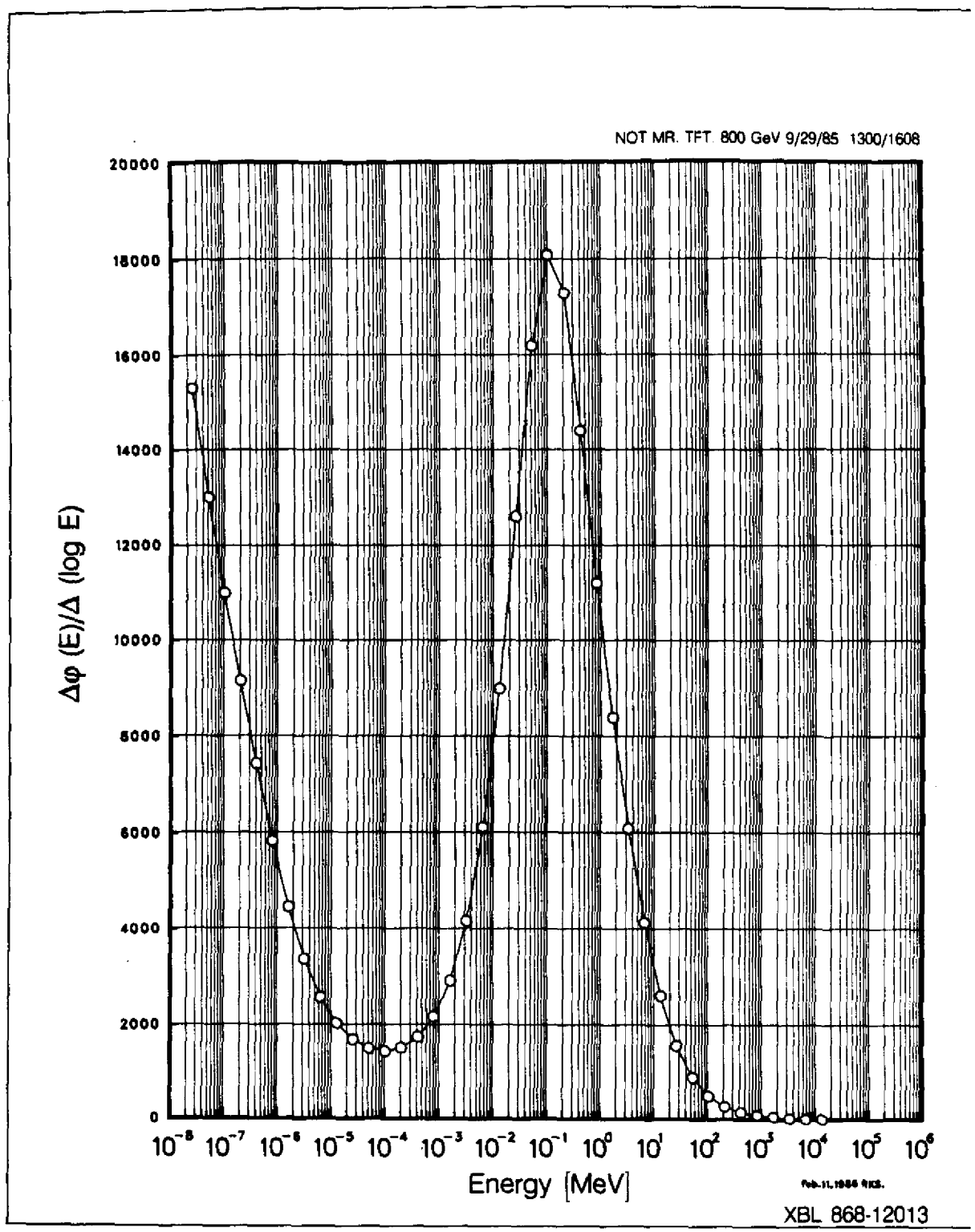

Fig. 7 Unfolded spectrum from program LOUHI for a Tevatron run at 800 GeV.

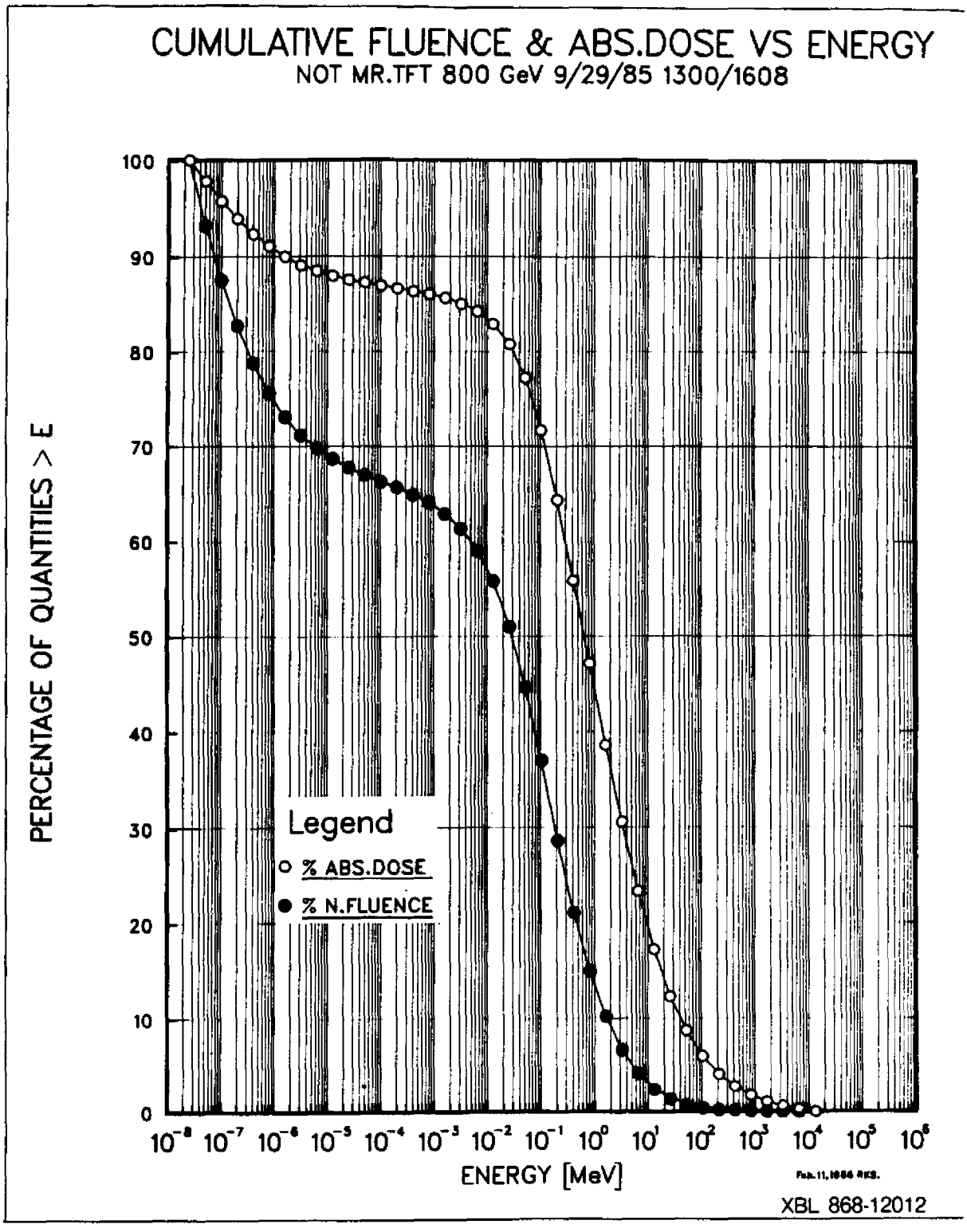

Fig. 8. Spectrum of preceding figure expressed as cumulative percentage of fluence and tissue absorbed dose.

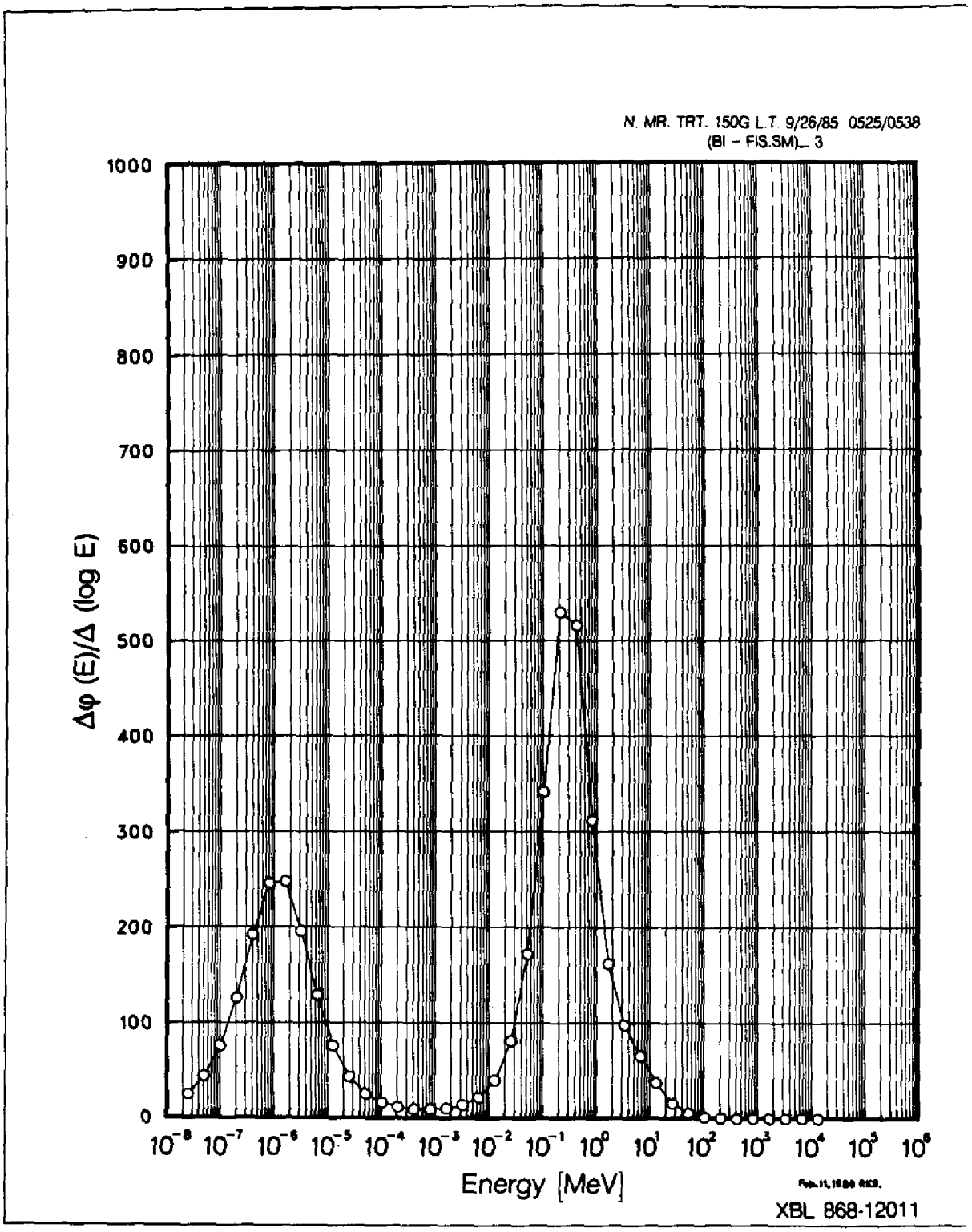

Fig. 9 Unfolded spectrum from LOUHI for a Tevatron run at 150 GeV.

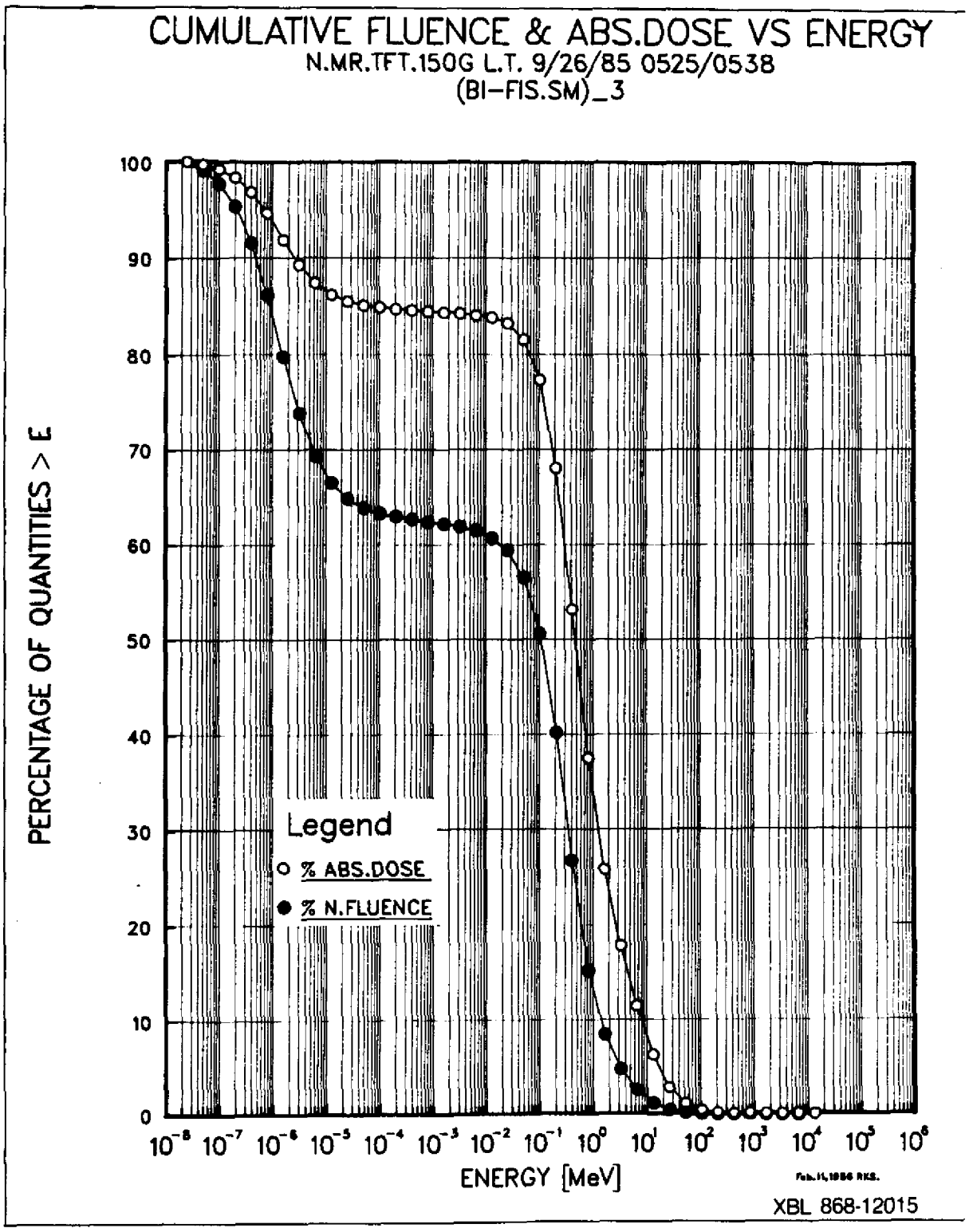

Fig. 10. Spectrum of preceding figure expressed as cumulative percentage of fluence and tissue absorbed dose.

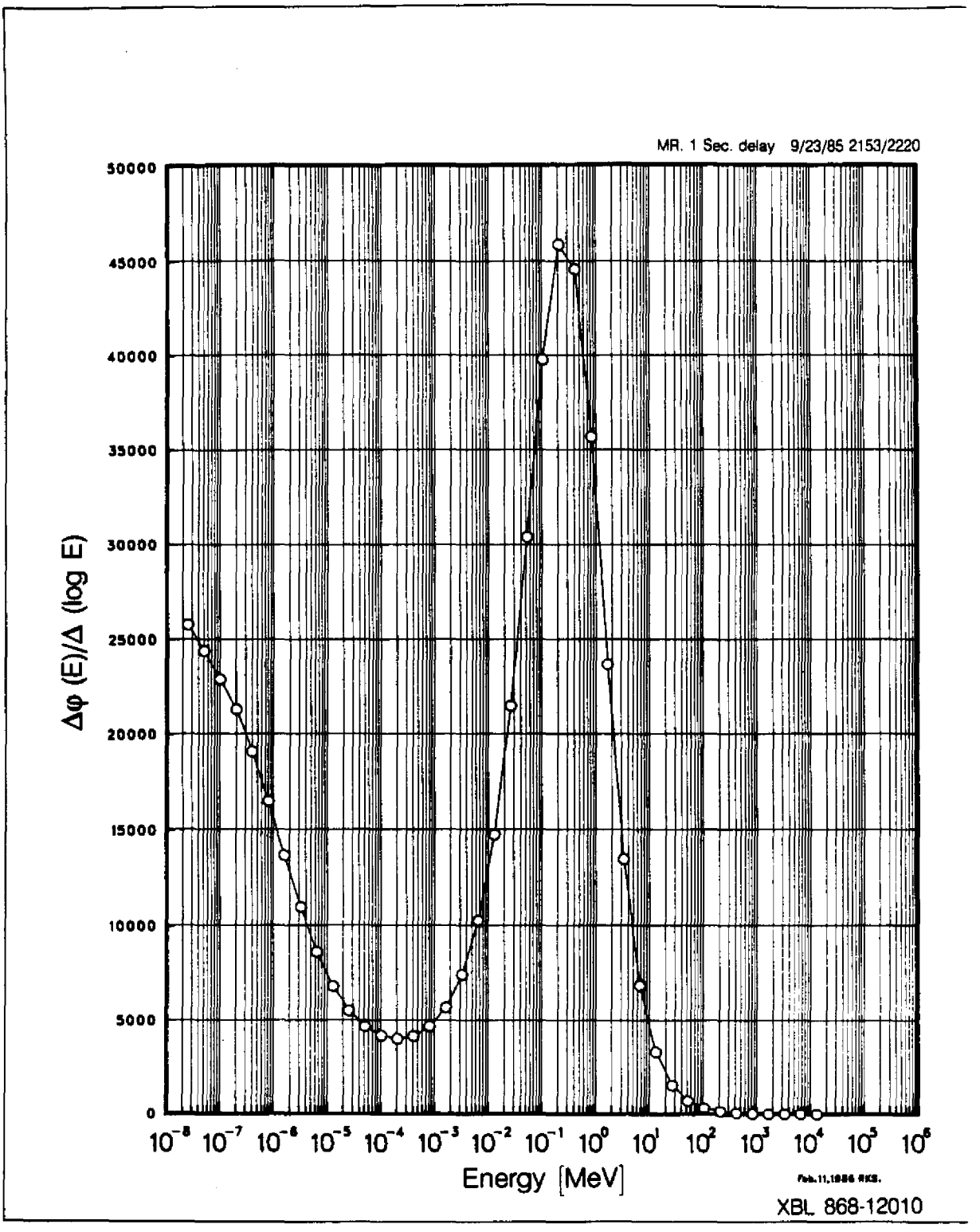

Fig. 11 Unfolded spectrum from LOUHI for a Main-Ring run (average over various energies during boost from 8 to 150 GeV).

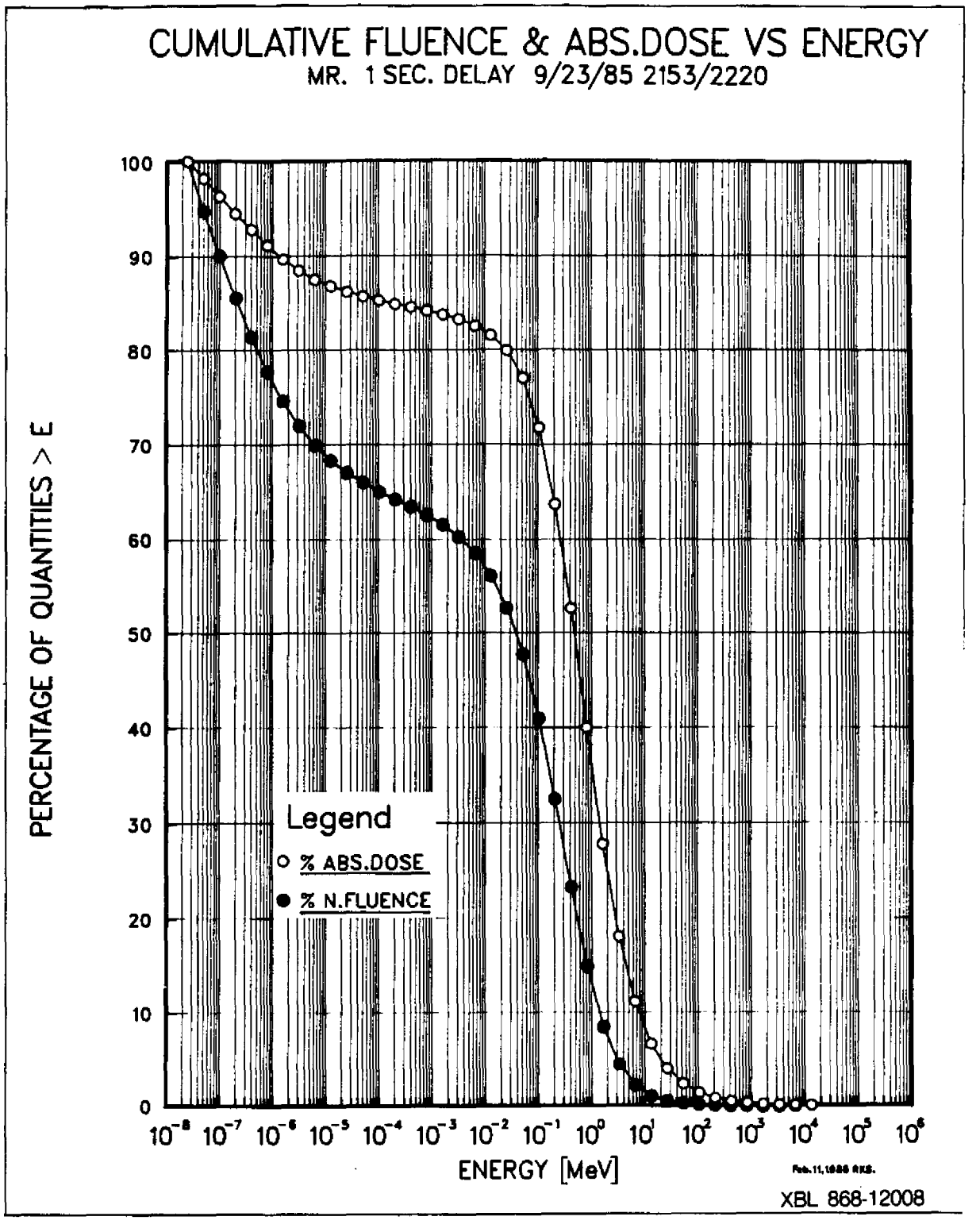

Fig. 12. Spectrum of preceding figure expressed as cumulative percentage of fluence and tissue absorbed dose.

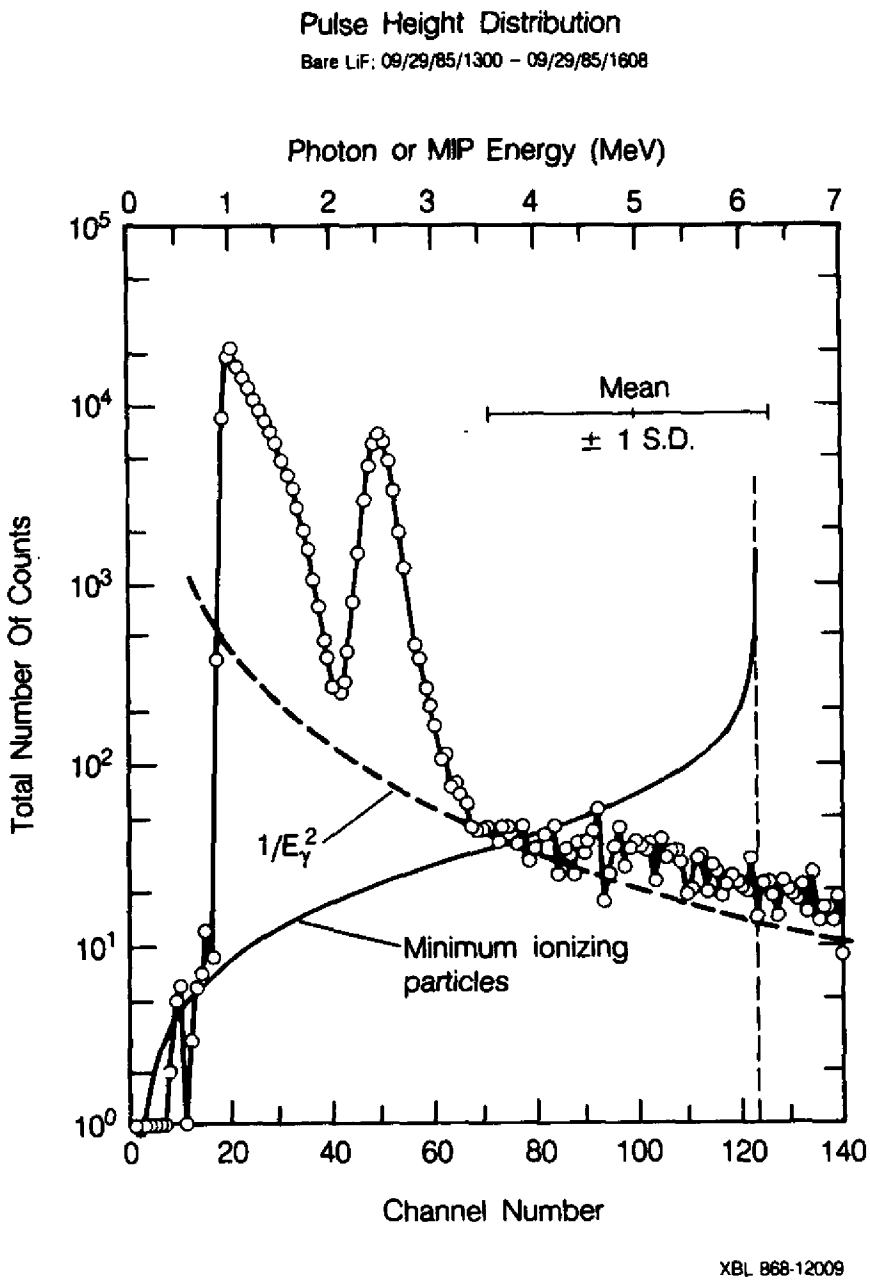

Fig. 13. Observed pulse height distribution (points, logarithmic ordinate) for the bare LiI crystal, showing idealized pulse height distribution for minimum ionizing particles in a cylindrical crystal (solid curve) and curve of the form E_γ^{-2} (dashed) hypothesized for photon spectrum.

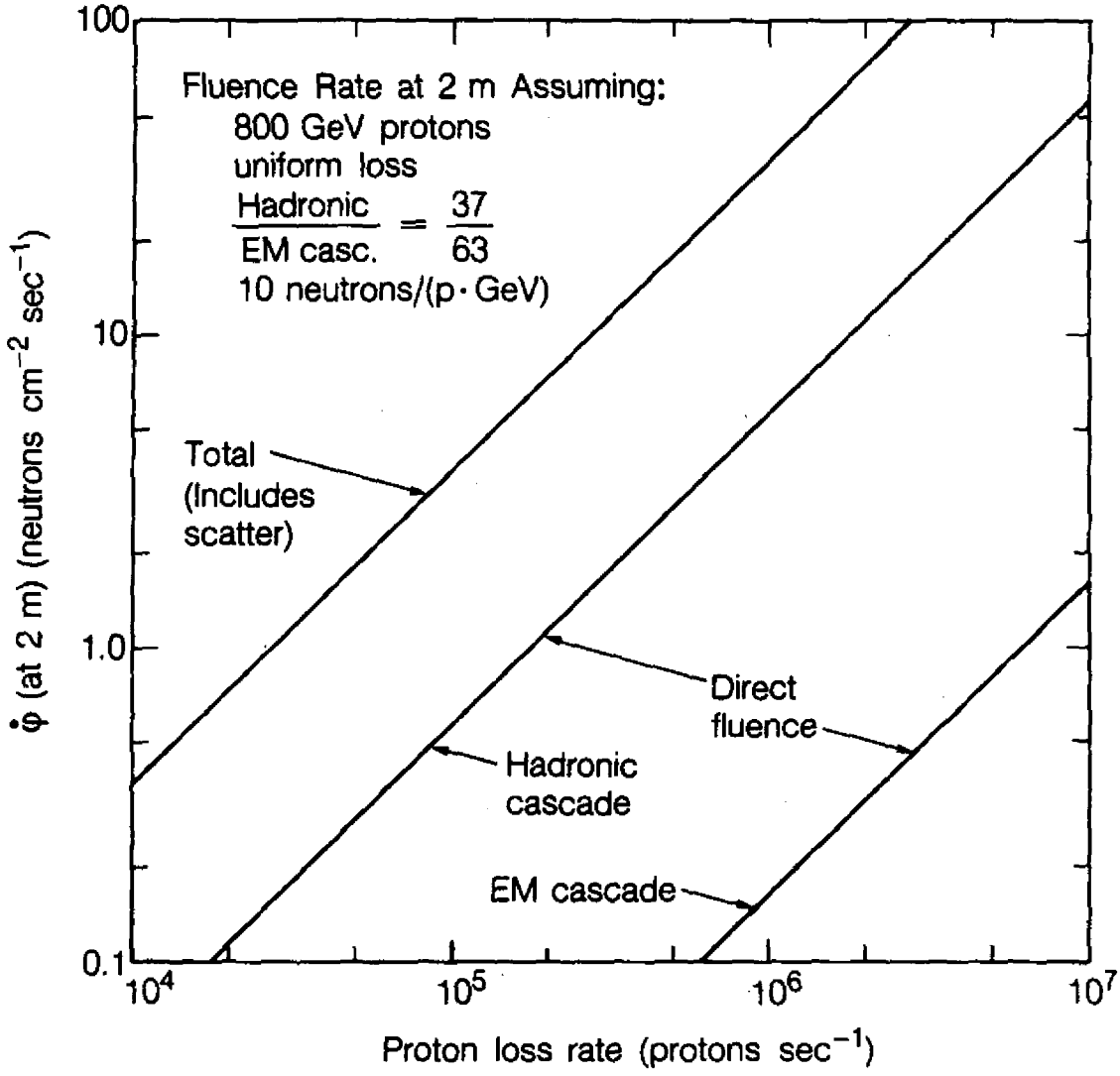

XBL 868-12017

Fig. 14. Estimate of fluence rate at 2 m for a uniform loss of 800 GeV protons around ring circumference (2π 1000 m). Assumed division of energy: [EM cascade : Hadronic cascade] = 63% : 37%. Lower line: Estimate of direct fluence rate of photoneutrons; Center line: Direct fluence rate from the hadronic cascade; Upper line: total fluence rate including scattered.

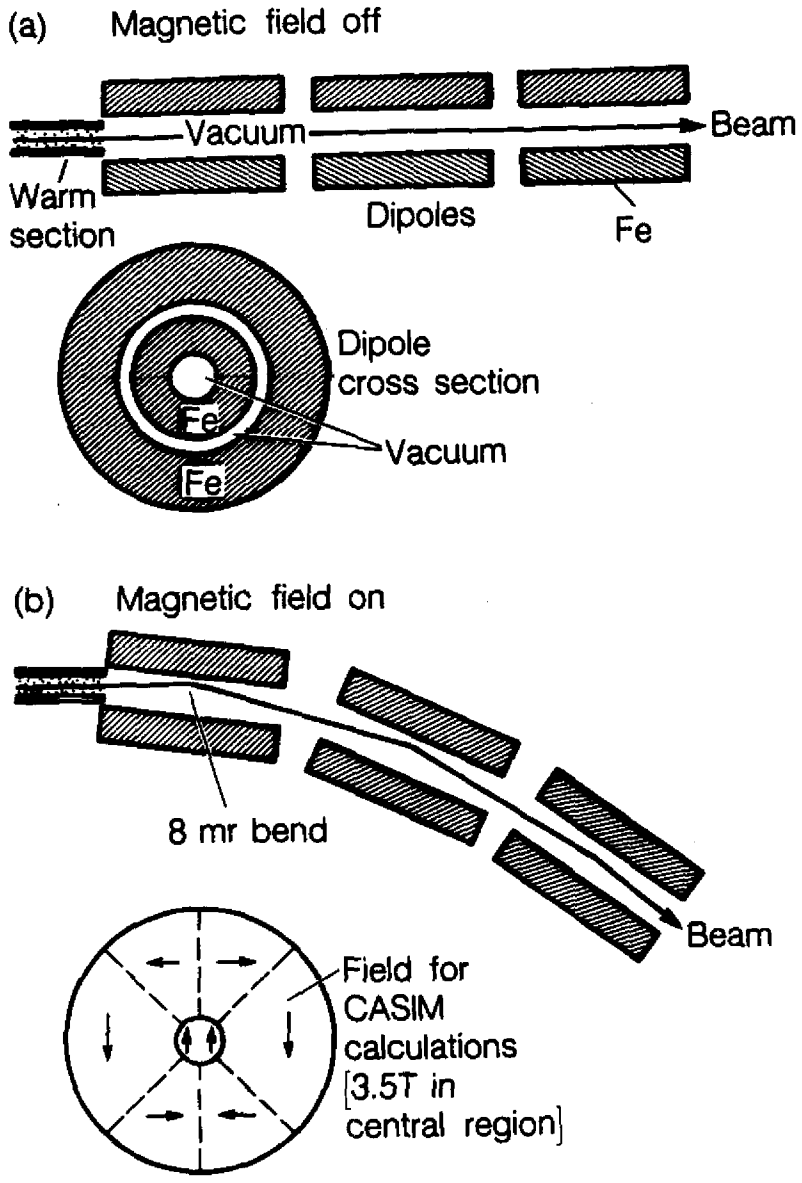

XBL 868-12019

Fig. 15. Geometry used for CASIM simulation of experimental arrangement (not to scale and transverse dimensions exaggerated). (a) Magnetic field off, showing dipole cross section assumed; (b) Magnetic field on, showing idealized field distribution. Field is assumed uniform within each of 7 regions. Orbit is bent by 8 mradian in each dipole.

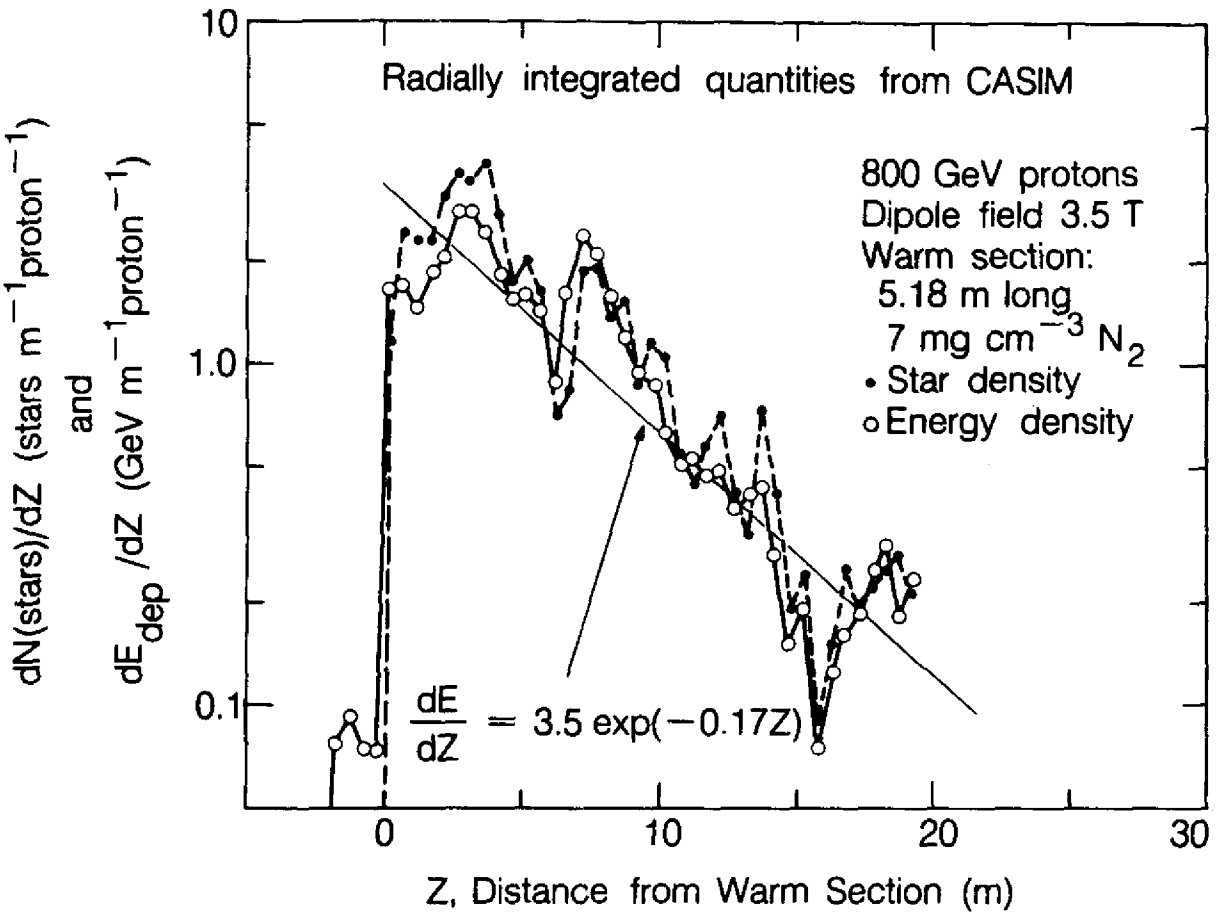

XBL 869-12025

Fig. 16. CASIM Monte-Carlo calculations for radially-integrated star density, $dN\,(\text{stars})/dz$ and energy deposited, dE_{dep}/dz, in dipole magnets as functions of distance from the warm section. Straight line is a parameterization of the energy deposited, dE_{dep}/dz.

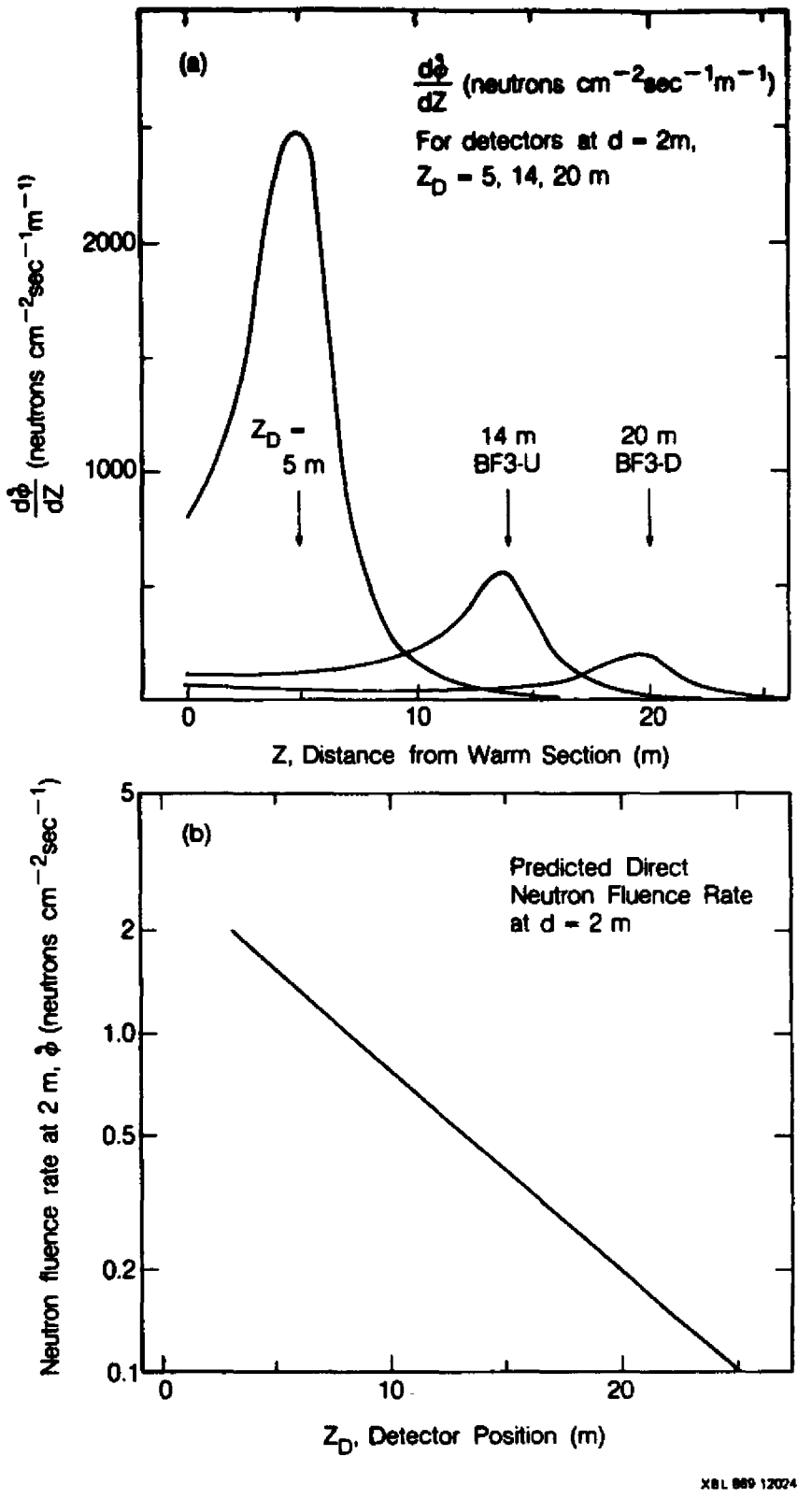

Fig. 17. (a) Calculations based on parameterization of previous figure showing direct-fluence source distribution along dipole chain, $d\dot{\phi}/dz$, at detector locations (d = 2m; and z_D = 5, 14 and 20m). Abscissa is the distance, z, from the warm section. Integral of curve for each detector location, z_D, gives:

(b) Neutron direct fluence rate, $\dot{\phi}$ at d = 2m as a function of z_D, based on integrals of panel (a).

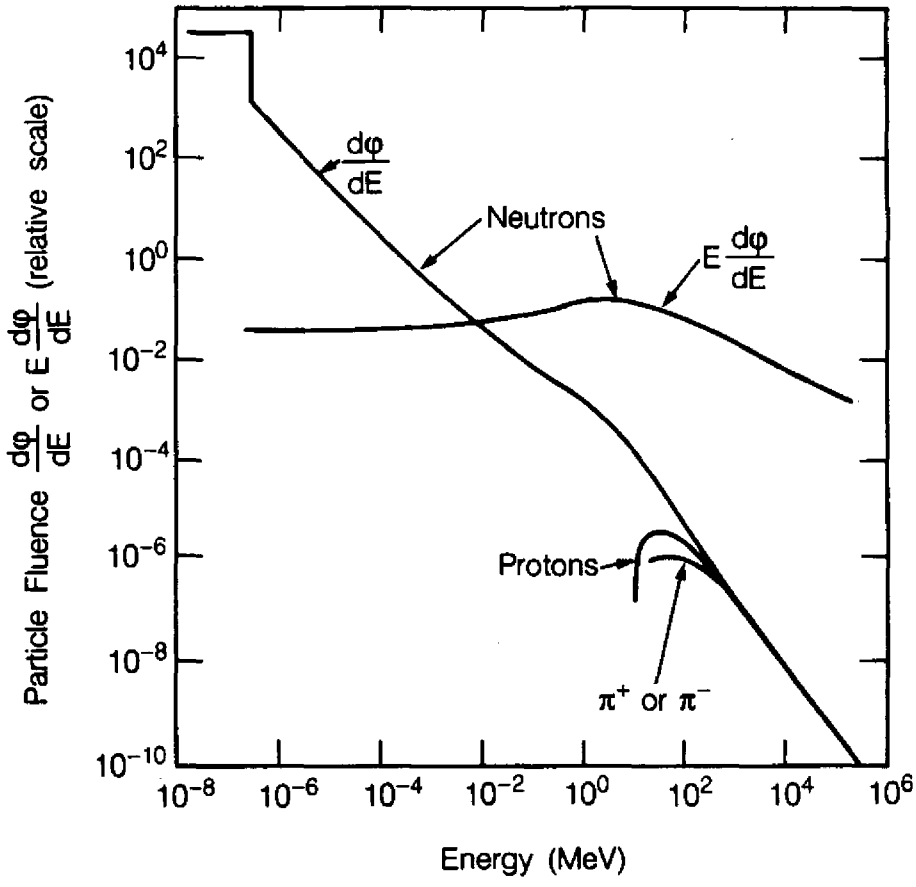

XBL 868-12020

Fig. 18. Hadron spectra within earth at end of a concrete-lined target tunnel. Incident proton energy: 500 GeV. [Adapted from Monte Carlo calculation of Gabriel and Santoro (Gab71)].

APPENDICES TO "MEASUREMENT OF NEUTRON SPECTRA AND DOSES IN THE TEVATRON TUNNEL FOR 800 GeV CIRCULATING PROTON BEAMS"*

William P. Swanson

Lawrence Berkeley Laboratory
University of California
Berkeley, CA 94720

ABSTRACT

Seven appendices (A - G) are compiled which discuss dosimetric aspects of neutron spectral measurements made in the Tevatron tunnel as reported by McCaslin et al. in SSC-CDG Report No. 58.* These appendices:

A. Estimate the beam lifetime and interaction rates in warm and cold sections. Depending on the assumptions adopted regarding gas pressure in the beam tube, beam lifetimes (1/e) lie between 383 - 518 hours, assuming nuclear interactions are the sole cause of beam loss. For 1×10^{11} stored protons, and depending on assumptions, the number of primary interactions in the warm section A-48 is 360 or 486 sec^{-1}, and the number of primary interactions in the following 20-m cold section is 113 or 0.3 sec^{-1}. Better information on the pressure in the beam tube is needed.

B. Estimate the contribution of photoneutrons and relate it to an estimate of direct neutron production from the hadronic cascade. The estimate shows that the photoneutrons are less than the direct neutrons by about a factor of 37.

C. Estimate the proportions of fluences [direct neutrons : scattered thermal neutrons : scattered fast neutrons] $= [\phi_{dir} : \phi_{sc}^{th} : \phi_{sc}^{fast}] = [15\% : 16\% : 69\%]$.

D. Summarize published information on gamma tissue kerma values, K_γ, in neutron fields. Typical ratios are: $K_\gamma/K_n \approx 0.14$, and $K_\gamma^{max}/\phi_n \approx (4\text{–}5)\times10^{-10}$ rad cm^2 and $K_\gamma/\phi_n \approx 2.6\times10^{-10}$ rad cm^2, depending on the source quoted.

E. Estimate the direct dose from the electromagnetic cascade, relative to the direct neutron fluence, to be about $D_{EM}/\phi_{dir} = 2.4\times10^{-10}$ rad $neutron^{-1}$ cm^2.

F. Estimate an experimental upper limit to doses from the electromagnetic cascade, relative to the neutron dose (to tissue) to be about $D_{EM}(LiI)/D_n(tissue) < 1.2$.

G. Derive the shape of the pulse height spectrum expected for minimum ionizing particles in LiI crystals and show how an upper limit on dose due to minimum ionizing particles can be determined from the pulse height distribution.

---

*Joseph B. McCaslin, Rai-Ko S. Sun, William P. Swanson, Alexander J. Elwyn, William S. Freeman and Peder M. Yurista, Measurement of Neutron Spectra and Doses in the Tevatron Tunnel for 800 GeV Circulating Proton Beams, Lawrence Berkeley Laboratory and Fermi National Accelerator Laboratory, SSC-CDG Report SCC-58 (1986).

October 2, 1986

APPENDICES TO "MEASUREMENT OF NEUTRON SPECTRA AND DOSES IN THE TEVATRON TUNNEL FOR 800 GeV CIRCULATING PROTON BEAMS"*

William P. Swanson

Lawrence Berkeley Laboratory
University of California
Berkeley, CA 94720

APPENDIX A. BEAM-GAS INTERACTIONS IN THE TEVATRON, BEAM LIFETIME AND THE SOURCE OF TUNNEL NEUTRONS

I. ESTIMATES BASED ON PUBLISHED INFORMATION

1. Beam-Gas Interactions in Warm and Cold Sections

The Tevatron has a circumference of $2\pi 1000$ m, of which we are able to sample only a small portion. Approximately 93% of the circumference is enveloped by cryogenic magnets which make the cold vacuum vessel an efficient pump. The remaining 7% comprise 30 straight sections at room temperature. Pressures within the warm and cryogenic sections are nominally 5×10^{-11} and 1×10^{-8} torr, respectively (Edw85; see Section 4 for alternate parameters). Rather than air, this residuum consists of gases evolved from the metal surfaces. In the warm sections we assume this mixture to contain $H_2 : CO = 0.35 : 0.65$, giving an average cross section per molecule of 533 mb. For the cold sections we assume a mixture of $H_2 : He = 0.65 : 0.35$, giving an average cross section per molecule of 102 mb. The proton-nucleus cross sections (Table A-1) on which these figures are based are taken from values recommended by Rubinstein as quoted by Mizuno et al. [Rub79, Miz79]:

Table A-1. Proton-nucleus cross sections assumed.

Nucleus	H	He	C	N	O
Atomic number	1	4	12	14	16
Cross section (mb)	42	135	335	390	440

These values reflect a dependence on A intermediate between A and $A^{2/3}$.

The average cross sections quoted above are derived as shown in Table A-2.

Table A-2. Average cross sections for gas mixtures (per molecule).

	Warm Section	Cold Section
Mixture	$H_2 : CO = 0.35 : 0.65$	$H_2 : He = 0.65 : 0.35$
Calculation	$0.35\times(2\times42)+0.65\times(335+440)$	$0.65\times(2\times42)+0.35\times(135)$
Result, $\overline{\sigma}$	533 mb	102 mb

The average cross section is particularly sensitive to the fraction of the mix which is H_2, $F(H_2)$. If the proportion of H_2 in these mixtures is changed by, say $\Delta F = \pm 0.2$, the $\overline{\sigma}$ will shift by a corresponding amount (about 25% and 20% for warm and cold sections, respectively). The response of the vacuum gauges would also be affected by a change in the proportions, and in a direction which would reinforce the error if it were not accounted for. In this discussion we

assume that *all pressures have already been properly corrected for gauge response for whatever gas mixtures are herein assumed.*

It is instructive to compare the ratios of rate of loss within the two temperature domains. The warm sections contain higher pressures of gasses having higher average cross sections but the cold sections have a higher density of molecules than they would at room temperature, owing to the lower temperature (4.6 *vs* 300 K). Using the ideal gas law, the ratio of number of interactions per unit length is:

$$\frac{dN_{warm}/dL}{dN_{cold}/dL} = \left[\frac{533\text{mb}}{102\text{mb}}\right] \times \left[\frac{1\times10^{-8}\text{torr}}{5\times10^{-11}\text{torr}}\right] \times \left[\frac{4.6\text{K}}{300\text{K}}\right] = 16.0\ . \qquad \text{(A-1)}$$

Although the number of interactions per unit length is larger for warm sections, the assumptions made here (mainly the pressure) would predict a larger fluence at our location from primary interactions in the *cold* section because of its close proximity. When the above ratio is multiplied by the ratio of lengths ($\Sigma L_{warm}/C = 0.07$) / ($\Sigma L_{cold}/C = 0.93$), where C is the Tevatron circumference, we have

$$\frac{N_{warm}}{N_{cold}} = 16.0 \times \left[\frac{0.07}{0.93}\right] = 1.2\ . \qquad \text{(A-2)}$$

Thus, averaged around the entire circumference, ***the integrated losses due to nuclear interactions in the warm and cold sections are approximately equal if the pressures assumed (Edw85) are realistic.*** See discussion of Section 4.

2. Beam Lifetime Due to Nuclear Interactions

To estimate the decay constant, λ, of the beam current, I, based on beam-gas nuclear interactions (as distinct from Coulomb scattering), we use the relationship

$$-\lambda = \frac{1}{I}\frac{dI}{dt} = \bar{\sigma}\,\bar{\rho}\,c \qquad \text{(A-3)}$$

where $\bar{\sigma}$ is the average cross section per molecule, and $\bar{\rho}$ is the density of molecules, given by $[N_A\ /\ 22.4\times10^3\ \text{cm}^3]\times[P\ (\text{torr})\ /\ 760\ \text{torr}] = 3.54\times10^{16} \times [\text{P (torr)}]$ molecules cm^{-3} at room temperature (300 K). This is based on Avogadro's number $N_A = 6.022\times10^{23}$ and the molar volume for a gas at STP. For cold sections the same method of estimating $\bar{\rho}$ applies, except that it is also scaled by the inverse ratio of temperatures (300 K / 4.6 K). The speed of beam particles through this rarified target is $c = 3\times10^{10}$ cm sec^{-1}.

In order to facilitate calculation, the given and derived parameters for the warm and cold sections are tabulated separately in Table A-3. Combining the decay constants, we have

$$\lambda_{tot} = \lambda_w + \lambda_c = 3.96\times10^{-7}\ \text{sec}^{-1} + 3.29\times10^{-7}\ \text{sec}^{-1} = 7.25\times10^{-7}\ \text{sec}^{-1} \qquad \text{(A-4)}$$

$$= 2.61\times10^{-3}\ \text{hr}^{-1}.$$

$$t_{1/e} = 1/\lambda_{tot} = 383\ \text{hr}\ . \qquad \text{(A-5)}$$

These results may be compared to the statements of Edwards [Edw85, p. 626] that imply a *luminosity* lifetime of $t_{1/e}$ =76.5 hr and estimate that "The warm region gas contributes about one-half of this reduction." The effect of Coulomb scattering is included in Edward's estimate, which applies to the reduction in luminosity, rather than current. This probably accounts for the lifetime shorter than calculated here. There are other effects which tend to shorten the lifetime that are not related to residual gas. These are "phase space dilution" and/or "diffusion out of the bucket" caused by intra-bucket particle scattering. Therefore the above analysis, if accurate, gives only an upper limit to the beam lifetime.

During the runs of September/October, 1985, the best lifetimes measured were $t_{1/e} \approx 70$ hr for 800 GeV low-beta operation.* For 150 GeV Tevatron operation, the lifetime was much shorter: $t_{1/e} \approx 6$ hr (Edw86).

* However, it was rumored that 70 hours is the longest lifetime that *can be measured;* the real lifetime might be longer than this.

Table A-3. Calculation of beam decay constant from nuclear interactions.

Quantity	Warm Section	Cold Section
Given quantities		
$F(H_2)$	0.35	0.65
F(CO)	0.65	—
F(He)	—	0.35
T(K)	300	4.6
Pressure, P (torr)	1×10^{-8}	5×10^{-11}
$\Sigma L\ /\ C$	0.07	0.93
Derived quantities		
$\overline{\sigma}$ (mb)	533	102
$\overline{\rho}$ (molecules cm^{-3})	3.54×10^{8}	1.16×10^{8}
λ (sec^{-1})	3.96×10^{-7} sec^{-1}	3.29×10^{-7} sec^{-1}

3. Interaction Rate in the Warm Straight Section, A-48.

The time rate of interactions, $\dot{N}_{int}$, in a section of length, L, is given by the product

$$\dot{N}_{int} = \overline{\sigma}\,\overline{\rho}\,L\ \dot{N}_p\,, \tag{A-6}$$

where $\overline{\sigma}$ is the average cross section per gas molecule, $\overline{\rho}$ is the average number of molecules per unit volume and L = 400 cm.** These quantities are given in the section just above. Assuming the ring is filled with 1×10^{11} protons, the rate of arrival of protons at a point is

$$\dot{N}_p = 1\times10^{11}\ \text{protons}\cdot c\ /C = 4.775\times10^{15}\ \text{protons sec}^{-1}, \tag{A-7}$$

where c is the speed of light and C = $2\pi1000$ m is the ring circumference.

For a pressure of 1×10^{-8} torr at the center of a warm section bounded by cold sections, the average density of molecules is given by

$$\overline{\rho} = \left[\frac{N_A}{22.4\times10^{3}\ \text{cm}^3}\right]\times\left[\frac{1\times10^{-8}\ \text{torr}}{760\ \text{torr}}\right] = 3.54\times10^{8}\ \text{molecules cm}^{-3}, \tag{A-8}$$

based on Avogadro's number and the molar volume of a gas at STP. [A factor of 2/3 which reflects the average in a parabolic pressure distribution which is maximum at the center and zero at each end is neglected here.]

Combining factors, we have

$$\dot{N}_{int} = \overline{\sigma}\,\overline{\rho}\,L\ \dot{N}_p = [533\times10^{-27}\ \text{cm}^2]\times[3.54\times10^{8}\ \text{cm}^{-3}]\times[400\ \text{cm}]\ \dot{N}_p \tag{A-9}$$
$$= 360\ \text{interactions sec}^{-1}$$

in the 4-m warm straight section A-48, for 1×10^{11} stored protons. For comparison, the number in the 20-m cold section just downstream from A-48 is

$$\frac{1}{16}\times\frac{20\ \text{m}}{4\ \text{m}}\times 360\ \text{sec}^{-1} = 113\ \text{interactions sec}^{-1}\,, \tag{A-10}$$

where the respective factors reflect the relative interaction rate per unit length [Eq. (A-1)] and account for the relative length. From this simple comparison, it is not obvious whether the warm or the cold section is the dominant source of primary interactions producing the ambient radiation field at the location of our detectors.

** We were informed by H. T. Edwards that the actual length of warm section at A-48 is 160 inches, or 4.06 m (Edw86).

II. ESTIMATES BASED ON REVISED INFORMATION OF H. JOSTLEIN

4. Estimates Based on Alternate Parameters

The above discussion, based on written sources (Edw85, Miz79), would indicate a maximum beam lifetime ($1/e$) of about 383 hours with the (warm, cold) sections contributing to the loss rate in approximately equal amounts. That is, $(\lambda_w : \lambda_c) = (1.2 : 1.0)$ from Eq. (A-2).

In private communications with H. Jostlein, we were apprised of the large uncertainties in the actual pressures. For the warm sections, we were quoted "$(1 - 4)\times10^{-8}$ torr" and for the cold sections, "less than 1×10^{-13} torr; assume it to be zero." As for gas composition in the warm sections, "$F(H_2)$ is in the range 50 - 70%; the remainder is mostly CO with some CH_4." For the cold sections, "assume it is all He (with some H_2 but this is extremely small)."

Repeating the calculations described in Sections 1-3 with parameters consistent with Jostlein's statements, gives the results shown in Table A-4.

Table A-4. Calculation of beam decay constant from nuclear interactions.

Quantity	Warm Section	Cold Section
Given quantities		
$F(H_2)$	0.60	—
F(CO)	0.40	—
F(He)	—	1.00
T(K)	300	4.6
Pressure, P (torr)	2×10^{-8}	1×10^{-13}
$\Sigma L\ /\ C$	0.07	0.93
Derived quantities		
$\overline{\sigma}$ (mb)	360	135
$\overline{\rho}$ (molecules cm^{-3})	7.07×10^{8}	2.31×10^{5}
λ (sec^{-1})	5.35×10^{-7} sec^{-1}	8.69×10^{-10} sec^{-1}

$$\frac{dN_{warm}/dL}{dN_{cold}/dL} = \left[\frac{360\text{mb}}{135\text{mb}}\right] \times \left[\frac{2\times10^{-8}\text{torr}}{1\times10^{-13}\text{torr}}\right] \times \left[\frac{4.6\text{K}}{300\text{K}}\right] = 8180\ , \qquad \text{(A-1a)}$$

and the revised ratio of number of interactions around the entire circumference, N_{warm}/N_{cold}, previously 1.2, is now 616! If the revised estimate is correct, it is probable that the warm section, A-48, is the main source of primary beam interactions in our region. This would simplify our picture of the neutron source considerably.

Combining the decay constants from Table A-4, we now have

$$\lambda_{tot} = \lambda_w + \lambda_c = 5.35\times10^{-7}\ \text{sec}^{-1} + 0.00869\times10^{-7}\ \text{sec}^{-1} = 5.36\times10^{-7}\ \text{sec}^{-1} \qquad \text{(A-4a)}$$
$$= 1.93\times10^{-3}\ \text{hr}^{-1}.$$

This gives a decay time, $t_{1/e}$, of:

$$t_{1/e} = 1/\lambda_{tot} = 518\ \text{hr}\ . \qquad \text{(A-5a)}$$

The approximate doubling of the lifetime is mainly due to absence of interactions in the cold sections. See the last part of Section 2 regarding other factors affecting the beam lifetime.

A revised estimate of the interaction rate in A-48 gives:

$$\dot{N}_{int} = \overline{\sigma}\,\overline{\rho}\,L\ \dot{N}_p = [360\times10^{-27}\ \text{cm}^2]\times[7.07\times10^{8}\ \text{cm}^{-3}]\times[400\ \text{cm}]\ \dot{N}_p \qquad \text{(A-9a)}$$
$$= 486\ \text{interactions sec}^{-1}$$

where $\dot{N}_p = 4.775 \times 10^{15}$ protons sec^{-1} for 1×10^{11} protons stored. This is about 35% more than the rate (360 interactions sec^{-1}) calculated in Eq. 9. The number of interactions in the 20-m cold section is now estimated as only about 0.3 interactions sec^{-1}, a negligible amount.

5. Discussion

It is essential to know the pressure in both A-48 and the cold dipole chain more accurately. From Jostlein's information, it seems that A-48 is the probable source of primary interactions, with about 486 interactions sec^{-1}, but the information supplied by Jostlein leaves room for an uncertainty of at least a factor of two in these estimates, from uncertainty in the A-48 pressure alone. The estimates regarding A-48 are not significantly different (360 or 486 interactions sec^{-1}) for the two sets of information examined. The major difference is in the contribution of the cold section. From Jostlein's information, it appears that primary interactions in the adjacent cold section can be ignored, whereas the published information would indicate a major contribution to the fluence at our location.

Remaining questions include: Are there nearby warm sections upstream of A-48 that can contribute to the measured fluence? Are there possible neutron sources downstream of the three dipoles after A-48?

REFERENCES

Edw85 H. T. Edwards, The Tevatron Energy Doubler, Ann. Rev. Nucl. Part. Sci. 35, 605 (Annual Reviews Inc., Palo Alto, CA, 1985).

Edw86 H. T. Edwards, Private communication, Fermi National Accelerator Laboratory (1986).

Jos85 H. Jostlein, Private communication, Fermi National Accelerator Laboratory, Batavia, IL, (1985).

Miz79 H. Mizuno, S. Ohnuma and A. G. Ruggiero, Vacuum and beam lifetime in the Doubler, Fermi National Accelerator Laboratory, Batavia, IL, Unpublished Note UPC No. 119 (Dec. 21, 1979).

Rub79 R. Rubinstein, Fermi National Accelerator Laboratory, Batavia, IL, Private communication as quoted by Miz79 (1979).

APPENDIX B. ESTIMATES OF PHOTONEUTRON AND HADRONEUTRON FLUENCE PRODUCED BY 800-GeV PROTON BEAMS

At Tevatron energies a large fraction of the initial energy of an hadronic cascade (HC) is fed into the electromagnetic (EM) cascade via π^0 decay into photons (Ran85, Ste85; See Fig. B-1). This immediately suggests that some fraction of the neutron fluence observed in the Tevatron tunnel is actually due to photoneutrons.

The photoneutron fluence is calculated under the following assumptions:

- Beam intensity is 1×10^{11} protons at 800 GeV;
- Entire beam is lost uniformly around the circumference of 2 π 1000 m;
- 63% of beam particle energy devolves to the EM cascade;
- The yield of photoneutrons is 1.0×10^{9} neutrons per J of EM energy deposited in iron (Swa79);
- Beam-line to detector distance is $d = 2$ m.

The total energy in a beam of 1×10^{11} protons at 800 GeV is

$$(1\times10^{11}) \times (1.602\times10^{-19}\mathrm{C}) \times (800\times10^{9}\mathrm{V}) = 1.28\times10^{4}\ \mathrm{J}. \tag{B-1}$$

This gives the total yield of photoneutrons if this energy is deposited in iron:

$$Y(\text{photoneutrons}) = 0.63 \times 1.28 \times 10^{4}\mathrm{J} \times (1\times10^{9}\ \text{neutrons}\cdot\mathrm{J}^{-1}) \tag{B-2}$$
$$= 0.806\times10^{13}\ \text{neutrons}.$$

Distribute the neutrons uniformly over a circumference of 2 π 1000 m:

$$q' = 0.806\times10^{13}\ \text{neutrons}/\ (2\pi1000\mathrm{m}) = 1.28\times10^{9}\ \text{neutrons}\cdot\mathrm{m}^{-1}. \tag{B-3a}$$

For an isotropic line source the fluence at distance, d =2m, is:

$$\phi_{\gamma,n} = \frac{q'}{4d} = \frac{1.28\times10^{9}\ \text{neutrons}\cdot\mathrm{m}^{-1}}{4\times2\mathrm{m}} = 1.60\times10^{8}\ \text{neutrons}\cdot\mathrm{m}^{-2} \tag{B-4a}$$
$$= 1.60\times10^{4}\ \text{neutrons}\cdot\mathrm{cm}^{-2}$$

per 1×10^{11} protons uniformly lost at 800 GeV. Room scattered neutrons (a larger number) are not included and fluence attenuation in the iron is not considered. This estimate should be good to within a factor of two.

We may also calculate the neutron fluence of direct hadronic origin under the same assumptions except that we use the rule of thumb for neutron production by proton beams (Pat73):

- Neutron production by protons incident on a thick iron absorber: 10 neutrons·proton^{-1}·GeV^{-1}

This gives the total yield of hadroneutrons at distance, d =2m:

$$Y(\text{hadroneutrons}) = 0.37 \times (1\times10^{11}\ \text{protons}) \times (800\mathrm{GeV}) \tag{B-5}$$
$$\times\ (10\ \text{neutrons}\cdot\text{proton}^{-1}\cdot\mathrm{GeV}^{-1}) = 29.6\times10^{13}\ \text{neutrons}.$$

Dividing by 2 π 1000 m gives a linear source of

$$q' = 29.6\times10^{13}\ \text{neutrons}/(2\pi1000\mathrm{m}) = 47.1\times10^{9}\ \text{neutrons}\cdot\mathrm{m}^{-1}. \tag{B-3b}$$

An isotropic line source gives the fluence of *hadroneutrons* at the distance d =2m:

$$\phi_{h,n} = \frac{q'}{4d} = \frac{47.1\times10^{9}\ \text{neutrons}\cdot\mathrm{m}^{-1}}{4\times2\mathrm{m}} = 5.89\times10^{9}\ \text{neutrons}\cdot\mathrm{m}^{-2} \tag{B-4b}$$
$$= 58.9\times10^{4}\ \text{neutrons}\cdot\mathrm{cm}^{-2}.$$

The ratio of the above two fluences is

$$\frac{\phi_{h,n}}{\phi_{\gamma,n}} = \frac{58.9\times10^4 \text{ neutrons}\cdot\text{cm}^{-2}}{1.60\times10^4 \text{ neutrons}\cdot\text{cm}^{-2}} = 36.8 \ , \tag{B-6}$$

which at least shows that neutrons direct from the hadronic cascade, rather than photoneutrons, are the dominant source. This ratio should be approximately independent of distance from the beam line.

The sum of the above two direct fluences at d =2m is

$$\phi_{\gamma,n} + \phi_{h,n} = [1.60\times10^4 + 58.9\times10^4] \text{ neutrons}\cdot\text{cm}^{-2} \tag{B-7}$$

$$\phi_{tot,dir} = 60.5\times10^4 \text{ neutrons}\cdot\text{cm}^{-2} \ .$$

Assuming a beam decay time ($1/\epsilon$) of, for example, 100 hours (3.6×10^5 sec), the direct neutron fluence rate would be [60.5×10^4 neutrons cm^{-2} / 3.6×10^5 sec] =

$$\dot{\phi}_{dir} = 1.7 \text{ neutrons cm}^{-2} \text{ sec}^{-1}$$

REFERENCES

Pat73 H. W. Patterson and R. H. Thomas, Accelerator Health Physics, (Academic Press, New York, 1973, p. 141).

Ran85 J. Ranft, Private communication, Karl Marx University, Leipzig (1985).

Ste85 G. R. Stevenson, Private communication, CERN, Geneva (1985).

Swa79 W. P. Swanson, Improved calculation of photoneutron yields released by incident electrons, Health Physics 37, 347 (1979).

FIGURE CAPTION

Fig. B-1. Fraction of primary energy transferred to the EM cascade as a function of primary energy. Circles show calculation of Ranft (Ran85); points are interpolations.

APPENDIX C. FLUENCE OF SCATTERED NEUTRONS IN THE TUNNEL

The fluence of scattered neutrons inside a cubical concrete room is rather uniform and is proportional to the fast-neutron source strength, Q, divided by the area of the room, A (floor, ceiling and walls combined). For thermal neutrons, the relation is (Pat58):

$$\phi_{sc}\,(thermal) = k^{th}\,Q\,/A \;= 1.26\,Q\,/A \tag{C-1}$$

and for fast neutrons it is (McC79, Eis82):

$$\phi_{sc}\,(fast) = k^{fast}\,Q\,/A \;= 5.4\,Q\,/A. \tag{C-2}$$

[The experimental and theoretical coefficients for thermal scattered neutrons are $k^{th} = 1.26 \pm 0.1$ and 1.39, respectively. We choose the experimental value for use here.]

We approximate a cubical concrete room by a concrete tunnel of circular cross section πR^2, and length L. Later we let L approach infinity. This leads to limits in the amount of direct, scattered-thermal and scattered-fast neutron fluences, so that ratios can be taken. The source strength in this tunnel section is $Q = q' \times L$, where q' is the number of neutrons per length of source. For an infinite line source ($L \rightarrow \infty$) the fluence of direct neutrons at distance, d, is:

$$\phi_{dir} = q'\,/\,4d \tag{C-3}$$

For scattered neutrons the fluence is

$$\phi_{sc} = k\frac{Q}{A} = \frac{q'\,L}{A_{walls} + A_{ends}}, \tag{C-4}$$

where

$$A_{walls} = 2\pi RL\,, \text{ and} \tag{C-5a}$$

$$A_{ends} = 2\pi R^2. \tag{C-5b}$$

This gives

$$\phi_{sc} = k\frac{q'\,L}{2\pi[R^2 + RL]} \tag{C-6}$$

For $L >> R$, this gives

$$\phi_{sc} = \frac{k\;q'}{2\pi R}. \tag{C-7}$$

Taking ratios, we have

$$\phi_{dir} \;:\; \phi_{sc}^{\,thermal} \;:\; \phi_{sc}^{\,fast} = \frac{q'}{4d} \;:\; \frac{k^{th}\,q'}{2\pi R} \;:\; \frac{k^{fast}\,q'}{2\pi R}. \tag{C-8}$$

Using $d = 2$ m and R = 1.52 m, we have:

$$\frac{q'}{8} \;:\; \frac{1.26\,q'}{2\pi 1.52} \;:\; \frac{5.4\,q'}{2\pi 1.52} \tag{C-9}$$

$$= 15\% \;:\; 16\% \;:\; 69\%\,.$$

There may be uncertainties in this relation arising from the geometric approximation made and from vagueness about the term "fast" neutron. However, it is adequate to show that the vast majority ($\approx$85%) of neutrons detected in our tunnel geometry are *scattered* neutrons.

REFERENCES

Eis82 C. M. Eisenhauer, R. B. Schwartz and T. Johnson, Measurement of neutrons reflected from the surface of a calibration room, Health Physics 42, 489 (1982).

McC79 R. C. McCall, T. M. Jenkins and R. A. Shore, Transport of accelerator produced neutrons in a concrete room, IEEE Trans. Nucl. Sci. NS-26, 1593 (1979).

Pat58 H. W. Patterson and R. Wallace, A Method of Calibrating Slow-Neutron Detectors, Report No. UCRL-8359, Lawrence Radiation Laboratory, Berkeley, CA 94720 (1958).

APPENDIX D. PUBLISHED RATIO OF GAMMA TISSUE KERMA TO NEUTRON TISSUE KERMA AND RATIO OF GAMMA TISSUE KERMA TO NEUTRON FLUENCE

In the review article by Tochilin and Shumway (Toc69), the measured ratio of kermas for tissue, K_γ/K_n, is tabulated for typical fast-neutron irradiation facilities. These facilities include nuclear-weapon fission, critical assemblies, reactors and converter plates. The primary spectrum from such facilities is a fission spectrum which is not too different from the evaporation spectrum believed to be a prominent source for the FNAL Tevatron tunnel measurements.

Among 36 tabulations of the tissue kerma ratio for various geometries and filtering conditions, values of K_γ/K_n varied between 0.09 and 8.4. However all but 5 values lay between 0.09 and 1.00, with the median being 0.40. The high outlying values were for particular arrangements not resembling our tunnel geometry.

Taking three experiments that most closely resembled ours, i.e., a source (reactor) and detector contained in a concrete room and a source-to-detector distance comparable to 2 m, we find values close to the lower range tabulated by Tochilin and Shumway (Table D-1).

Table D-1. Published tissue kerma data for concrete rooms.

Reference	Room volume (m^3)	Detector distance (m)	Neutron tissue kerma factor ($rad \cdot cm^2$)	K_γ/K_n
Say60	580	0.50	2.36×10^{-9}	0.091
		1.00	2.26×10^{-9}	0.090
		1.50	2.22×10^{-9}	0.117
Mob64	520	1.50	—	0.16
Hum65	1400	1.50	—	0.14
Average (for 1.50 m)		1.50	2.22×10^{-9}	0.14

For these experiments the ratio K_γ/K_n for tissue (Col. 5) varied slowly with increasing distance from the source; there was an average of only 26% increase as the distance was varied from 0.50 to 1.50 m. The small increase reported in Say60 is probably due to a reduction of direct neutrons with distance, in relation to capture gammas from the concrete walls.

A comparison of the three experiments suggests that K_γ/K_n does not vary too much with room volume. This may be because, as the wall-to-detector distance increases (holding the neutron fluence constant), the $1/r^2$ decrease in gamma kerma from each element of source area is cancelled by the increased total area of the walls.

The neutron tissue kerma factors shown in the table (Col. 4, from Say60) are quite close to the values found in the Tevatron tunnel measurements, about 2.0×10^{-9}rad·cm^2, again suggesting the similarity of the two situations as regards neutron spectra. Therefore we feel that these published results may be considered as estimates of the corresponding ratios for our measurement conditions in the Tevatron tunnel. In fact, it may be that almost all of the photon dose at our detector location may be neutron-related. This would mean that the photon dose direct from the accelerator in the Tevatron experiment is quite small.

From data in NCRP-38 (NCRP71), it is also observed that, for broad unidirectional fields of monoenergetic neutrons incident on a tissue phantom, the ratio of *maximum* photon dose within

the phantom to *incident* neutron fluence lies within a surprisingly narrow range, $(4.0\text{–}5.3)\times10^{-10}$ rad cm^2 for neutron energies from thermal to 5 MeV. This near-constancy can be understood by considering that the majority of neutrons not reflected eventually become thermalized to produce the observed photon dose, mainly by gammas from capture on hydrogen. To the extent that concrete (also hydrogeneous) is similar to tissue, a similar relation should hold. It is likely that a large fraction of our photon dose (quoted as an *upper limit* of about 2×10^{-9} rad cm^2 for both the Tevatron and Main Ring) is accounted for by this effect.

Sayeg (Say60) also specifies the fluence of fast neutrons obtained in his experiment. This permits a determination of the ratio of gamma tissue kerma to fast neutron fluence. This value is

$$\frac{K_\gamma}{\phi_n} = 2.60\times10^{-10}\frac{\text{rad}}{\text{neutrons}\cdot\text{cm}^{-2}},$$

at the distance of 1.5 m. This can be compared to the upper limit found in the Tevatron experiment of about 2×10^{-9} rad cm^2.

REFERENCES

Hum65 K. C. Humpherys, W. Quam, C. Rainbolt, R. Durkee and T. Dahlstrom, Nuclear Radiation Dosimetry Measurements of the White Sands Missile Range Fast Burst Reactor, Report No. S-262-R, EG&G Inc., Santa Barbara, CA (1965).

Mob64 T. S. Mobley, R. E. Engel, R. E. Godden and V. T. Penikas, "In vivo and air dosimetry of fission-spectrum neutrons" in Biological Effects of Neutron and Proton Irradiations, Vol. I, p. 103 (Vienna: IAEA, 1964).

NCRP71 National Council on Radiation Protection and Measurements, Protection Against Neutron Radiation, Report No. 38 (Washington, D. C., 1971).

Say60 J. A. Sayeg, Neutron and γ Dosimetry Measurements at the AFRRI-DASA TRIGA Reactor, Armed Forces Radiobiol. Res. Inst. Report AFRRI CR65-6, Bethesda, MD (1965).

Toc69 E. Tochilin and B. W. Shumway, "Dosimetry of neutrons and mixed n + γ fields" in F. H. Attix and E. Tochilin, eds., Radiation Dosimetry, Vol. III, p. 290 (New York: Academic Press, 1969).

APPENDIX E. ESTIMATED DOSE FROM THE ELECTROMAGNETIC CASCADE

When an 800-GeV proton is incident on an iron absorber, approximately 63% of the primary proton energy eventually devolves to the electromagnetic (EM) cascade. As there is information on shielding of the EM cascade from electron accelerators (Swa79), an estimate of the photon dose at $d = 2$ m from an effective line source illuminated by hadronic fragments is possible. Although the real lineal distribution of energy incident on the vacuum pipe may not be uniform, the assumption of uniform illumination should give at least the correct order of magnitude and be useful in comparison with other radiation quantities calculated under the same assumptions (neutron fluence from hadronic interactions, photoneutrons).

Preliminary Estimate of the EM dose

To summarize the assumptions made:

- Beam intensity is 1×10^{11} protons at 800 GeV;
- Total beam is lost uniformly around the circumference of $2\,\pi\,1000$ m;
- 63% of beam particle energy is contained in the EM cascade;
- Beam-line to detector distance is $d = 2$ m;
- Attenuation of the EM cascade in iron is given by 1 TVL = 11 cm. (tenth-value layer -- thickness that attenuates dose by a factor of 10);
- In addition, at 90° to the *point* location of an EM cascade a source term useful for shielding estimates is (Swa79, p. 319):

$$D = 1.39\times10^{-3}\,\frac{\text{rad}\cdot\text{m}^2}{\text{J}}, \tag{E-1}$$

where the unit "J"refers to total energy in the EM cascade.

The total energy in a beam of 1×10^{11} protons at 800 GeV is:

$$(1\times10^{11})\times(1.602\times10^{-19}\text{C})\times(800\times10^{9}\text{V}) = 1.28\times10^{4}\text{J}. \tag{E-2}$$

Distribute the 63% of this energy in the EM cascade uniformly around the circumference:

$$W' = 0.63\times1.28\times10^{4}\ \text{J}\ /\ (2\pi\ 1000\text{m}) = 1.28\ \text{J}\cdot\text{m}^{-1} \tag{E-3}$$

The "lineal dose term" D' , (analogous to the lineal source term for radioactive line sources) is then

$$D' = 1.28\ \text{J}\cdot\text{m}^{-1}\times1.39\times10^{-3}\frac{\text{rad}\cdot\text{m}^2}{\text{J}} = 1.78\times10^{-3}\ \text{rad}\cdot\text{m}\ . \tag{E-4}$$

For a preliminary approximation we ignore the intrinsic angular distribution of bremsstrahlung and assume a line source with *constant* attenuation by a factor of 1/10 for every ray connecting the source and detector. [The iron is approximately 11 cm thick, if the coil collars and yoke are combined. The amount of attenuation is greatly underestimated for every ray except those near 90°.] Using the general formula for the dose, D, at distance, d, from a uniform line source and multiplying by the nominal attenuation factor, 1/10, we have:

$$D_{EM} = \frac{1}{10}\times\frac{\Delta\theta\,D'}{d} = \frac{1}{10}\times\frac{(\pi/2)\times1.78\times10^{-3}\ \text{rad}\cdot\text{m}}{2\text{m}} \tag{E-5}$$
$$= 1.42\times10^{-4}\ \text{rad}.$$

For the contributing angular interval, we assume $\Delta\theta = \pi/2$. The justification for this choice is that π radians is the maximum physically possible interval and oblique rays at angles larger than about $\pm\pi/2$ are strongly attenuated; at $\pm\pi/2$ the attenuation factor is of the order of $10^{\sqrt{2}} = 25.9$, rather than 10 and it increases rapidly at larger angles. This effectively reduces the source

length as expressed as the angle subtended at the detectors. This heuristic calculation is believed to give at least the correct order of magnitude (factor of three accuracy). The major error is ignoring the angular variation of thick-target bremsstrahlung intensity which gives an enhanced EM dose coming from upstream of the detectors.

Estimate by Integration

A Moyer-type integration (McC85) using the above assumptions was performed with the parameters:

$$H_0 = 0.0111 \text{ rad}\cdot\text{m}^2\cdot\text{J}^{-1},$$

$$\beta = 1.324 \text{ radian}^{-1},$$

$$W' = 0.128 \text{ J}\cdot\text{m}^{-1},$$

The number of shield attenuation lengths, l, measured perpendicularly to a line source, was made equivalent to 1 TVL:

$$l = 2.303,$$

$$d = 2 \text{ m}.$$

To show the connection between Eq. (E-5) and these parameters: The product $H_0 \times e^{-\beta\cdot\pi/2}$, for $\theta = \pi/2$, equals 1.39×10^{-3}rad·m^2·J^{-1}, the source term given in Eq. (E-1) for 90°. The angular distribution parameter for wide-angle bremsstrahlung, $\beta = 1.324$ radian^{-1}, is consistent with measurements (Din77) and Monte-Carlo calculations (Fas84), for bremsstrahlung angles in the range $\theta_B = 45° - 180°$. The distribution rises to a very strong peak at forward angles -- much higher than this parameter would indicate. However it is shown below that the rays from small-angle bremsstrahlung are so strongly attenuated in the iron, because of the obliquity factor, that they contribute very little. As the detectors are on the interior of the Tevatron ring for our geometry, the sharp bremsstrahlung spike at 0° is not present.

These parameters are used in the Moyer integral for a detector placed at $d = 2$m and $d = 0$:

$$D_{EM} = W' \int_{-\infty}^{\infty} \frac{H_0\, e^{-\beta\theta}\, e^{-l \csc\theta}}{r^2}\, dL \ , \tag{E-6}$$

where dL is an element of source length, L, and $r^2 = d^2 + L^2$. The integral value is 1.15×10^{-4}rad·m·J^{-1}. This gives

$$D_{EM} = 1.28 \text{ J}\cdot\text{m}^{-1} \times [1.15\times10^{-4} \text{ rad}\cdot\text{m}\cdot\text{J}^{-1}] = 1.47\times10^{-4} \text{ rad} . \tag{E-7}$$

This model is consistent with the rough calculation just described but now the thick-target bremsstrahlung angular distribution and the attenuation of oblique rays are handled in a more satisfactory manner.

The integration procedure also provides information on the effective distribution of *source* along the beam line (Fig. E-1): The maximum integrand value occurs at L = -0.6 m, or upstream of the detector at about -17°. The integrand diminishes to half its maximum value at L = -1.9 m and 0.54 m or -43.5° and 15.1°, respectively. This is a total angular interval of 58.6 degrees or 0.33 π radians which contributes most of the dose at $d = 2$ m, L = 0. This is reasonably close to the initial guess of $\Delta\theta = \pi/2$ used in Eq. (E-5). The corresponding range of bremsstrahlung angles is given by the 90° complement, or $\theta_B = 46.5° - 105.1°$; contributions at smaller and larger θ_B are heavily attenuated.

Dividing this EM dose estimate by the direct (not scattered) neutron fluence predicted under consistent assumptions (Appendix B), we get:

$$\frac{D_{EM}}{\phi_{dir}} = \frac{1.47\times10^{-4} \text{ rad}}{60.5\times10^{4} \text{ neutrons}\cdot\text{cm}^{-2}} = 2.43\times10^{-10} \frac{\text{rad}}{\text{neutrons}\cdot\text{cm}^{-2}}. \tag{E-8}$$

This ratio is a definite prediction that may be accurate to within a factor of three. It should hold true at any distance, d, from the beam line as long as the beam loss distribution does not vary too strongly in the vicinity. It should be remarked that the method of estimating the EM dose would be less reliable if the shielding of 11 cm of iron were not present, because the angular variation of bremsstrahlung intensity would have a much greater effect. With 11 cm of iron, the principal contribution of EM dose emerges from a relatively restricted region of beam line.

If the *scattered* neutrons, which constitute about 85% of the total fluence for our tunnel geometry, are considered, the ratio of Equation (E-8) is modified as follows:

$$\frac{D_{EM}}{\phi_{total}} = \frac{D_{EM}}{\phi_{dir}} \times 0.15 = 2.43\times10^{-10}\frac{\text{rad}}{\text{neutrons}\cdot\text{cm}^{-2}} \times 0.15 \qquad \text{(E-9)}$$

$$= 3.64\times10^{-11}\frac{\text{rad}}{\text{neutrons}\cdot\text{cm}^{-2}} ,$$

where 0.15 represents the fraction of direct (not scattered) neutrons. The ratio from Equation (E-9) is the one to be compared to the experimental result.

FIGURE CAPTION

Fig. E-1. Curve labeled "Moyer": Integrand of Eq. (E-6), $(dD_{EM}/dL)/W'$, as a function of distance along the beam line, L , for $d = 2$ m and uniform beam loss, W' . "Approximate" curve, for $|L| \leq 2.0$m, is equivalent to the approximation, Eq. (E-5). Area under either curve, when multiplied by W' gives an estimate of the EM dose at $d = 2$ m.

REFERENCES

Din77 H. Dinter and K. Tesch, Dose and shielding parameters of electron-photon stray radiation from a high energy electron beam, Nucl. Instr. Meth. 143, 349 (1977).

Fas84 A. Fassò, K. Goebel, M. Höfert, G. Rau, H. Schönbacher, G. R. Stevenson, W. P. Swanson and J. W. N. Tuyn, Radiation Problems in the Design of the Large Electron-Positron Collider (LEP), European Organization for Nuclear Research, TIS Commission, Report No. CERN84-02, Geneva (1984).

McC85 J. B. McCaslin, W. P. Swanson and R. H. Thomas, Moyer Model Approximations for Point and Extended Beam Losses, Lawrence Berkeley Laboratory, Report No. LBL-14699, Berkeley, CA (1985).

Swa79 W. P. Swanson, Radiological Safety Aspects of the Operation of Electron Linear Accelerators, Tech. Report Series 188 (Vienna: IAEA, 1979).

APPENDIX F. EXPERIMENTAL UPPER LIMIT TO DOSES FROM THE EM CASCADE FED BY THE HADRONIC CASCADE

Because a large fraction of the initial energy of the hadronic cascade ultimately is carried by photons, it is interesting to estimate the resultant energy deposition in our detectors by photons from the EM cascade.

There is reason to believe that some of the counts to the right of the thermal peak in the MCA pulse height distributions (higher energy side) might be due to photons from the accelerator tunnel environment. On the other hand the majority of counts to the left (lower energy side) of the thermal peak are probably related to neutron capture [via (n, α) or (n, γ)] on materials of the detector, rather than to incident photons.

Justification for these statements is shown in Fig. F-1. The data plotted in the lower portion are the pulse heights at Channel 100 (4.9 MeV photon energy)* as a function of polyethylene sphere radius. The straight line, normalized to the data shows the expected attenuation of 5-MeV photons in polyethylene (μ_{tot} =0.0292cm^{-1}) for the corresponding radii. The agreement in slope is striking, and supports the suggestion that some of these pulses may be due to photons incident on the detectors. It also justifies in retrospect the use of the 45.7-cm (18-inch) sphere to set the upper limit on charged particle dose as this contains the smallest photon background. Possible sources of such photons are manifestly (a) the electromagnetic cascade produced by π^0 decay photons of the hadronic cascade, and (b) neutron capture gammas from such materials as Fe in the magnet yokes and H and Si of the concrete walls.

Figure F-1 also shows the plot of Channel 30 ($\approx$1.5 MeV photon energy) as a function of sphere radius. Clearly these data do not follow the attenuation expected for 1.5-MeV photons in polyethylene (μ_{tot} =0.0559cm^{-1}). However they closely resemble the behavior of the height of the thermal peak (also shown), which strongly suggests that counts to the left of the thermal peak are mostly related to the thermal neutron fluence in the sphere interior rather than to external photon irradiation.

To estimate the dose to the LiI crystals due to external photons from the EM cascade, we assume a pulse height distribution proportional to E_γ^{-2} which is suggested by the track length distribution from shower theory (Ros52). The shape is indicated by the curve of Fig. F-2, which is normalized to the distribution at Channel 70 ($E_\gamma \approx$3.4MeV). This channel is chosen because it is the lowest point of the distribution at which a curve of the assumed shape can be normalized. In doing this we also implicitly assume the energy transfer efficiency is uniform between chosen limits that are given below. The assumptions just described lead to an integral of the form

$$D_{EM} = \left[\frac{N(70)}{M}\right] \times \left[\frac{4900}{(61/3)}\right] \int_{E_1}^{E_2} E^{-1} dE \ \text{MeV}\cdot\text{g}^{-1} \ , \qquad \text{(F-1)}$$

where N(70) is the observed number of counts at Channel 70, M = 6.53 g is the mass of the LiI crystal, the factor $(70)^2$ = 4900 is for normalization and (61/3) converts the abscissa scale from channel number to MeV (Channel 61 corresponds to 3 MeV photon energy*).

Evaluating Equation (F-1) gives

$$D_{EM} = 37\ N(70)\ ln\,(E_2/E_1)\ \text{MeV}\cdot\text{g}^{-1} \ . \qquad \text{(F-2a)}$$

If the integration limits differ by a factor of 100 (ln100 = 4.61), this gives:

$$D_{EM} = 170\ N(70)\ \text{MeV}\cdot\text{g}^{-1} \ . \qquad \text{(F-2b)}$$

---

* This is based on a calibration of the same crystals using gamma sources ^{137}Cs, ^{60}60 and ^{24}Na performed by R. K. Sun (Sun86).

The actual limits are somewhat arbitrary. However the lower limit should include 0.5 MeV (for positron annihilation photons) but not be less than 0.1 MeV where μ_{tot}/ρ for Fe has risen to ten times its minimum value. The upper limit should reflect the fact that, above about 6 - 7 MeV, the effective energy transfer efficiency declines with energy, because the dimensions of the crystal preventing it from absorbing a significant fraction of the photon energy if it interacts by Compton scattering or pair production; the maximum energy deposited by a fast secondary electron is about 6.2 MeV. Energy limits of 0.3 and 30 MeV are chosen for this analysis.

Converting Equation (F-2) by use of 1 MeV = 1.602×10^{-8} g·rad, we have:

$$D_{EM} = 2.7\times10^{-6}\, N(70) \text{ rad} . \qquad \text{(F-3)}$$

Using Equation (F-3) gives approximately the same result whether the bare crystal, the 5.08 cm (2-in) sphere or the 45.7 cm (18-in) sphere is used. The photon dose to LiI so obtained, $D_{EM}(LiI)$, can be compared to the neutron dose to tissue, $D_n(tissue)$ for the same runs. An average over 18 runs made under varying conditions gives $D_{EM} / D_n(tissue) = 1.4 \pm 1.1$. If an anomalous run which gave 5.6 is excluded, the average becomes 1.1 ± 0.5. For seven runs selected as having relatively "quiet" coasting beam conditions, the average is 1.2 ± 0.5.

Lacking a satisfactory method of subtracting other contributions to the LiI pulse height distributions, these results must be considered as upper limits.

REFERENCES

Ros52 B. Rossi, High Energy Particles (Prentice-Hall, Englewood Cliffs, NJ, 1952).

Sun86 R. K. Sun, Photon-Energy Calibration of LiI Crystals Using ^{24}Na, Lawrence Berkeley Laboratory, Health Physics Note LBL-HPN-143 (August, 1986).

FIGURE CAPTIONS

Fig. F-1. (a) Circles: Number of counts in MCA Channel 30 ($E_\gamma \approx 1.5$ MeV photon energy) as a function of sphere radius; Triangles: Counts at maximum of thermal peak as a function of sphere radius. Dashed straight line shows expected attenuation of 1.5-MeV photons in polyethylene.

(b) Squares: Counts at Channel 100 ($E_\gamma \approx 4.9$ MeV photon energy) as a function of sphere radius. Straight line: expected attenuation of 5-MeV photons.

Fig. F-2. Number of counts as a function of channel number for a typical run. Dashed curve shows presumed shape of photon spectrum ($1/E_\gamma^2$), normalized at Channel 70. Solid curve is idealized distribution of pulses from minimum ionizing particles.

APPENDIX G. MINIMUM IONIZING PARTICLES IN CYLINDRICAL LiI CRYSTALS

Charged particles from high energy hadronic cascades (pions, muons) are expected to be near minimum ionizing and their energy loss rate is in the range 1.1 - 1.5 MeV g^{-1} cm^2 (for 1 - 10 GeV muons; PDG86). Each cylindrical LiI crystal is 12.7 mm diameter × 12.7 mm high and of density 4.06 g cm^{-3}. Thus, assuming $dE/dX = 1.2$ MeV $g^{-1}cm^2$, the maximum energy deposition for perpendicular incidence would be 6.2 MeV.

Imagine a unidirectional broad charged particle fluence that is perpendicular to the cylinder axis. For the moment assume that a particle traversing a diametral path deposits unit energy (unit pulse height, P). The distribution of pulse heights, dN/dP, is identical to the distribution of chord lengths, assuming straight tracks with no straggling. It is calculated to be

$$dN/dP = \frac{P}{\sqrt{1-P^2}} \tag{G-1}$$

This may be derived by considering a cylindrical crystal of unit diameter centered at the origin, calculating the length of chord $P(x)$ perpendicular to the x-axis for each value of x over the interval (-1/2, 1/2), and allowing uniform probability in x. Thus:

$$x^2+y^2 = (\tfrac{1}{2})^2 \tag{G-2}$$

$$\frac{dN}{dx}=1 \quad \text{for } -\tfrac{1}{2} < x < +\tfrac{1}{2} \tag{G-3}$$

$$P = 2y = 2\sqrt{\tfrac{1}{2}^2-x^2} \tag{G-4}$$

$$\left|\frac{dP}{dx}\right| = \frac{4x}{P} = 4\times\frac{\sqrt{1-P^2}}{2P} \tag{G-5}$$

$$\frac{dN}{dP} = \frac{dN}{dx}/\frac{dP}{dx} = \frac{P}{2\sqrt{1-P^2}} \tag{G-6}$$

The latter expression is doubled to account for both positive and negative values of x. Equation (G-1), normalized to unit number of pulses (unit area), results. The average value (mean) of P, $\overline{P}$, can be derived from the cosine-averaged value of the sin, and is

$$\overline{P} = \int_0^1 \sin\theta \; d(\cos\theta) = \pi/4 = 0.785 \tag{G-7}$$

The mean-square (MS) value, about the mean is given by

$$\overline{(P-\overline{P})^2} = \int_0^1 [\sin\theta-\pi/4]^2 \; d(\cos\theta) = \frac{2}{3} - \frac{\pi^2}{16} = 0.0498 \tag{G-8}$$

This yields the RMS value about the mean $\Delta P = \sqrt{0.0498} = 0.223$. Expressed in relative terms, $\Delta P/\overline{P} = [0.223/0.785] = \pm 28\%$. The shape of the distribution of Eq. (G-1) is shown in Fig. G-1, in which the mean and ± one standard deviation, ($\overline{P} \pm \Delta P$), are marked.

As mentioned above, the energy deposition of a single minimum ionizing particle describing a diametral path perpendicular to the crystal axis is 6.2 MeV. Using the above factors and the approximate calibration of the MCA pulse height analyzer [Channel 61 = 3 MeV for minimum ionizing particles (Smi85, Sun86)], we find that the centroid [0.785×6.2 MeV=4.87 MeV] of the pulses due to minimum ionizing particles should lie at Channel 99. Thus we should seek minimum ionizing particles in the Channels 71 - 127, which corresponds to an energy interval of ± 28%.

The approximate formula for the minimum-ionizing particle dose, D_{mip}, is then:

$$D_{mip} = \frac{1}{6.53g}\,\frac{3\text{ MeV}}{61}\sum_{C=71}^{127} C\cdot N(C) = 7.53\times10^{-3}\sum_{C=71}^{127} C\cdot N(C)\ \text{MeV}\cdot\text{g}^{-1} \tag{G-9}$$

$$= 1.21\times10^{-10} \sum_{C=71}^{127} C\cdot N(C) \text{ rad},$$

where M = 6.53 g is the mass of the crystal, the second factor, (3 MeV/61), expresses the channel number-energy calibration,* N(C) is the number of counts in Channel C, and the summation is over the MCA channels indicated. As this approach is not very exact anyway, an approximate form for the summation over 57 channels, based on the observed smoothness in the MCA pulse-height distribution, is used:

$$D_{mip} = 1.21\times10^{-10}\,[57\times99\,N(99)]\text{ rad} = 6.8\times10^{-7}\,N(99)\text{ rad}. \qquad \text{(G-10)}$$

REFERENCES

PDG86 Particle Data Group, Particle Properties Data Booklet, Lawrence Berkeley Laboratory (1986).

Smi85 A. R. Smith, Private communication, Lawrence Berkeley Laboratory, (1985).

Sun86 R. K. Sun, Photon Energy Calibration of LiI Crystals Using ^{24}Na, Lawrence Berkeley Laboratory, Health Physics Note LBL-HPN-143 (August, 1986).

FIGURE CAPTION

Fig. G-1. Idealized pulse height distribution for cylindrical detector, where a broad unidirectional beam of charged particles is incident perpendicularly to the cylinder axis. Abscissa value of 1.0 corresponds to 6.2 MeV for minimum ionizing particles in LiI crystals used.

---

* This is based on a calibration of the same crystals using gamma sources ^{137}Cs, ^{60}60 and ^{24}Na performed by R. K. Sun (Sun86).

FIGURE CAPTIONS

Fig. B-1. Fraction of primary energy transferred to the EM cascade as a function of primary energy. Circles show calculation of Ranft (Ran85); points are interpolations.

Fig. E-1. Curve labeled "Moyer": Integrand of Eq. (E-6), $(dD_{EM}/dL)/W'$, as a function of distance along the beam line, L, for $d = 2$ m and uniform beam loss, W'. "Approximate" curve, for $|L| \leq 2.0$m, is equivalent to the approximation, Eq. (E-5). Area under either curve, when multiplied by W' gives an estimate of the EM dose at $d = 2$ m.

Fig. F-1. (a) Circles: Number of counts in MCA Channel 30 ($E_\gamma \approx 1.5$ MeV photon energy) as a function of sphere radius; Triangles: Counts at maximum of thermal peak as a function of sphere radius. Dashed straight line shows expected attenuation of 1.5-MeV photons in polyethylene.

(b) Squares: Counts at Channel 100 ($E_\gamma \approx 4.9$ MeV photon energy) as a function of sphere radius. Straight line: expected attenuation of 5-MeV photons.

Fig. F-2. Number of counts as a function of channel number for a typical run. Dashed curve shows presumed shape of photon spectrum ($1/E_\gamma^2$), normalized at Channel 70. Solid curve is idealized distribution of pulses from minimum ionizing particles.

Fig. G-1. Idealized pulse height distribution for cylindrical detector, where a broad unidirectional beam of charged particles is incident perpendicularly to the cylinder axis. Abscissa value of 1.0 corresponds to 6.2 MeV for minimum ionizing particles in LiI crystals used.

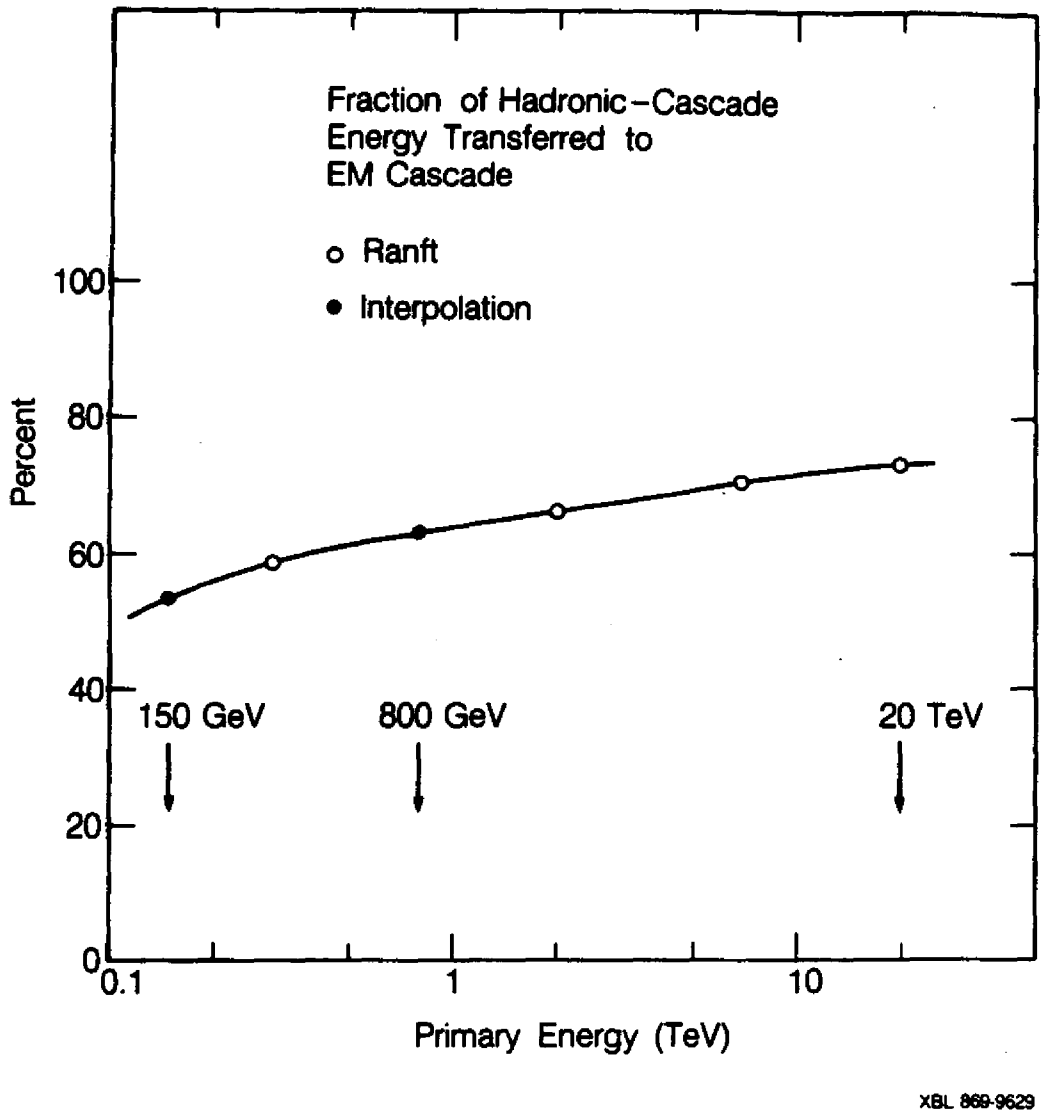

Fig. B-1. Fraction of primary energy transferred to the EM cascade as a function of primary energy. Circles show calculation of Ranft (Ran85); points are interpolations.

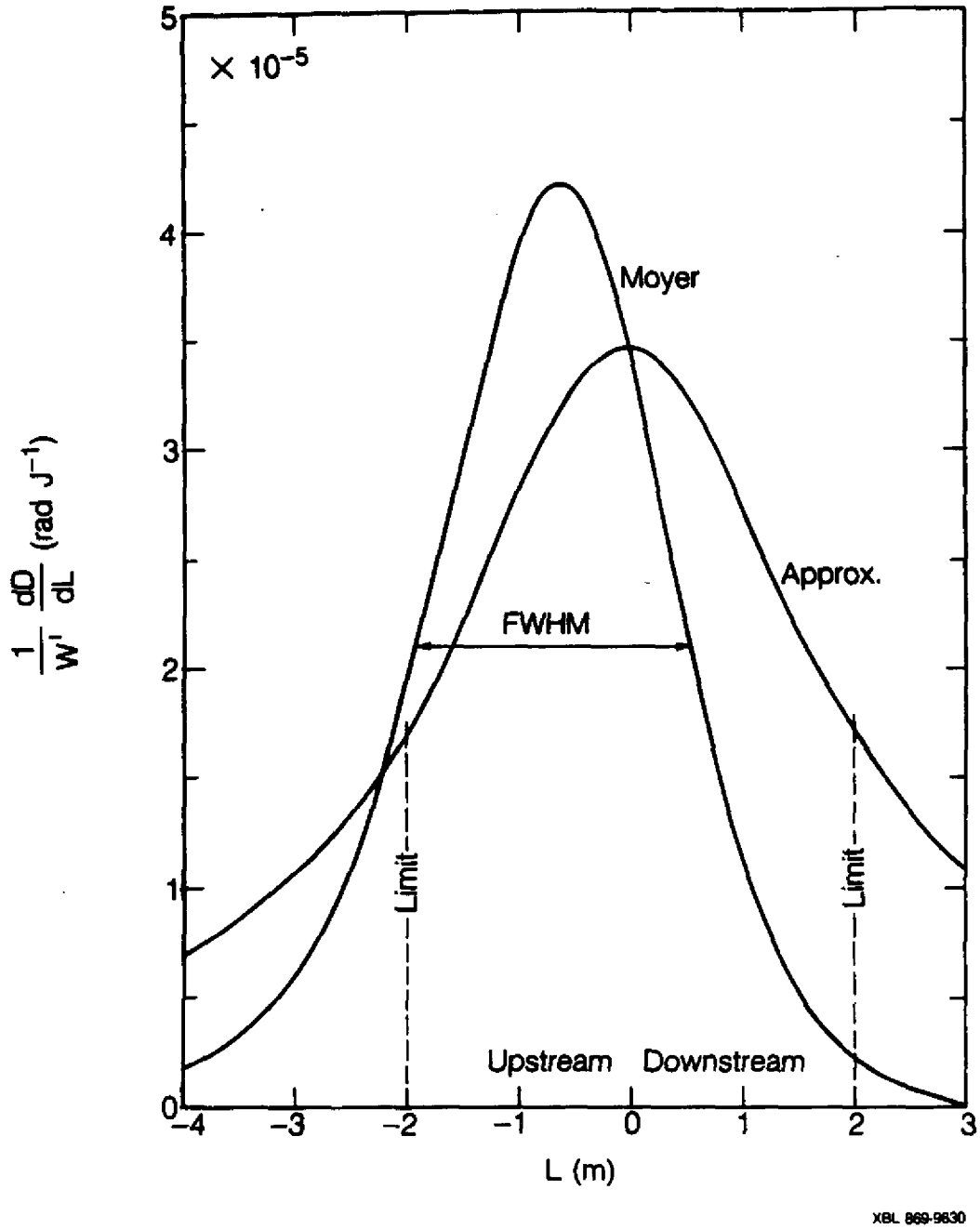

Fig. E-1. Curve labeled "Moyer": Integrand of Eq. (E-6), $(dD_{EM}/dL)/W'$, as a function of distance along the beam line, L, for $d = 2$ m and uniform beam loss, W'. "Approximate" curve, for $|L| \leq 2.0$m, is equivalent to the approximation, Eq. (E-5). Area under either curve, when multiplied by W' gives an estimate of the EM dose at $d = 2$ m.

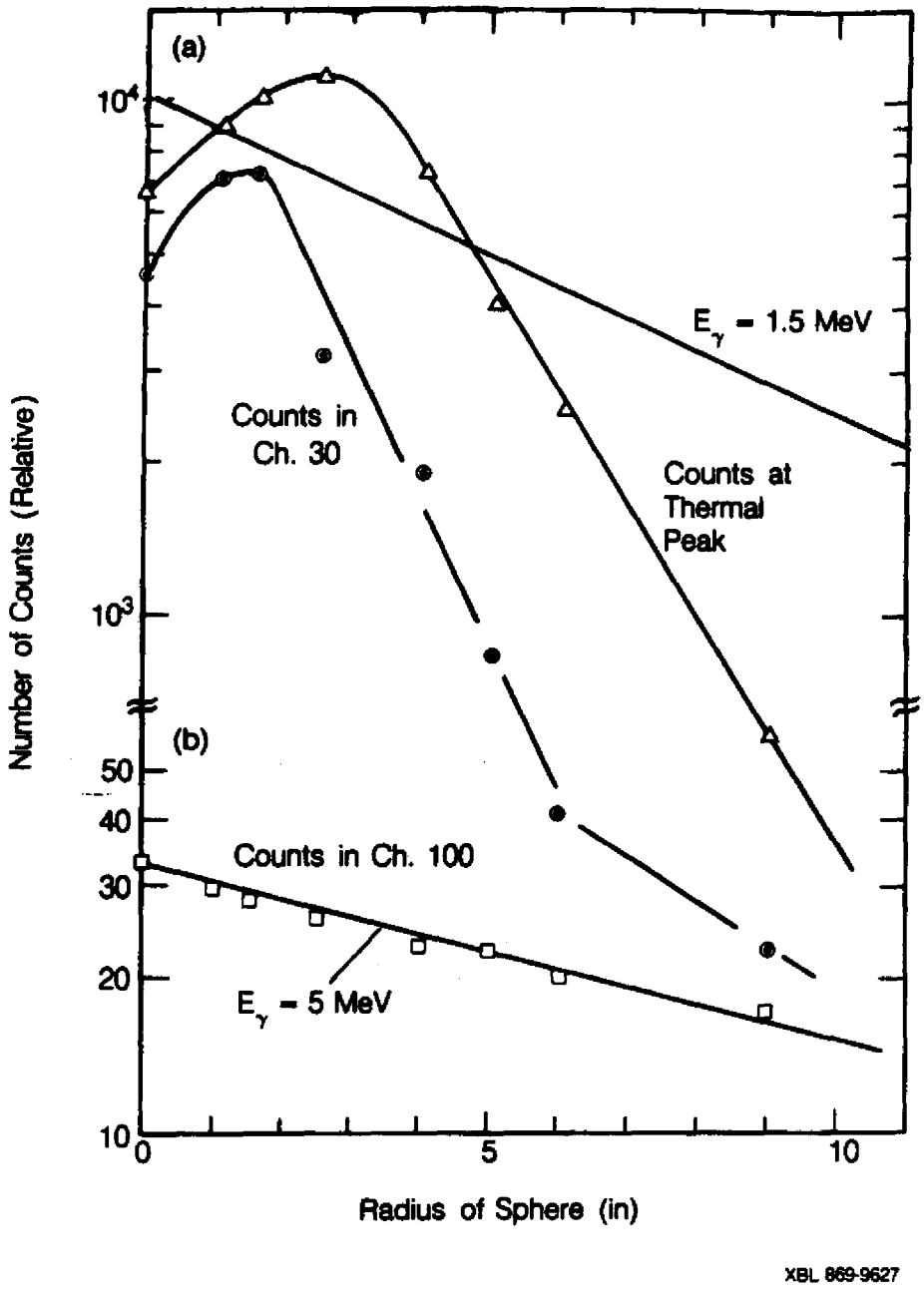

Fig. F-1. (a) Circles: Number of counts in MCA Channel 30 ($E_\gamma \approx 1.5$ MeV photon energy) as a function of sphere radius; Triangles: Counts at maximum of thermal peak as a function of sphere radius. Dashed straight line shows expected attenuation of 1.5-MeV photons in polyethylene.

(b) Squares: Counts at Channel 100 ($E_\gamma \approx 4.9$ MeV photon energy) as a function of sphere radius. Straight line: expected attenuation of 5-MeV photons.

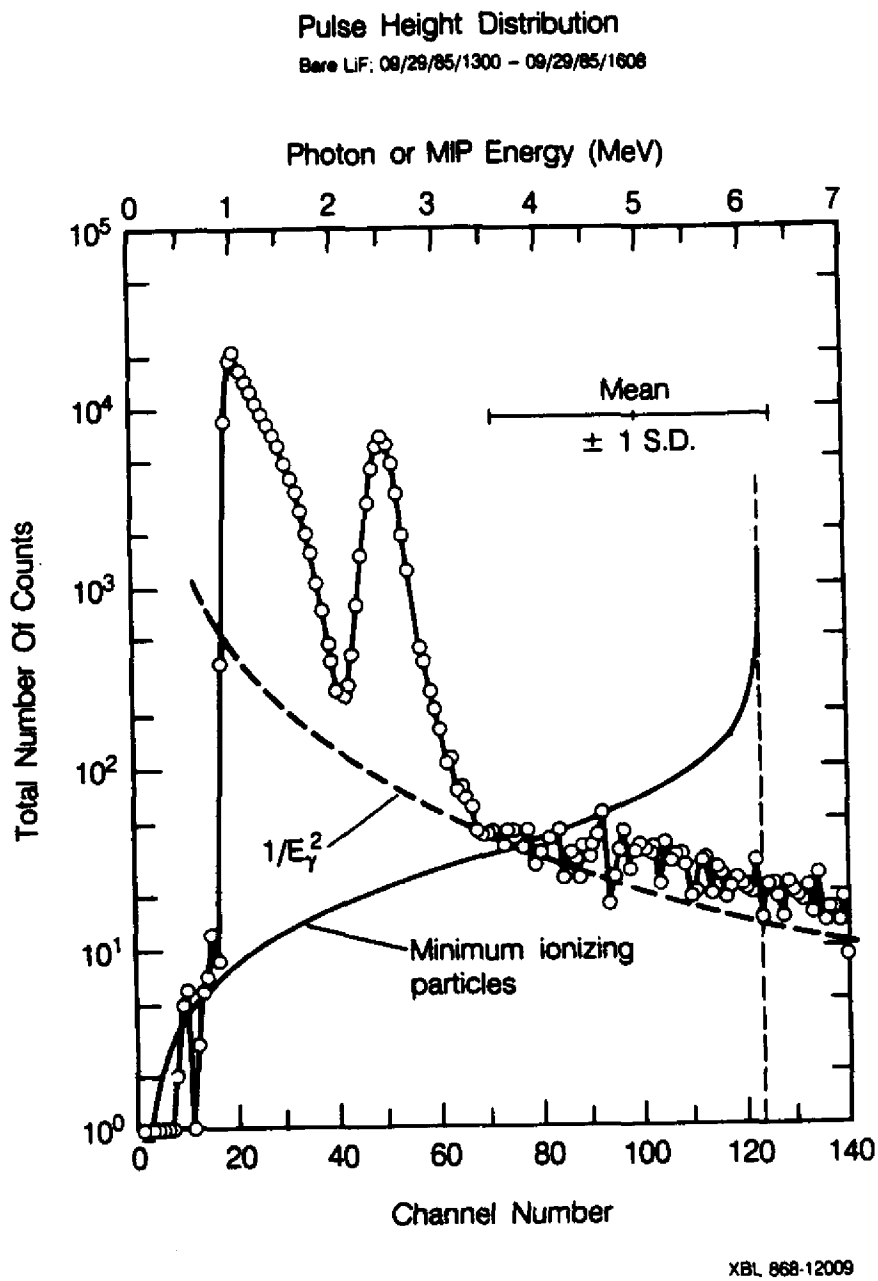

Fig. F-2. Number of counts as a function of channel number for a typical run. Dashed curve shows presumed shape of photon spectrum ($1/E_\gamma^2$), normalized at Channel 70. Solid curve is idealized distribution of pulses from minimum ionizing particles.

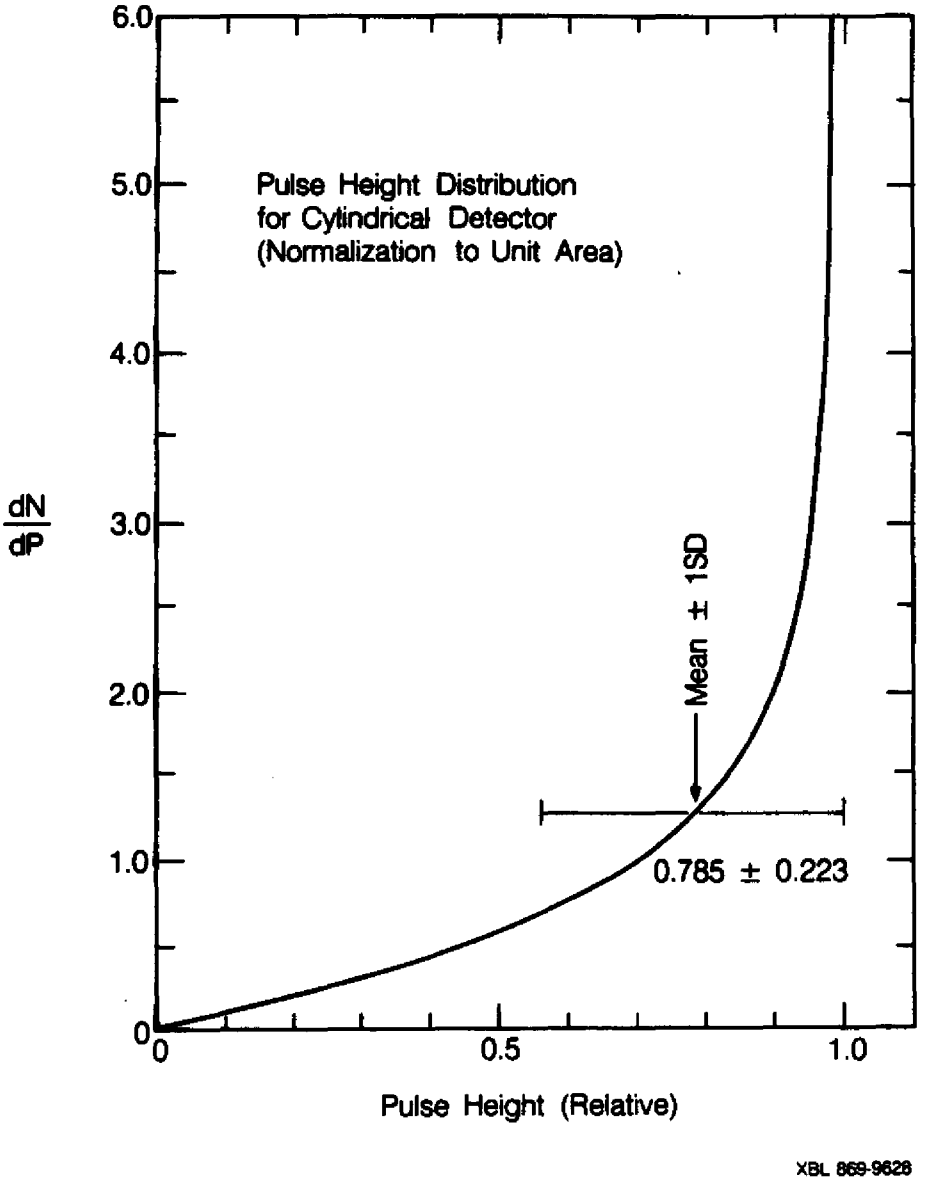

Fig. G-1. Idealized pulse height distribution for cylindrical detector, where a broad unidirectional beam of charged particles is incident perpendicularly to the cylinder axis. Abscissa value of 1.0 corresponds to 6.2 MeV for minimum ionizing particles in LiI crystals used.